Ph.D. DISSERTATION

# One-Dimensional Transverse Magnetic and Unique Transverse Electric Modes in Graphene

## 그래핀의 일차원 직교자기장 모드 및 특이 직교전기장 모드

BY

SERGEY MENABDE

AUGUST 2017

DEPARTMENT OF ELECTRICAL AND COMPUTER ENGINEERING

COLLEGE OF ENGINEERING

SEOUL NATIONAL UNIVERSITY

# One-Dimensional Transverse Magnetic and Unique Transverse Electric Modes in Graphene

지도교수 박 남 규

이 논문을 공학박사 학위논문으로 제출함

2017년 8월

서울대학교 대학원

전기·컴퓨터 공학부

메 나 브 데 세 르 게 이

메나브데 세르게이의 박사 학위논문을 인준함

2017년 8월

위 원 장 이 병 호 (인)

부위원장 박 남 규 (인)

위 원 정 윤 찬 (인)

위 원 민 범 기 (인)

위 원 최 현 용 (인)

# Abstract

## One-Dimensional Transverse Magnetic and Unique Transverse Electric Modes in Graphene

Sergey Menabde

DEPARTMENT OF ELECTRICAL AND COMPUTER ENGINEERING
COLLEGE OF ENGINEERING
SEOUL NATIONAL UNIVERSITY

The scope of light-matter interaction has been significantly enriched with the discovery of graphene in the middle 2000s. An unusual gapless and linear band structure of electrons behaving as massless Dirac fermions is accountable for an ultrabroadband and nontrivial electrodynamic response from the single layer of carbon atoms. Another consequence of the unique carriers dispersion in graphene is its accessibility to Fermi level adjustment in a wide range of energies, allowing for the control of the electrodynamic response at given frequency, thus tuning the plasmonic properties of graphene. For example, the onset of interband electronic transitions, as photon energy

approaches twice the Fermi level, governs the switching from metallic (Drude-like) to dielectric-like type of response when the sign of imaginary part of graphene's conductivity changes from positive to negative. This spectral transition of graphene's electrodynamic response is associated with the two particularly unusual plasmonic phenomena that are the focus of this work.

First, its is highlighted that graphene provides the realistic 2D platform on which a truly 1D metal-dielectric interface can be realized. Assuming the non-uniform doping, two laterally connected semi-infinite areas of graphene with different properties are considered: one being metallic, while the other is a low-loss dielectric with corresponding doping level, having the negative imaginary part of graphene's conductivity. Under this configuration, it is shown for the first time both theoretically and numerically, that 1D metal-dielectric interface (realized on graphene platform) supports fundamental 1D plasmonic mode that exhibits cutoff behavior, providing dramatically improved light confinement in 2D systems. This 1D plasmonic mode constitutes a new basic category of plasmons as the missing 1D member of the plasmon family: 3D bulk plasmons, 2D surface plasmons, 1D plasmons, and 0D localized plasmons.

Second, yet another unique aspect of the graphene's electrodynamic response is rigorously studied: transverse electric (TE) propagating mode that is predicted to manifest when the sign of imaginary part of conductivity changes to negative. Although thus far, a feasible platform for the direct

experimental detection of TE mode at finite temperature is yet to be suggested. In this work, the Otto-Kretschmann scheme is shown to provide such platform for the TE mode excitation in graphene. It is theoretically demonstrated that the TE mode supported by graphene in Otto configuration unusually exhibits a cutoff thickness between the coupling prism and the graphene layer that forbids its efficient coupling to an incident wave in case of a single-layer graphene at typical finite temperatures. In contrast, significantly increased coupling is predicted in the case of an *N*-layer graphene stack, owing to an *N*-fold increase of the effective graphene conductivity.

The excitation and further detection of the TE mode in graphene has been considered a challenge for it is extremely sensitive to excitation environment and phase matching condition adherence. In this work for the first time, the direct optical probing of the TE mode is realized, employing a modified Otto configuration with extremely precise phase matching. In agreement with analytical predictions, a significant coupling to an incident wave is demonstrated in electrically doped multilayer graphene sheet at room temperature. The proposed technique of careful phase matching and obtained access to graphene's TE excitation would stimulate further studies of this unique phenomenon, and enable its application in various fields of photonics.

**Keywords:** Graphene, Graphene Plasmonics, Transverse Electric Mode, 1D Plasmon, 2D Crystals

**Student Number:** 2012-31289

# Table of Contents

# List of Figures

# Chapter 1

# Introduction

## 1.1 Motivation

The discovery of graphene has been acknowledged by the Nobel Prize to its authors [1]. Not only and not just this material is the first known physically existing 2D crystal (a hexagonal crystal of carbon atoms [2]), but it is its properties which have opened up a whole new physics, still being not completely understood. The impact from the discovery of graphene outspreads to remarkably numerous fields of natural science: indeed, a few discoveries have attracted the attention of such broad communities among physicists, chemists, and engineers at the same time.

One of the areas greatly influenced by the discovery of graphene is nanophotonics in general, and plasmonics in particular. The reason for this is that the graphene plasmonics offers a route towards a strong light-matter interaction due to an unusually high field confinement in the propagating plasmonic mode, which is a direct consequence of the graphene's low dimensionality [3]–[5]. Furthermore, a unique and tunable electrodynamic response of graphene allows for the tunability

over its plasmonic resonance through the incredibly wide spectrum – from THz to visible light frequencies. This promises a long-sought efficient and controllable interface between nanophotonics and electronics, as well as providing an access to new regimes of operation where strong field confinement results in, for example, stronger photoresponse or perfect light absorption [3], [5], [6]. The constantly growing interest to this sub-field of plasmonics is illustrated by the publication statistics shown in Fig. 1.1. While graphene-related plasmonic studies exhibit a rapid and constant growth since its birth years, the total number of all other plasmon-related publications seemingly has reached a saturation point around 2014, and even declined in 2016 which has happened for the first time.

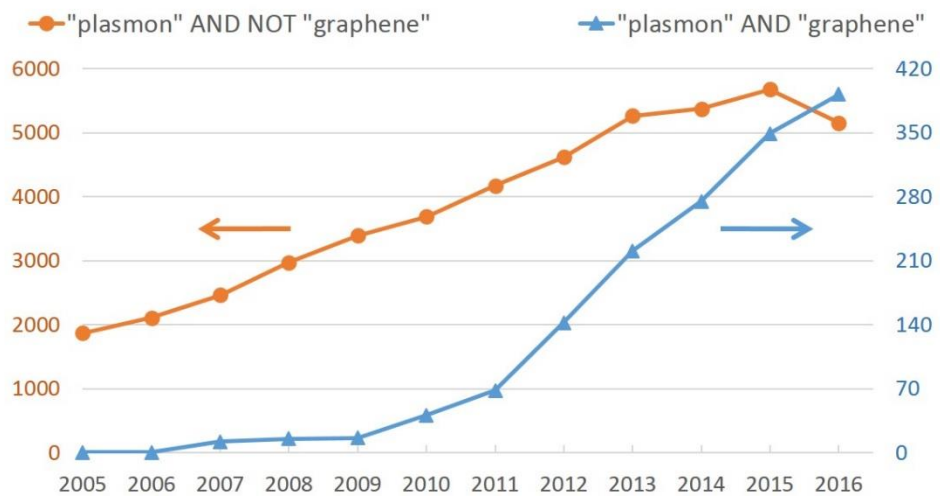


**Figure 1.1.** Annual number of publications on graphene plasmonics and all other plasmon-related studies according to Scopus web resources.

However, between the intrinsically 2D case of the propagating graphene plasmons and the localized plasmons at nanoparticles, there exists previously uncovered case of 1D metal-dielectric (1DMD) interface. While such a 1D interface is of remarkable fundamental simplicity, constituting the low-dimensional

counterpart of the bulk metal-dielectric interface, the existence and nature of plasmonic excitations at 1DMD interfaces remain unknown. At the same time, such an interface is readily available in doped graphene between the two areas with different types of electrodynamic response, metallic- and dielectric-like, which can be controlled by doping. Therefore, the plasmonic excitation at the 1D interface between the metallic- and dielectric-like graphene (1D surface plasmon polariton, or 1DSPP) is investigated in order to reveal its plasmonic properties and application potential for the future photonic devices. Furthermore, 1D plasmons complete the family of plasmonic excitations in all dimensions: 3D bulk plasmons, 2D surface plasmons, 1DSPPs, and down to the localized plasmons at nanoparticles.

At the same time, graphene supports not only a conventional transverse magnetic (TM) plasmonic modes, but also an unusual transverse electric (TE) propagating mode which does not exist in metals or other plasmonic materials. The existence of this mode was first predicted as early as in 2007 [7], but its experimental detection has not been reported so far. The reason for this is that the TE mode is extremely weakly localized and sensitive to the excitation environment, which makes it a particularly hard case for the experimental study, but also a perfect candidate for the ultrasensitive measurement applications. The experimental detection of the TE mode therefore, is both fundamentally and practically important.

Overall, considered in this work, the two graphene modes are the two limiting cases of the propagating electromagnetic excitations with exceptionally strong and weak field localization. It is truly fascinating to observe and study both phenomena in a single framework of graphene electrodynamic response.

## 1.2 Background

### 1.2.1 Low-dimensional surface plasmons in graphene

The first observed low-dimensional collective electron excitations are those at 2D metal-dielectric interfaces, the surface plasmon-polaritons (SPPs). It has been demonstrated that SPPs provide an electric field enhancement and spatial confinement which can dramatically enhance light-matter interactions [3], [8], [9]. In recent years however, graphene has attracted much attention as a long-sought-after plasmonic material alternative to metals due to predicted [10] exceptional electric field confinement of the 2D plasmonic excitations of doped sheets [10], [11]. In pursuit to further increase the electric field confinement of graphene plasmons, the following quasi-low-dimensional schemes have been suggested: graphene ribbon structures [3], [12]–[17], p-n junctions [18], [19], discs [3], [20], [21], and nanoresonators [22] (see Fig. 1.2).

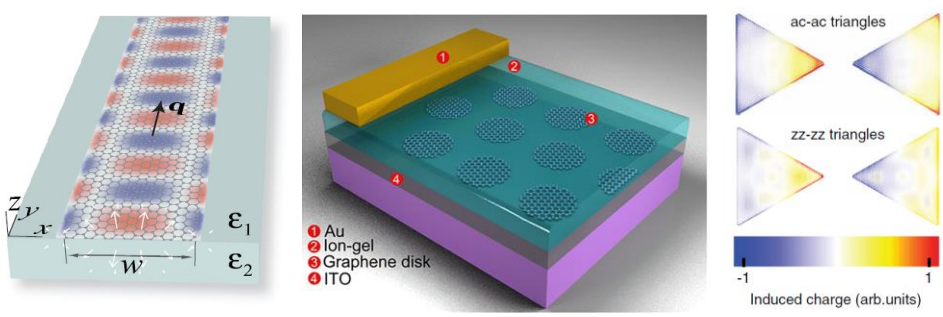


**Figure 1.2.** Low-dimensional schemes to support plasmons in graphene (from left to right): microribbons [13], nanodiscs [21], and nanoresonators [22].

The most well studied low-dimensional graphene configuration is the micro- and nanoribbons. Figure 1.3 illustrates the dispersion and electric field profiles of THz plasmonic modes supported by the 5 μm and 20 μm wide graphene microribbon [13]. The graphene nanoribbon supports several plasmonic modes, including the quasi 1D edge graphene surface plasmons (EGSP) – so far the most low-dimensional manifestation of SPPs in graphene. It is worth to note that the EGSP dispersion does not coincide with that of the bulk 2D graphene surface plasmon (2DGSP) at any

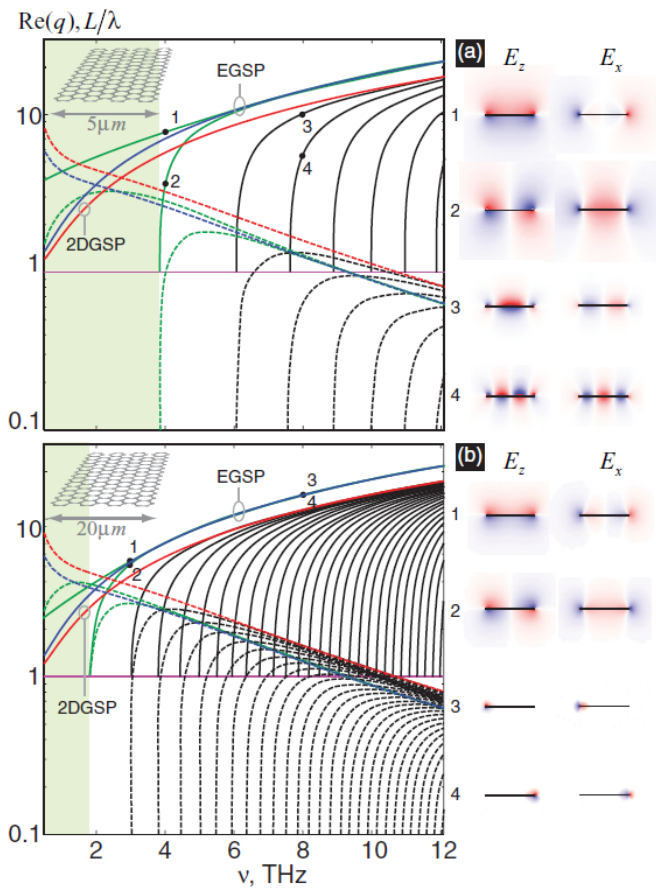


**Figure 1.3.** Dispersion and electric field profile of the THz plasmonic modes supported by (a) 5 μm and (b) 20 μm wide graphene microribbons [13].

frequency (Fig. 1.3), implying the fundamental difference between the two modes, both of which are the fundamental modes of the nanoribbon. Multiple high order modes are also supported similar to the general waveguide of finite geometry.

The effective index of the EGSP is practically the same as that of the bulk mode, highlighting the quasi 1D nature of the EGSP mode. The higher effective index of graphene plasmons compared to noble metals [5] is a promising feature, providing the ground for enhanced light-matter interaction [5], [9]. At the same time, high effective index makes it difficult to excite plasmonic modes in graphene, and their first successful experimental observation at IR frequencies has been reported several years after the discovery of graphene [23], [24] (Fig. 1.4). These successful examples of 2DGSP excitation open the perspective for their utilization in the future optoelectronic devices.

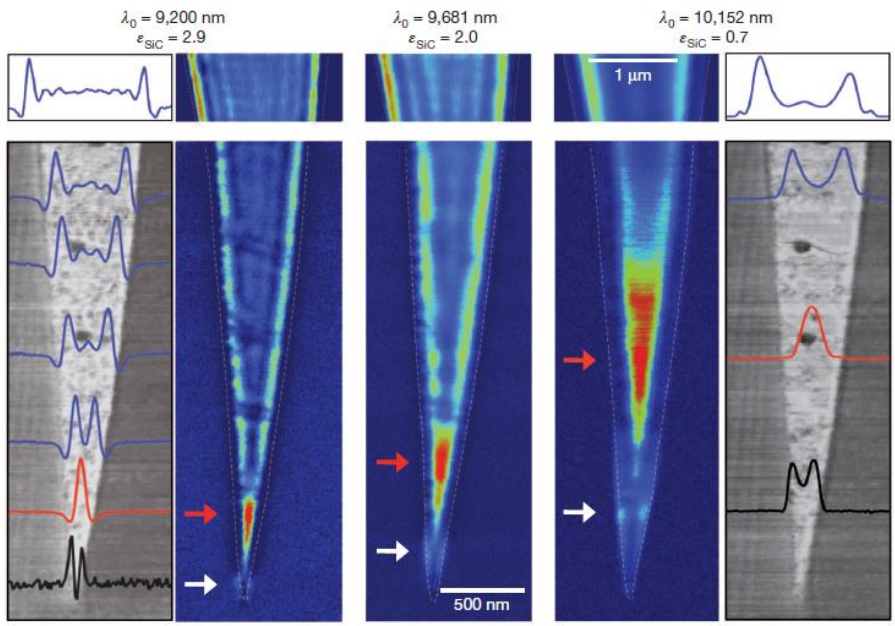


**Figure 1.4.** Infrared nano-imaging of different plasmonic modes in the tapered single layer graphene ribbon obtained by Chen et al. [24].

### 1.2.2 Low-dimensional graphene plasmonic structures formed by doping

Another important feature of graphene is the tunability of its electrodynamic response via the Fermi level tuning. The linear and gapless bang structure of graphene allows for efficient tuning of the Fermi level with for example, the electrostatic doping by top and back gating configuration [6], [21], [25], [26]. This further allows an unprecedented control over the graphene plasmonic response, which is impossible for metals. For example, an uneven doping of the same graphene sheet creates a pattern of areas with different types of the response: metallic-like or dielectric-like, effectively replacing the physical patterning of graphene to create periodic structures such as band-pass filters [27] (Fig. 1.5) or plasmonic waveguides [12] (Fig. 1.6).

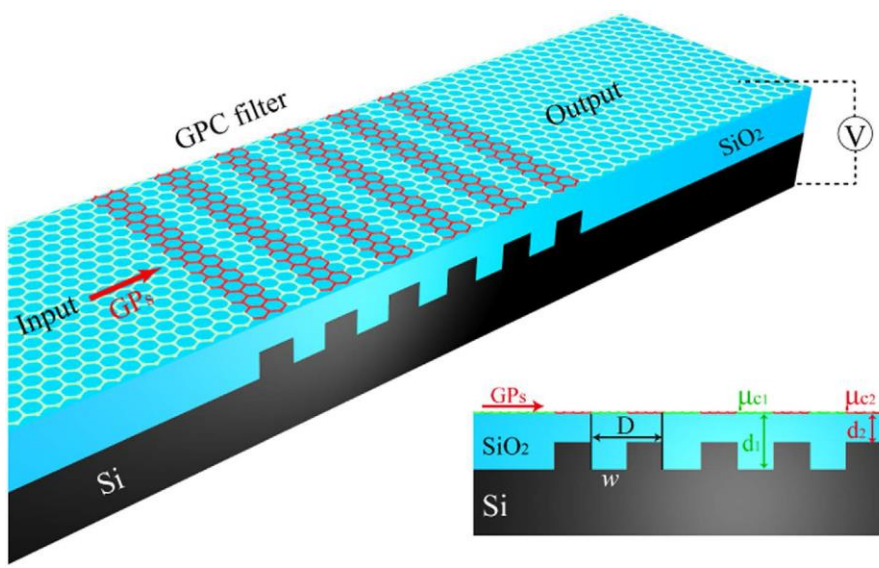


**Figure 1.5.** Periodic structure of the band-stop filter for graphene plasmons formed in uniform graphene by the periodic back gate doping [27].

In this work, the concept of non-uniform doping is adopted, as first proposed by Vakil and Engheta [12], to study the plasmonic response of the 1D interface between the areas of graphene with metallic- and dielectric-like electromagnetic response. Even though this interface has been simulated as a part of the microribbon studies by Nikitin [13], [15], the eigensolutions for this interface had been missed, incorrectly assuming its similarity with the bare graphene edge. At the same time, this metallic-dielectric 1D graphene interface exhibits unique plasmonic properties, supporting the 1DSPP mode, drastically different from the bare edge plasmonic response as demonstrated further in this Dissertation.

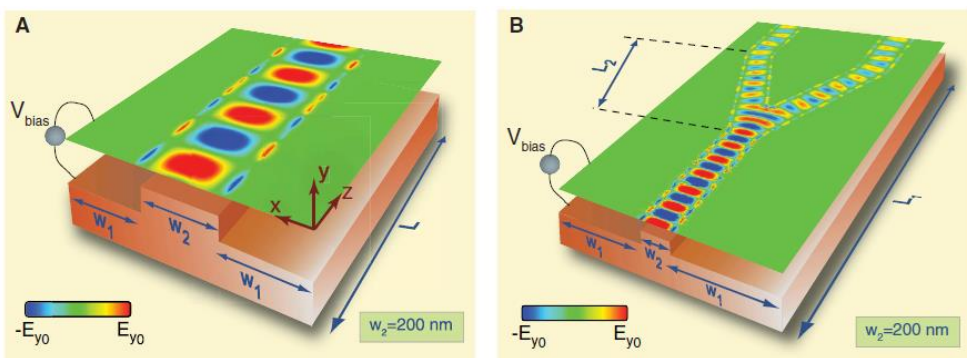


**Figure 1.6.** Concept of plasmonic waveguides formed in uniform graphene sheet by non-uniform back gate doping [12].

### 1.2.3 Transverse electric propagating electromagnetic mode in graphene

As it has been already mentioned, the tunability of graphene's electrodynamic response allows for the unusual regime when the imaginary part of graphene's conductivity $\sigma''$ becomes negative while the real part is still relatively small (Fig. 1.7(a)). Notably, this sign change has been associated with the predicted manifestation of the propagating and localized TE electromagnetic mode, rather than the conventional TM plasmons, i.e. TE (TM) for when $\sigma'' < 0$ ($\sigma'' > 0$), in both single- [7] and bi-layer [28] graphene. The physical nature of the TE excitations in graphene can be understood as magnetic dipole waves, i.e. self-sustained oscillations of current (Fig. 1.7(b)) with no spatial charge density perturbation, while conventional TM plasmons are an electric dipole waves. In analogy with the fundamental guided mode of a high-index dielectric slab waveguide [29] as the slab thickness approaches zero, the TE mode supported by graphene is weakly bound [7] to the graphene plane, therefore exhibiting very low propagation loss [7], and is highly sensitive to the optical contrast between the adjacent dielectrics sandwiching the graphene layer [30]. Based on this sensitivity, a TE-based "plasmonic" gas-sensor has been recently proposed, exhibiting an impressive theoretically predicted detection limit exceeding $6.7\times10^{-7}$ RIU at room temperature [30].

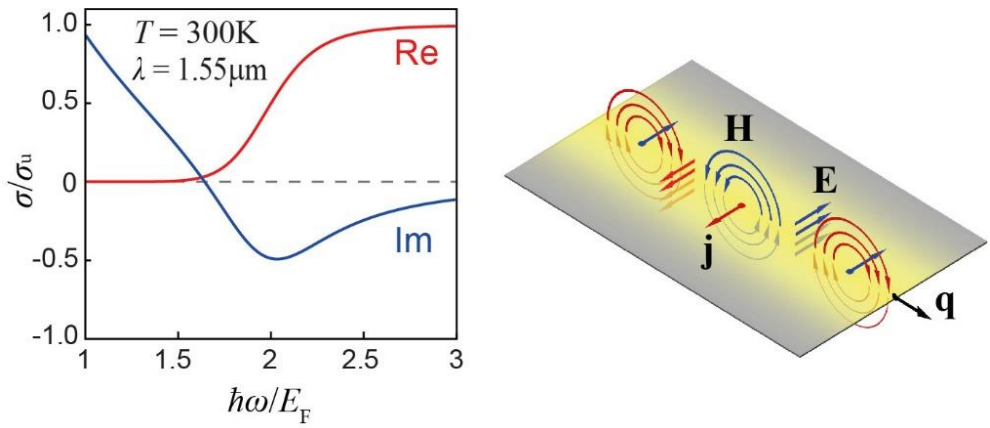


**Figure 1.7.** Spectral transition of graphene and the TE mode. (Left) Graphene sheet conductivity (red – real, blue – imaginary part) at indicated parameters. (Right) Schematic representation of graphene TE mode with wavevector **q** as an oscillation of surface current **j** under excitation by transverse electric field **E**.

However, the very existence of the TE mode, which is a fundamental aspect of graphene's plasmonic response, is yet to be experimentally demonstrated. While theoretical studies of the TE mode have suggested that its experimental detection will be a challenge due to a weak coupling efficiency at finite temperatures, a thorough quantitative analysis pertaining to a real experimental setup is yet to be presented. The novel approach to the problem of the TE mode detection, with comprehensive analytical investigation, as well as the successful demonstration of the first ever experimental detection of TE mode in graphene is presented in this Dissertation.

## 1.3 Layout of dissertation

This Dissertation is focused on the two extreme aspects of graphene's electrodynamic response: a plasmonic response of the real 1D interface induced in graphene by non-uniform doping, and a unique manifestation of the TE mode under certain doping conditions. The plasmonic mode of the 1DMD interface is studied both analytically and numerically, assuming the low-temperature approximation, which allows for derivation of the analytic dispersion relation and FEM simulation of the 1DMD plasmonic mode in COMSOL FEM package. Further, the detailed analysis of the proposed TE mode detection scheme demonstrates the possibility of its experimental detection using the modified Otto configuration. Applying the suggested experimental approach, the excitation of the TE mode is successfully demonstrated in the five-layer graphene stack at excitation wavelength 1.55 μm, and at room temperature.

First, in Chapter 2, the basic theoretical treatment of graphene electrodynamic response is presented, considering the precise solution at finite temperatures, as well as the low-temperature approximation. Also, some key aspects of the FEM simulation of graphene are discussed. Chapter 3 starts with the analytical study of the 1DSPP mode, and then is completed with comprehensive numerical investigation of 1DSPP properties in COMSOL. Chapter 4 presents the theoretical analysis of proposed detection scheme for the TE mode excitation, and Chapter 5 is dedicated to the experimental work, demonstrating the results of successful experimental excitation and detection of the TE mode, as well as the analysis of the obtained data.

## Chapter 2

# Electrodynamic response of graphene

In this chapter, the basic theoretical background on the graphene's electrodynamic response at optical frequencies is discussed from the perspective of analytical and numerical study of the 1DSPP and TE modes. Also, specific aspects of FEM simulation of graphene are discussed, as they are used in the mode analysis of the 1DSPP.

## 2.1 Optical conductivity of graphene and spectral transition region

A unique and attractive feature of graphene's electrodynamic response is its tunability [31] between two different behaviors according to the Fermi level $E_F$ of its charge carriers relative to the photon energy ($\hbar\omega$). At small doping (or, high frequency; $\hbar\omega > 2E_F$), graphene exhibits a dielectric-like properties, such as for example, a broadband and saturable absorbance of ~2.3% [32]. At large doping (or, low frequency; $\hbar\omega < 2E_F$), graphene responds as an atomically-thin Drude-metal which supports localized [3], [20], [22], [26], [33]–[35] and TM propagating [10], [23], [24] SPPs with exceptionally strong electric field confinement. At the same time, studies focusing on graphene's spectral transition region ($\hbar\omega \sim 2E_F$) are surprisingly limited. In the spectral transition region, it has been predicted that the imaginary part of graphene's conductivity (Im[$\sigma$] = $\sigma''$) changes sign from positive ($\sigma'' > 0$, i.e. metallic-like) at low frequencies, to negative ($\sigma'' < 0$, i.e. dielectric-like) at high frequencies [7]. Notably, this sign change has been associated with the predicted manifestation of the TE mode, rather than the conventional SPPs. Furthermore, the very same spectral transition region is responsible for the manifestation of propagating 1DSPP at the 1DMD formed between the metallic and dielectric graphene areas, where dielectric-like conductivity has negative imaginary part $\sigma'' < 0$, and at the same time, very small real part $\sigma' \approx 0$ (which is further demonstrated in Chapter 3).

The sheet conductivity of single-layer graphene at temperature $T$ and Fermi level $E_F$ is obtained from the random phase approximation (RPA) [10], [11], [36] in the local limit, $q \rightarrow 0$ (or, $q << k_F$; $q$ is the plasmon wavenumber, and $k_F$ is the Fermi wavenumber) [37]:

$$\sigma(\omega)=\ln\left[2\cosh\left(\frac{E_F}{2k_BT}\right)\right]\frac{2e^2k_BT}{\pi\hbar^2}\frac{i}{\omega+i/\tau}$$

$$+\frac{e^2}{4\hbar}\left\{H(\omega/2)+\frac{4i\omega}{\pi}\int_0^\infty dx\frac{H(x)-H(\omega/2)}{\omega^2-4x^2}\right\}, \qquad (2.1)$$

where

$$H(x)=\frac{\sinh(\hbar x/k_BT)}{\cosh(E_F/k_BT)+\cosh(\hbar x/k_BT)}, \qquad (2.2)$$

$k_B$ is Boltzmann's constant, $e$ is the charge of an electron, $\tau=\mu E_F/ev_F^2$ is the electron scattering relaxation time, $v_F=3\times10^6$ ms$^{-1}$ is the Fermi velocity of charge carriers in graphene, and the electron mobility $\mu$ thorough the work is chosen conservatively as $\mu=1\times10^4$ cm$^2$(Vs)$^{-1}$ [10]. It is instructive to note that the local limit applies for most cases of plasmonic excitations in graphene, including the 1DSPP and TE modes.

The two terms of equation (2.1) come from the two allowed types of the transitions for the photoexcited carriers [37]: intraband (first term) and interband (second term) as schematically illustrated in Fig. 2.1. Since we are considering the local limit, non-local effects are neglected and $k$ = const., although the $k$-space for possible transitions are wider (Fig. 2.1).

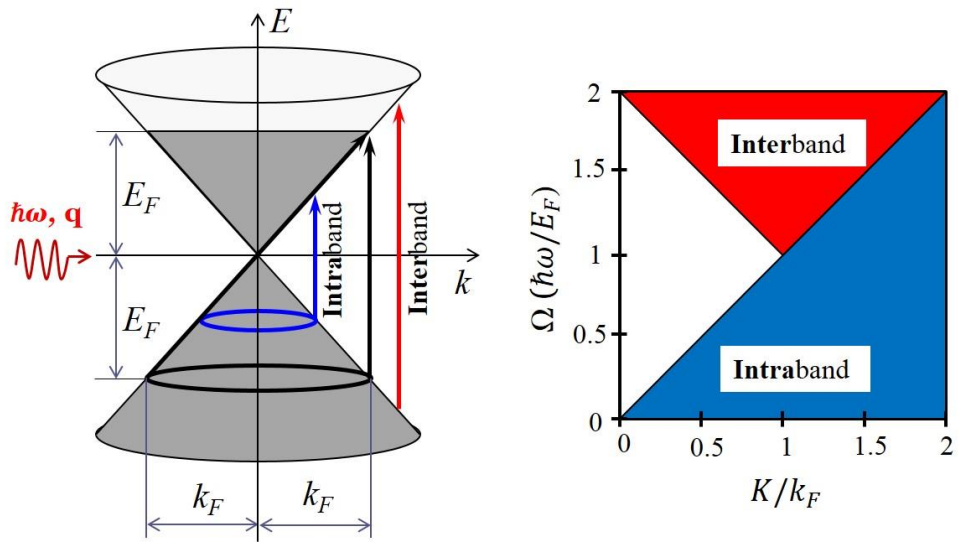


**Figure 2.1.** Graphene band structure and allowed transitions for photoexcited carriers.

The frequency dependent real and imaginary parts of conductivity ($\sigma = \sigma' + i\sigma''$) in the spectral transition region are shown in Fig. 2.2 for several Fermi levels and at the temperatures (a) $T$ = 300K (room) and (b) $T$ = 80K (liquid nitrogen); the conductivity is normalized to the universal graphene conductivity, $\sigma_u = e^2/4\hbar$ [32]. The real part of conductivity $\sigma'$, which determines the optical loss in graphene, is evidently characterized by a shift from small ohmic loss in the Drude regime ($\Omega < 2$; $\Omega = \hbar\omega/E_F$ is the normalized frequency), to a frequency independent absorption $\sigma' = \sigma_u$ ($\Omega > 2$) induced by interband carrier transitions which become dominant as $\hbar\omega > 2E_F$. The effect of increased temperature or decreased Fermi energy is apparent in Fig. 2.2 as a broadening of the transition region. A step-like dependence of $\sigma'$ is approached for increasing $E_F/k_BT$; the $T = 0$ K limit is achieved as $E_F/k_BT \rightarrow \infty$ ($E_F >> k_BT$). An increase of $E_F/k_BT$ simultaneously increases the depth of the minimum of $\sigma''$, and a singularity $\sigma''(\Omega \rightarrow 2) \rightarrow -\infty$ occurs in the $T = 0$K limit [7].

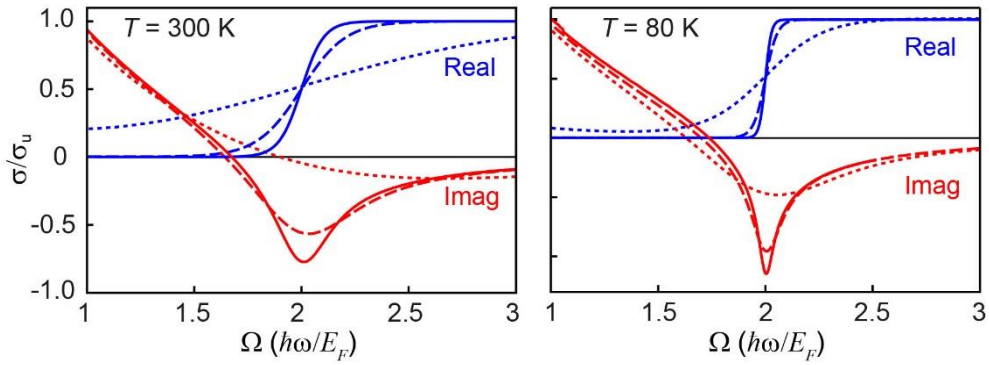


**Figure 2.2.** Real (blue) and imaginary (red) parts of the graphene conductivity in the spectral transition region at $E_F$ = 0.1eV (dotted), 0.5eV (dashed), and 1eV (solid), and at temperatures $T$ = 300K (a), and $T$ = 80K (b). The electron mobility is $\mu$ = $1\times10^4$ cm$^2$ (Vs)$^{-1}$.

The assumption of the $T \approx 0$ K allows for significant simplification of the conductivity's analytical expression, leading to the following temperature-independent form [37]:

$$\sigma(\omega)=\frac{e^2E_F}{\pi\hbar^2}\frac{i}{\omega+i/\tau}+\frac{e^2}{4\hbar}\left\{\theta\left(\hbar\omega-2E_F\right)+\frac{i}{\pi}\ln\left|\frac{\hbar\omega-2E_F}{\hbar\omega+2E_F}\right|\right\}, \tag{2.3}$$

where $\theta$ is the step function. Now, the first (intraband) term is that given by the Drude model for conductivity. The conductivity in form of equation (2.3) leads to an interesting observation: graphene exhibits properties of lossless dielectric in the doping/frequency range exactly in the range $0.5 < E_F/\hbar\omega < 0.6$. This kind of electromagnetic response at quite wide frequency range inside the transition region is a truly unique feature of graphene, and it is this band which makes it possible to observe propagating 1DSPP and TE modes, as will be demonstrated further.

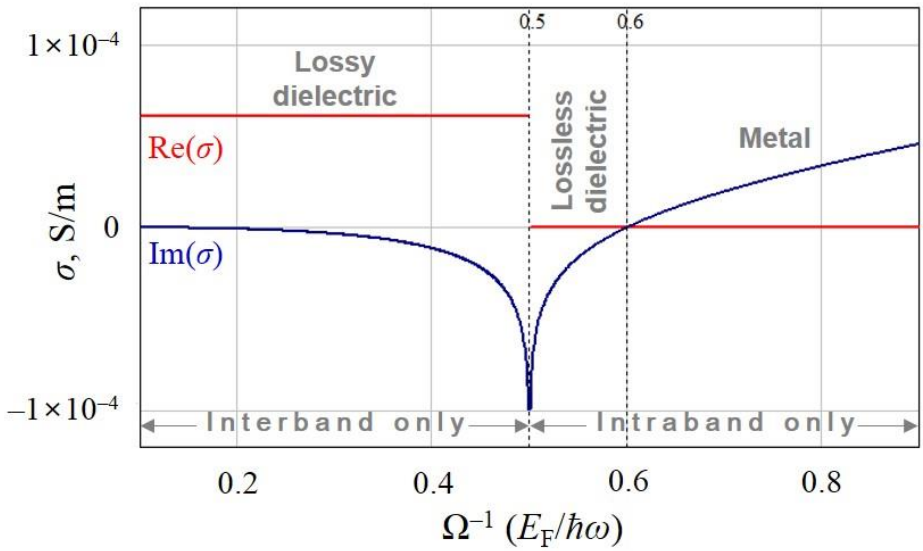


**Figure 2.3.** Graphene conductivity at $T = 0$ limit according to equation (2.3).

## 2.2 Propagating electromagnetic modes

As it was mentioned earlier, graphene supports both TM and TE propagating modes, associated with the positive and negative sign of $\sigma''$ respectively. Dispersion of the TM 2DGSP and TE modes are given in implicit form as [7], [38]:

$$1+\frac{2\pi i\sigma(\omega)\sqrt{q(\omega)^2-\omega^2/c^2}}{\omega}=0 \quad \text{for the 2DGSP,} \tag{2.4}$$

$$1-\frac{2\pi i\omega\sigma(\omega)}{c^2\sqrt{q(\omega)^2-\omega^2/c^2}}=0 \quad \text{for the TE mode.} \tag{2.5}$$

Notably, the small effective index of the TE mode (close to that of the surrounding bulk [7]) $n^{\text{eff}} = \text{Re}[q]/k_0 \approx 1$, where $q$ is the modal wavenumber and $k_0$ is that in free-space, is in a drastic contrast with the TM mode which has $n^{\text{eff}} \sim 10$ at THz, and ~ 100 at IR and visible frequencies. Therefore, the excitation of the TE mode is potentially possible via the conventional attenuated total reflection regime, while the 2DGSP and GEP modes require non-trivial nano-photonic-scale devices and techniques. However, the extremely low contrast of the TE mode makes it unavailable for FEM numerical study, since it is practically indistinguishable from the propagating wave.

Further, the dispersion relation for the edge graphene plasmon modes can readily available from the equation (2.4) if one uses the new frequency value $\omega' = \omega(2/3)^{1/2}$ as was fist demonstrated for the 2D electron gas [39].

## 2.3 Simulation with graphene

In the COMSOL simulations, the graphene is incorporated into the numerical model as a thin film with a thickness of $\delta$, thus having a relative dielectric permittivity of $\varepsilon(\omega) = 1 + i\sigma/\omega\varepsilon_0\delta$, where $\sigma$ is given by equation (2.3). This representation secures the constant current density in graphene layer of any thickness.

It is instructive to have a look at the numerical simulation results for the 2DGSP eigensolution considering different thickness of graphene employed in the simulation, and compare the data with the analytical solution of dispersion equation (2.4). Figure 2.4 demonstrates the error of numerical solution by the COMSOL mode solver (RF module) against the analytical dispersion of the 2DGSP wavenumber $\mathrm{Re}[q]$ and propagation loss $L/\lambda = (2\pi\mathrm{Im}[q])^{-1}$ obtained at THz frequencies. Surprisingly enough, thickness of as much as 5 nm provides the error as good as < 4% for considered frequencies. However, further through this Dissertation graphene thickness in simulation is assumed $\delta = 0.2$ nm to guarantee accurate results at IR frequencies.

As for the edge mode, its simulation error for the wavenumber and losses is shown in Fig. 2.5, exhibiting generally more sensitive behavior compared to the 2DGSP. Still, graphene thickness less than 5 nm should provide good approximation for the THz range.

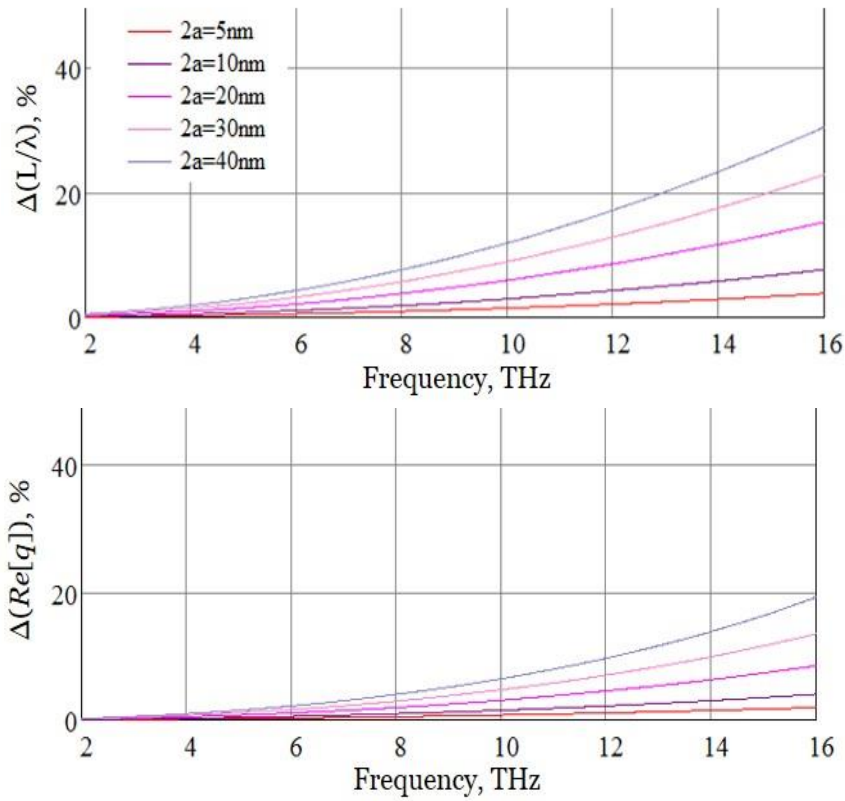


**Figure 2.4.** Error for the numerically obtained wavenumber (top) and losses (bottom) of the 2DGSP.

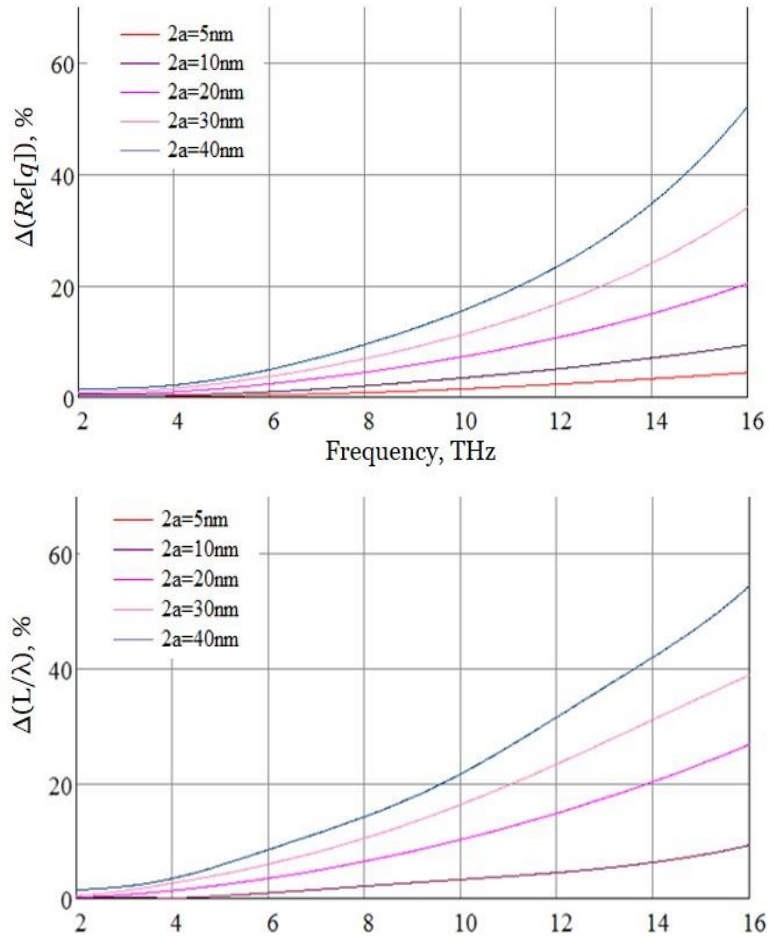


**Figure 2.5.** Error for the numerically obtained wavenumber (top) and losses (bottom) of the GEP.

## Chapter 3

# 1D surface plasmon polaritons at graphene 1DMD interface

In this chapter, the new type of graphene plasmonic response is revealed – the plasmonic excitation of the 1D metal-dielectric (1DMD) interface formed in uniform graphene sheet by non-uniform doping – the 1D plasmonic mode (or, 1DSPP). The 1DMD interface exists between the areas of graphene with metallic and dielectric response at given frequency. It is demonstrated how unique cutoff behaviour of 1DSPPs could allow for a dramatic improvement in the electric field confinement of plasmons in 2D systems in general, exceeding that of previously predicted quasi-1D and 1D plasmonic excitations in graphene [3], [12]–[16], [18]. In the considered example, the confinement of the electric field intensity to modal areas over one million times smaller than the diffraction limit is demonstrated. Furthermore, from a fundamental perspective, the 1DSPP, as the fundamental excitation of the 1DMD interface, constitutes a new basic category of plasmon on its own: the missing 1D member of the plasmon family – 3D bulk plasmon, 2DSPP, *1DSPP*, and 0D localized plasmons.

## 3.1 Dispersion relation of 1DSPP

### 3.1.1 Derivation of dispersion relation

It starts with the consideration of a hybrid 2D system in the $y = 0$ plane comprising two semi-infinite domains laterally connected along the $z$ axis with sheet conductivities of $\sigma^{(L)} = \sigma^{(L)\prime} + i\sigma^{(L)\prime\prime}$ ($x < 0$) and $\sigma^{(R)} = \sigma^{(R)\prime} + i\sigma^{(R)\prime\prime}$ ($x > 0$) (Fig. 3.1) immersed in a uniform medium with relative dielectric permittivity $\varepsilon$.

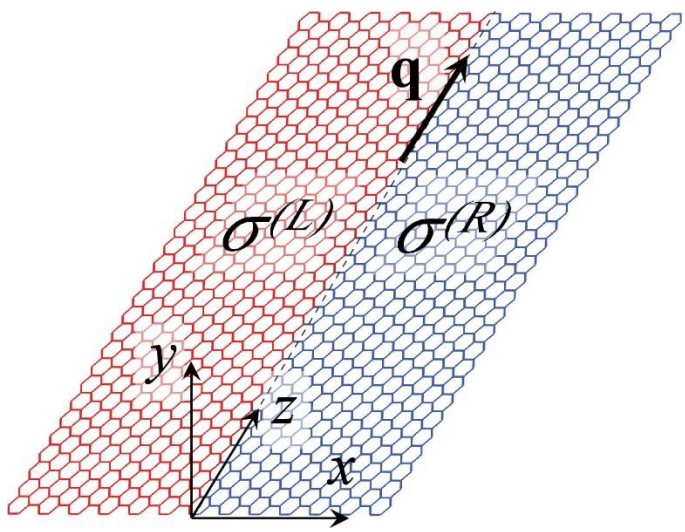


**Figure 3.1.** Hybrid 2D system with two semi-infinite domains of different conductivity.

Without loss of generality, we take regions L and R as metallic ($\sigma^{(L)\prime\prime} > 0$) and dielectric ($\sigma^{(R)\prime\prime} < 0$) domains, respectively. In the quasi-static theory of Volkov and Mikhailov [40], [41], based on the solution to Poisson's equation with an assumed

electric potential of the form $\phi(\mathbf{r}) = \phi_0(x,y)\exp(iq_z z - i\omega t)$, the dispersion relation of plasmons propagating along a 1D junction between two adjoining 2D electron gases (2DEG) is given by [40]

$$1 + \frac{\delta\sigma_{xz}}{i\delta\sigma_{xx}} \tanh\left[\frac{1}{\pi}\int_0^\infty \frac{\mathrm{d}\xi}{1+\xi^2} \ln\left(\frac{\varepsilon_R(\mathbf{q},\omega)}{\varepsilon_L(\mathbf{q},\omega)}\right)_{q_x=|q_z|\xi}\right] = 0. \tag{3.1}$$

Here, $\delta\sigma_{\beta\gamma} = \sigma^{(\mathrm{R})}{}_{\beta\gamma} - \sigma^{(\mathrm{L})}{}_{\beta\gamma}$, where $\beta$ and $\gamma$ are tensor indices ($x$, $z$), and $\varepsilon_{R,L}$ are the effective dielectric permittivities of the left (L) and right (R) 2DEG [40]; $\varepsilon_{R,L} = \varepsilon + i\sigma_{xx}^{(R,L)}(\omega)q/(2\varepsilon_0\omega)$, where $q = \sqrt{q_x^2 + q_z^2}$ and $\varepsilon_0$ is the permittivity of free space. For electrically isotropic 2DEGs in the absence of an external magnetic field, we have $\sigma^{(\mathrm{R,L})}{}_{\mathrm{xz}} = 0$ and $\delta\sigma_{\mathrm{xz}} = 0$. Taking $\delta\sigma_{\mathrm{xx}} = \delta\sigma = \sigma^{(\mathrm{R})} - \sigma^{(\mathrm{L})}$, we obtain

$$-i\delta\sigma \coth\left[\frac{1}{\pi}\int_0^\infty \frac{\mathrm{d}\xi}{1+\xi^2} \ln\left(\frac{\varepsilon_R(\mathbf{q},\omega)}{\varepsilon_L(\mathbf{q},\omega)}\right)_{q_x=|q_z|\xi}\right] = 0. \tag{3.2}$$

When $\delta\sigma \neq 0$, the dispersion relation reduces to when the hyperbolic cosine of the argument in the above equation is zero. To simplify the analysis we start by setting $\sigma^{(\mathrm{R,L})\prime} = 0$, which neglects ohmic and interband losses (see Section 2.1), e.g., pristine graphene in the local and zero-temperature limit at a normalised frequency $\Omega < 2$; $\Omega = \hbar\omega/E_F$. Then, making the variable substitution $\sin\theta = \left(1+\xi^2\right)^{-1/2}$, we arrive at the following dispersion relation:

$$\int_0^{\pi/2} d\theta \ln\left(\frac{\sin\theta - KN}{\sin\theta - N}\right) = i(2m-1)\pi^2/2, \tag{3.3}$$

where $\sigma^{(R)\prime\prime} = K\sigma^{(L)\prime\prime}$ ($K < 0$), the normalised effective index $N = n/n_{2D}$ ($N > 0$; $n = q/k_0$; $k_0 = \omega/c$) is the effective index of the 1D interface plasmon with wavenumber $q$ normalised to that of the planar 2D transverse magnetic (TM) plasmons of region L, $n_{2D} = 2c\varepsilon\varepsilon_0/\sigma^{(L)\prime\prime}$ [10], and $m$ is an integer. The numerical solution of the dispersion is shown in the end of this section, in Fig. 3.3.

Inspection of equation (3.3) reveals that the left hand side of the plasmon dispersion can be written as the difference of two integrals $f(KN) - f(N)$, where $f(C) = \int_0^{\pi/2} d\theta \ln(\sin\theta - C)$. While the solution of this integral lacks a simple closed-form expression for arbitrary $C$, its numerical solution combined with its asymptotic behaviour is revealing that $\mathrm{Im}[f(C)] = 0$ when $C \leq 0$, $\mathrm{Im}[f(C)] = \pi^2/2$ when $C \geq 1$, and $\mathrm{Im}[f(C)]$ increases monotonically as $C$ increases within the range $0 < C < 1$ (see Fig. 3.2; dashed curve). This behaviour immediately precludes solutions for purely real $N$ (i.e. non-leaky) when $K > 0$ (i.e. metal-metal systems) because $0 < f(KN), f(N) \leq \pi^2/2$, which constrains $-\pi^2/2 < \mathrm{Im}[f(KN) - f(N)] < \pi^2/2$, so that the imaginary part of equation (3.3) could not be satisfied for any integer $m$. Indeed, this was earlier pointed out by Mikhailov [41] and corresponds to leakage of the so-called inter-edge plasmon into planar 2D plasmons towards the region with the smaller carrier density (i.e. smaller $\sigma''$).

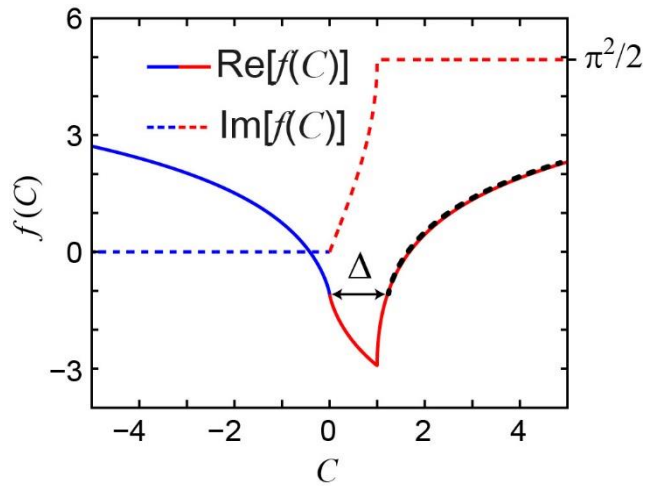


**Figure 3.2.** Real (solid) and imaginary (dashed) parts of the function $f(C)$. The black overlaid dotted curve corresponds to $\mathrm{Re}[f(C+\Delta)] \approx \mathrm{Re}[f(-C)]$.

Now, let's turn to the pertinent case of the 1DMD interface [$K < 0$; $\sigma^{(\mathrm{L})\prime\prime} > 0$, $\sigma^{(\mathrm{R})\prime\prime} < 0$)]. This case has not been previously considered [40], [41] because of the strictly positive sign of $\sigma''$ in conventional 2DEGs. New opportunities to realise 1DMD interfaces in graphene prompt to investigate fundamental solutions to equation (3.3) in 2D metal-dielectric systems. The previous observations imply non-leaky solutions to equation (3.3) for $K < 0$ when $N > 1$ (and $m = 0$), provided that $\mathrm{Re}[f(-|K|N)] = \mathrm{Re}[f(N)]$ (which satisfies the real part of equation (3.3)); indeed, $\mathrm{Im}[f(KN)] = 0$ for $NK < 0$ (i.e. $N > 0$, $K < 0$), and $\mathrm{Im}[f(N)] = \pi^2/2$ for N > 1, thus satisfying the imaginary parts of equation (3.3). From the numerical integration of $f$(C), we empirically find the relation $\mathrm{Re}[f(C+\Delta)] \approx \mathrm{Re}[f(-C)]$ ($C > 0$) (see Fig. 3.2; overlaid dotted black curve). Setting $C = |K|N$ leads to $\mathrm{Re}[f(|K|N+\Delta)] \approx \mathrm{Re}[f(-|K|N)]$, and recalling the solution condition $\mathrm{Re}[f(-|K|N)] = \mathrm{Re}[f(N)]$, we must have (comparing the *positive* arguments of the function $\mathrm{Re}[f(C)]$ which monotonically

increases for $C > 1$, and noting $\Delta > 1$) $|K|N + \Delta = N$. This indicates a dispersion relation of the form $N = N_e/(1 - |K|)$, where we have identified $N = N_e$ as the bare edge plasmon dispersion (i.e. for when $K = 0$), or recalling the definitions of $N$ and $K$ and taking [41] $N_e \approx \sqrt{3/2}$ (the known approximate factor of the bare edge plasmon dispersion [39]), we can write the following for the propagation constant: $q \approx 2\sqrt{3/2}\varepsilon\varepsilon_0\omega / (\sigma^{(\mathrm{L})\prime\prime} + \sigma^{(\mathrm{R})\prime\prime})$. One may also consider the asymptotic behaviour in the limit $N, N|K| >> 1$. Writing equation (3.3) as the difference of two integrals $f(-|K|N) - f(N)$ and Taylor-expanding the respective arguments to the first order, we find:

$$N \approx \frac{2}{\pi}\left(1+\frac{1}{|K|}\right)\frac{1}{\ln\left(1/|K|\right)}; \quad N, N|K| >> 1, \tag{3.4}$$

which further illustrates the limiting behaviour as $|K| \to 1$ of $N \approx (2/\pi)(1 + |K|)/(1 - |K|)$, which is consistent with the $(1 - |K|)^{-1}$ dependence in the empirical relation obtained above. Solution to equation (3.3) only when $m = 0$ naturally precludes the existence of higher-order, multipolar modes because of the step-like transition of the conductivity across the junction; this result is expected, considering that multipolar modes of a bare edge plasmon manifest only when the conductivity decreases monotonically from a constant to zero over a non-zero length $a$ beyond some cutoff [38]. We note that the dispersion of the bare edge plasmon [40], [41] is recovered in the limit that $K = 0$, given by the root of $\int_0^{\pi/2} d\theta \ln\left(\frac{N}{\sin\theta} - 1\right) = 0$, which is satisfied by $N = N_e \approx 1.217\ldots$ [40]. In Fig. 3.3, we plot the dispersion $N(K)$ as determined from the numerical solution of equation (3.3) and as given by the analytical equation (3.4) given for $|K| > 0.5$ (see solid and dashed curves, respectively).

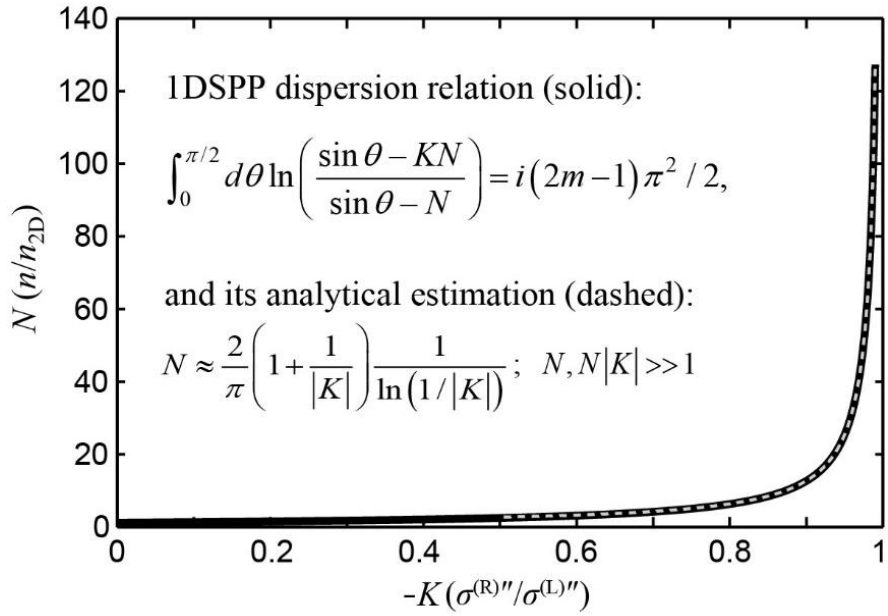


**Figure 3.3.** The numerical solution of the 1DSPP dispersion (equation (3.3); solid curve) and the asymptotic expression (equation (3.4) for $|K| > 0.5$; dashed curve).

### 3.1.2 Important properties of 1DSPP dispersion

While equation (3.3) lacks a closed-form solution, our numerical solution indicates a dispersion relation of the form $q \approx 2\sqrt{3/2}\varepsilon\varepsilon_0\omega / (\sigma^{(L)\prime\prime} + \sigma^{(R)\prime\prime})$. We find that non-leaky plasmons exist (i.e. $N$ is purely real) strictly in the window $0 \leq -K < 1$. At $K = 0$, the plasmon wavenumber takes its minimum value as that of the bare edge plasmon [38] $q_e \approx \sqrt{3/2}n_{2D}k_0$. As $|K| \to 1$, that is, when the electric susceptibilities on the two sides of the interface become equal ($|\sigma^{(R)\prime\prime}| \to \sigma^{(L)\prime\prime}$), the plasmon wave number diverges. Interestingly, this divergent behaviour reveals a strong connection to the conventional SPPs localized to bulk metal-dielectric interfaces [42]. Indeed, in the absence of ohmic loss, the wavenumber of the SPPs ($q_{SPP} = n_{SPP}k_0$) diverges at the surface plasmon (SP) frequency $\omega_{SP}$ given by the non-retarded SP condition [42]: $\varepsilon_d + \varepsilon_m(\omega_{SP}) = 0$; $\varepsilon_d > 0$ and $\varepsilon_m < 0$ are the relative permittivities of the dielectric and the metal, respectively. Likewise, at the 1DMD interface, we note the cutoff condition $K = -1$, or $\sigma^{(R)\prime\prime} + \sigma^{(L)\prime\prime} = 0$ ($\sigma^{(R,L)\prime} = 0$). This reveals that the plasmonic mode of a 1DMD interface is a 1D manifestation of SPPs in 2D systems. An important consequence of the reduced dimensionality can be observed when comparing the respective divergence behaviours: the SPP behaviour takes the form $n_{SPP} \sim 1/\sqrt{\Delta\varepsilon}$ ($\Delta\varepsilon = \varepsilon_d - |\varepsilon_m|$), which diverges much less rapidly than that of the 1DSPP, $n \sim 1/\Delta\sigma$ ($\Delta\sigma = \sigma^{(L)\prime\prime} - |\sigma^{(R)\prime\prime}|$).

It is important to note a clear distinction between the newly discovered 1DSPP, and the recently predicted quasi-1D plasmonic excitations of graphene p-n junctions [18], according to fundamental differences between their respective physical origins. The multiple plasmon modes of a graphene p-n junction [18] owe their manifestation to a spatial gradient of the imaginary part of conductivity (i.e. $\sigma''$), much like the multiple modes of a graded-index waveguide, and the graphene is everywhere

metallic. In contrast, the 1DSPP manifests exclusively as a consequence of the metallic-to-dielectric transition across the 1DMD interface, either side of which the conductivity is spatially uniform. In this regard, we predict that the IR edge wave observed graphically in Vakil et al. [12] is in fact due to the excitation of 1DSPPs, rather than p-n junction plasmons as suggested therein.

### 3.1.3 Lossy 1DSPP dispersion

The lossy 1DSPP dispersion (i.e. when either $\sigma^{(L)\prime}$, $\sigma^{(R)\prime} \neq 0$) is readily obtained on introducing the complex parameter $K$ defined in terms of the complex conductivities $K = \sigma^{(R)}/\sigma^{(L)} = K' + iK''$, and solving for the complex normalized effective index $N = n/n_{2D} = N' + iN''$ (where $n_{2D} = i2c\varepsilon_0/\sigma^{(L)}$; [10]). In the limit that the loss is wholly confined to the dielectric domain ($\sigma^{(L)\prime} = 0$, $\sigma^{(R)\prime} \neq 0$), we obtain the convenient and meaningful expressions $K' = \sigma^{(R)\prime\prime}/\sigma^{(L)\prime\prime}$ (i.e. same as the lossless case), and $K'' = -\sigma^{(R)\prime}/\sigma^{(L)\prime\prime}$. Thus we may imagine that fixing $K'$ and simultaneously increasing $|K''|$ corresponds to fixing of the imaginary part of conductivity of the L and R domains, and linearly increasing the loss ($\sigma^{(R)\prime}$) in the dielectric domain. Conversely, fixing $|K''|$ and increasing $K'$ is equivalent to fixing $\sigma^{(R)\prime}$ and linearly increasing $\sigma^{(R)\prime\prime}$. Meanwhile, the quantity $N'/(2\pi N'')$ reduces to the propagation length defined as the number of optical cycles within one exponential decay length ($l = \mathrm{Re}(q)/[2\pi\mathrm{Im}(q)]$). We note that this physical scenario is particularly relevant to a graphene/graphene metal-dielectric system at finite temperature (see Section 3.2.2) where the dielectric response of domain R is accompanied by interband losses which strongly dominate the overall loss (i.e. relative to ohmic loss in either domain).

The green (dash-dotted) and red (dashed) curves in the inset of Fig. 3.4 show $N'$ when loss is introduced through two example values $K'' = 0.06$ and $K'' = 0.12$. Similarly to the behavior of conventional SPPs on a lossy metal surface [42], the loss is shown to destroy the divergent cutoff behavior of the 1DSPP owing to heavy damping, the onset of which occurs in some vicinity of $K'$ that is specific to $K''$ (compare where $N$ begins to decrease at the two values of $K''$). To illustrate and quantify the onset of 1DSPP damping, the main window of Fig. 3.4 shows the $K''$ dependence of the 1DSPP propagation length at several fixed values of $K'$. At a given value of $K''$, the propagation length decreases with an increase in $K'$, which is typical of plasmons as their wave number increases (recalling that $q$ increases with $K'$). We note that, at each value of $K'$, the curve is cutoff at the x-axis corresponding to the propagation length of just one wavelength (i.e. a strongly damped 1DSPP). It is illustrative to compare the $K''$ cutoff with a particular $K'$, e.g. when $K' = 0.6$, the cutoff is $K'' \sim 0.06$, corresponding to $K''/K' = -\sigma^{(R)\prime}/\sigma^{(R)\prime\prime} \sim 0.1$. Obviously, the loss is more forgiving for smaller $K'$, e.g. when $K' = 0.2$, the cutoff is $K'' \sim 0.12$, corresponding to $-\sigma^{(R)\prime}/\sigma^{(R)\prime\prime} \sim 0.6$.

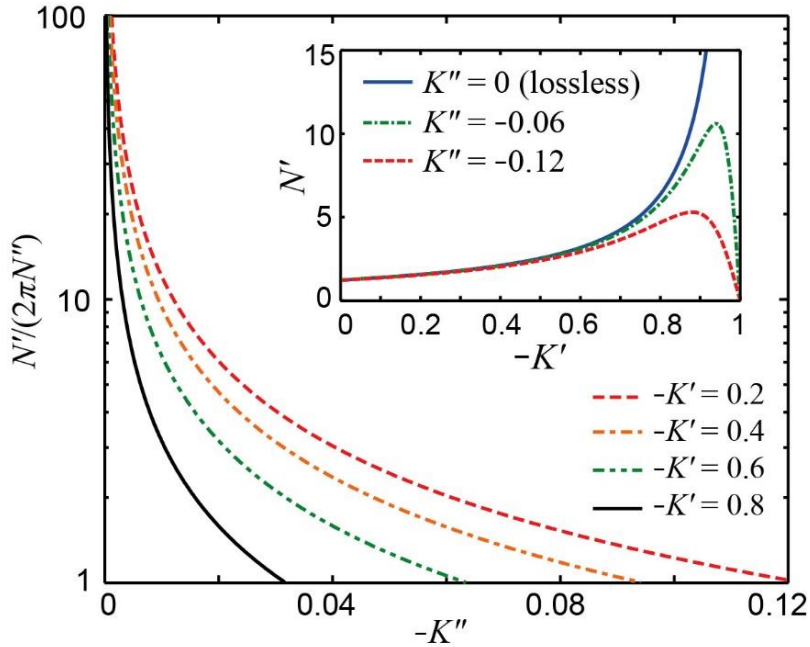


**Figure 3.4.** Plasmonic propagation length as a function of loss factor $K''$. Inset: lossy dispersion for example values of $K''$, as compared to lossless dispersion.

## 3.2 Numerical study of 1DSPP in graphene

### 3.2.1 Zero temperature approximation

In this section, the results of numerical FEM simulations of 1DSPPs in a graphene/graphene metal-dielectric system are presented under the assumption of temperature $T \approx 0$, when the random phase approximation provides convenient closed-form expressions for the optical conductivity in both domains (See Chapter 2). The 1DMD interface is achieved by appropriate doping of both graphene domains; in the local and zero-temperature limit considered here (see [7], and Chapter 2), the doping levels of regions L and R correspond to when $E_F^{(L)}/\hbar\omega > 0.6$ and $0.5 < E_F^{(R)}/\hbar\omega < 0.6$, where $E_F^{(L,R)}$ is the Fermi level of domains L or R. The numerical calculations suggest that the existence of 1DSPPs is not critically dependent on an abrupt sign change of $\sigma^{(R)\prime\prime}$ at the interface (see Section 3.2.3), so graphene systems that support 1DSPPs may also be realised by proposed electrical gating [12] or substrate controlled [43] schemes for spatially non-uniform graphene doping in addition to patterned growth [44]–[47]. We note that in an electrical back-gating scheme [12], the absence of well-defined boundary separating the metallic and dielectric graphene domains would reduce edge effects such as those associated with zigzag edges in graphene and known to be responsible for strong plasmon damping (see for example [6]).

The conductivities on either side of the interface are completely determined by the respective normalised frequencies [7] $\Omega^{(L,R)} = \hbar\omega/E_F^{(L,R)}$. As it has been shown, the dispersion of 1DSPPs (normalized to $n_{2D}$) is completely determined by the dimensionless conductivity $K$, and this behaviour suggests a flexible tunability of the effective index $n$ through the variation of either $\sigma^{(R)\prime\prime}$ ($E_F^{(R)}$) or $\sigma^{(L)\prime\prime}$ ($E_F^{(L)}$) with the

doping level of either graphene domain. To demonstrate this tunability and simultaneously verify the quasi-static analytical results, a mode-solver tool in the numerical FEM package COMSOL is employed, including retardation effects. In Fig. 3.5, we show the calculated dependence $n(E_F^{(R)})$ for several fixed values of $E_F^{(L)}$ (see respective curves) and the spatial evolution of the 1DSPP electric field components $E_x$ and $E_y$. Note the normalisation of $E_F^{(R,L)}$ in terms of $\hbar\omega$; this was verified by comparing all results at the frequencies of 20 THz and 80 THz. One can observe excellent agreement between the dispersion being analytically predicted by the equation (3.3) (solid curves) and the numerically obtained data points. The monotonic increase in $n$ as $E_F^{(L)}$ decreases (at fixed $E_F^{(R)}$) can be readily understood in terms of the corresponding decrease in $\sigma^{(L)\prime\prime}$ and thus $\Delta\sigma$ (recalling that $n \sim 1/\Delta\sigma$). Each curve diverges asymptotically towards a cutoff value of $E_F^{(R)}$ given by the condition $\sigma^{(L)}(E_F^{(L)}) + \sigma^{(R)}(E_F^{(R)}) = 0$. The cutoff value of $E_F^{(R)}$ approaches $0.5\hbar\omega$ as $E_F^{(L)}$ increases. When the photon energy $\hbar\omega$ and the Fermi level $E_F^{(L)}$ are of approximately the same order of magnitude (corresponding to the typical practical situation), the cutoff is very close to 0.5 because of the relative strengths of the interband and intraband terms in the graphene conductivity (see Chapter 2).

The electric field profiles in Fig. 3.6 combined with the plot of the net power flow (Fig. 3.7; normalised to the graphene bare edge plasmon (GEP) [38], i.e. when $\sigma^{(R)} = 0$) demonstrate the nature of the cutoff dynamics at the 1DMD interface. The net power flow parallel to the interface is given by the integral of $S_z = E_xH_y^* - E_yH_x^*$ over the $xy$ plane. $S_z$ is symmetric about the $x$ axis, although the terms $E_xH_y^*$ and $E_yH_x^*$ both exhibit odd sign parity about the $y$ axis; thus, cumulative integration on either side of the interface leads to their respective partial cancellation. This cancellation is weak in the case of GEPs because of the strong field asymmetry, and therefore, the net power flow is significant. Conversely, as the cutoff condition

($\sigma^{(R)\prime\prime} \rightarrow -\sigma^{(L)\prime\prime}$) is approached, the symmetrisation of the field components caused by equal charge screening on either side of the interface (analogous to conventional SPPs near the plasmon frequency [42]) leads to a strong reduction in the net power flow as the group velocity approaches zero.

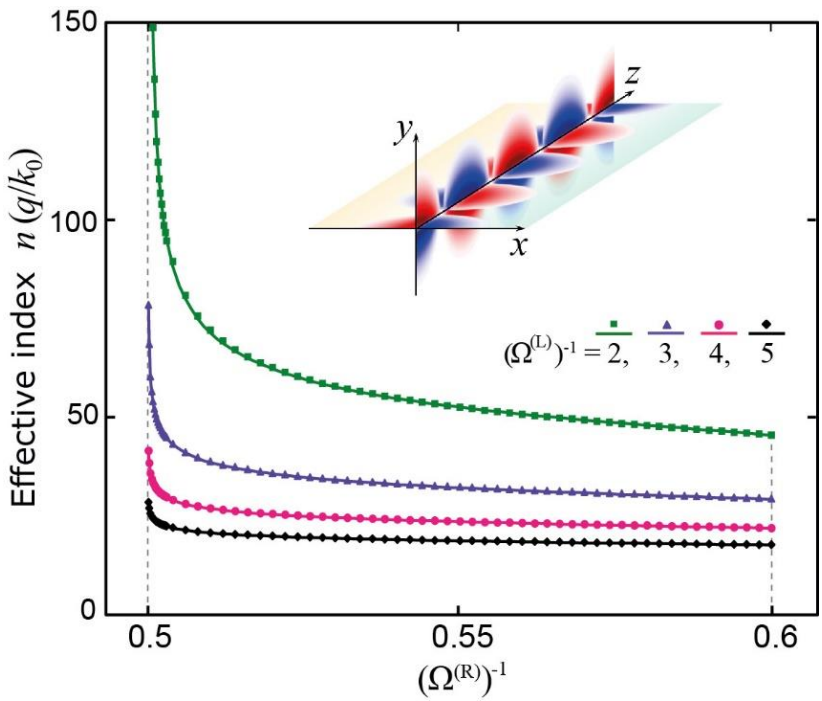


**Figure 3.5.** Effective index of the 1DSPP as a function of $(\Omega^{(R)})^{-1}$, calculated for different $(\Omega^{(L)})^{-1}$: the solution of dispersion equation (3.3) (solid curves) and FEM simulations (data points). Inset: spatial evolution of the 1DSPP electric field components $E_x$ ($xz$ slice) and $E_y$ ($yz$ slice) at $(\Omega^{(L)})^{-1} = 2$ and $(\Omega^{(R)})^{-1} \approx 0.5$.

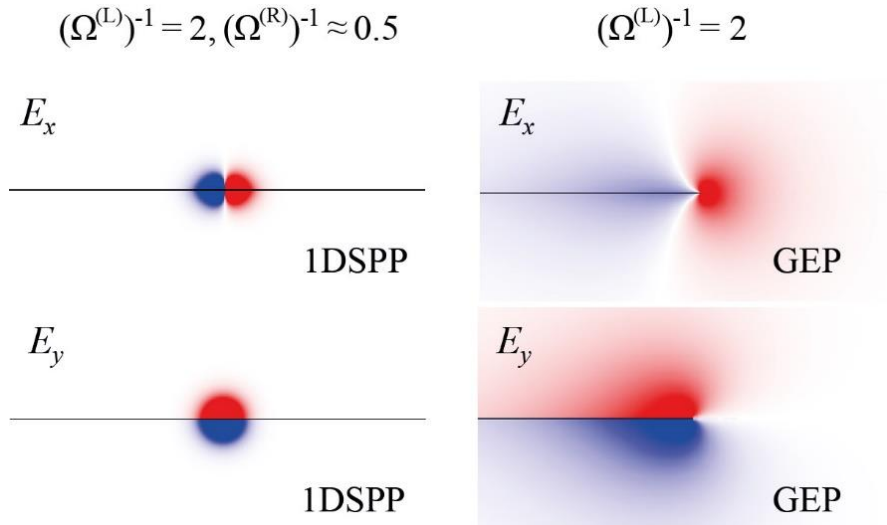


**Figure 3.6.** Electric field profiles of 1DSPP compared with GEP mode.

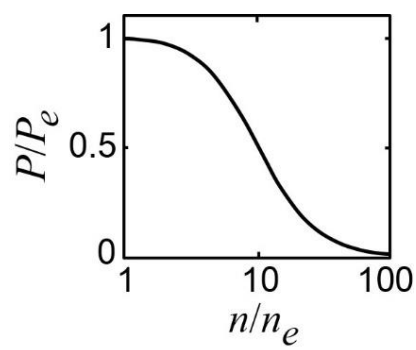


**Figure 3.7.** Dependence of the net power flow $P$ (along $z$) on the effective index $n$ of the 1DSPP, normalised to that of the graphene bare edge plasmon ($P_e$, $n_e$).

Figure 3.8 shows the evolution of the 1DSPP mode cross section as the cutoff is approached, in comparison with the GEP (central solid $K = 0 \rightarrow$ dashed $K = -0.87$). Concentric contours, from the outermost to the innermost contour, correspond to

$(\Omega^{(R)})^{-1}$ = 0.6, 0.58, 0.56, 0.54, 0.52, 0.501, and 0.5002. The dashed contour exactly coincides with that of the GEP. Each contour is defined as a line $|\mathbf{E}|^2$ = constant enclosing an area $A$ (in the $xy$ plane), such that $\iint_A |\mathbf{E}|^2 \, dS / \iint |\mathbf{E}|^2 \, dS = 0.8$.

We note the tremendous localisation of the electric field intensity (Fig. 3.9, left) to regions from $A_0 \approx 5\times10^{-5}\,\lambda_0^2$ to $A \approx 6\times10^{-7}\,\lambda_0^2$ ($\lambda_0$ is the wavelength in vacuum) as $|K|$ increases in the range $0 \le |K| \le 0.87$ (Fig. 3.9, right). Thus, the spatial confinement of the electric field intensity of the 1DSPP in graphene is approximately one million times smaller than the diffraction limit ($\sim\lambda_0^2$); a two-orders-of-magnitude improvement over the graphene bare edge plasmon (i.e. when $K$ = 0).

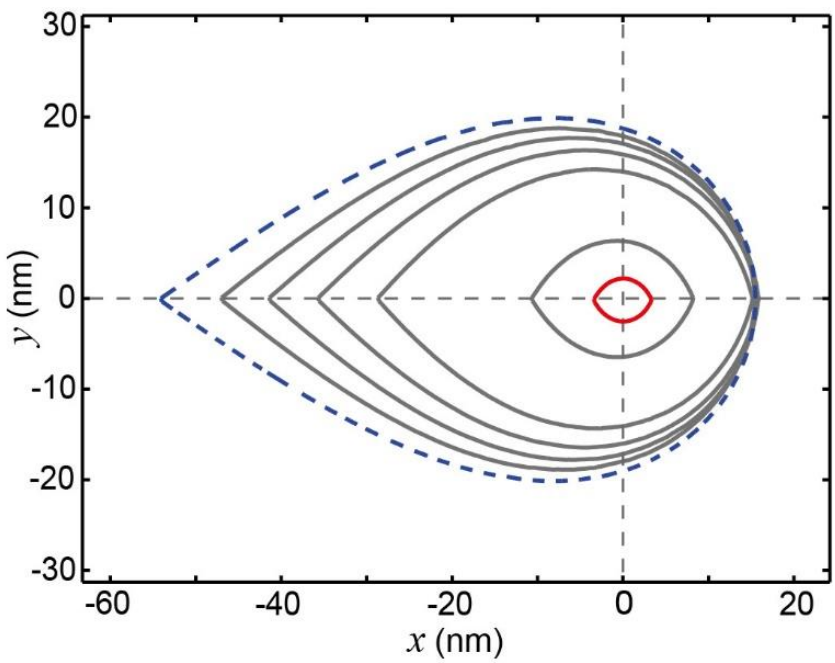


**Figure 3.8.** Mode cross section of 1DSPPs as the cutoff condition is approached as $K$ = 0 (dashed) → $K$ = −0.87 (solid; most inner contour).

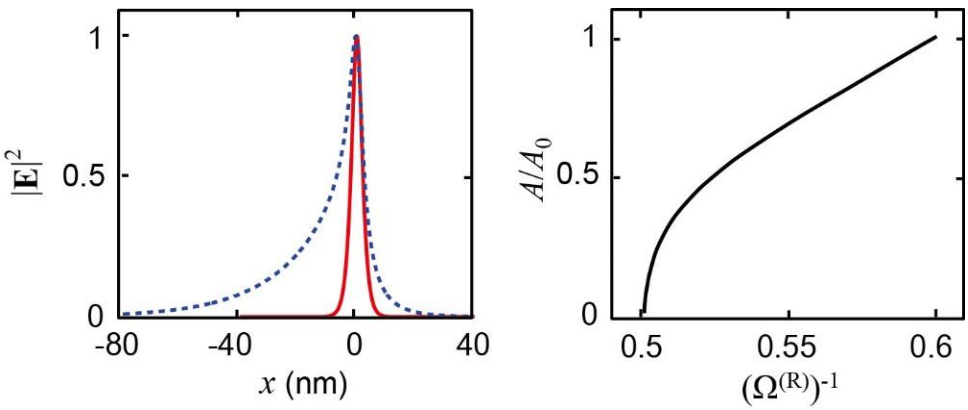


**Figure 3.9.** (Left) Normalised intensity of the electric field (2 nm above the graphene) for the extreme cases $(\Omega^{(R)})^{-1} = 0.6$ (blue, dashed) and $(\Omega^{(R)})^{-1} = 0.5002$ (red, solid). (Right) Mode cross-sectional area normalised to that of the GEP. FEM simulation at 50 THz; $(\Omega^{(L)})^{-1} = 2$.

The above results are not limited to the presented example of graphene but are generalizable to any isolated 1DMD interface in a hybrid 2D system characterised by the same value of $K$. The 1DMD interface in graphene/graphene 2D systems at finite temperature is intrinsically lossy because of the presence of interband transitions, which is essential to achieving the dielectric character in one domain (i.e. $\sigma^{(R)\prime\prime} < 0$; $K < 0$), and further exhibit a temperature-dependent upper limit on $|\sigma^{(R)\prime\prime}|$ (and $|K|$).

### 3.2.2 1DSPP propagation length at finite temperatures

The complex normalised effective index of the 1DSPPs, $N = N' + iN''$, is given by the solution of the 1DSPP dispersion relation (equation (3.3)) for the complex $K = \sigma^{(R)}/\sigma^{(L)}$, obtained with using the general form of the RPA conductivity $\sigma^{(R,L)}$ (equation 2.1) at the specified Fermi energies of the respective domains R and L. From the obtained value of $N$, and from the definition $N = n/n_{2D}$ ($n = q/k_0$, $n_{2D} = i2c\varepsilon_0/\sigma^{(L)}$; note the general form applicable to the case in which $\sigma^{(L)}$ is complex, $\sigma^{(L)''} > 0$), we obtain the complex propagation constant $q$, from which the propagation length is conventionally defined as $l = \mathrm{Re}(q)/[2\pi\mathrm{Im}(q)]$, i.e. normalised to the number of optical cycles within one exponential decay length.

In Fig. 3.10 and 3.11, we show the 1DSPP propagation length for a parameter sweep over $E_F^{(R)}$ and $\omega$ for fixed $E_F^{(L)} = 1.5\hbar\omega$ and for the two different temperatures, $T = 80$ K (liquid nitrogen temperature; Fig. 3.10) and $T = 300$ K (room temperature; Fig. 3.11). The propagation length of the 1DSPPs ($l$) is primarily determined by the ratio $S = |\sigma^{(R)''}|/\sigma^{(R)'}$ and increases as this ratio increases. The ohmic losses in both regions have almost no impact on $l$, even for very conservative estimates of the graphene mobility. At finite temperatures, when $E_F^{(R)}/\hbar\omega < 0.5$, the plasmon is strongly absorbed because of the dominance of interband transitions in region R. The maximum value of $S$ (at fixed $\hbar\omega$) occurs at larger values of $E_F^{(R)}/\hbar\omega$ as the temperature increases from 80 K to 300 K. Furthermore, the maximum value of $S$ itself increases as the ratio $E_F^{(R)}/k_BT$ increases, which can be understood in terms of the decreased smearing of the graphene absorption profile ($\sigma^{(R)'}$ near $E_F^{(R)}/\hbar\omega = 0.5$) at large Fermi energy and low temperature. Thus, an increased photon energy (at fixed $E_F^{(R)}/\hbar\omega$) corresponds to a larger value of $E_F^{(R)}/k_BT$, and the loss is reduced. Therefore, lower temperatures and larger overall doping (i.e. higher Fermi energies

of both domains) provide the optimal conditions for reducing the loss of 1DSPPs in graphene. As an example, we find $l \sim 100$ plasmon wavelengths at $T = 80$ K, $\hbar\omega \sim 0.7$ eV ($\lambda = 1.8$ μm), $E_F^{(L)} \sim 1$ eV, and $E_F^{(R)} \sim 0.4$ eV, corresponding to a propagation length of ~2.6 μm.

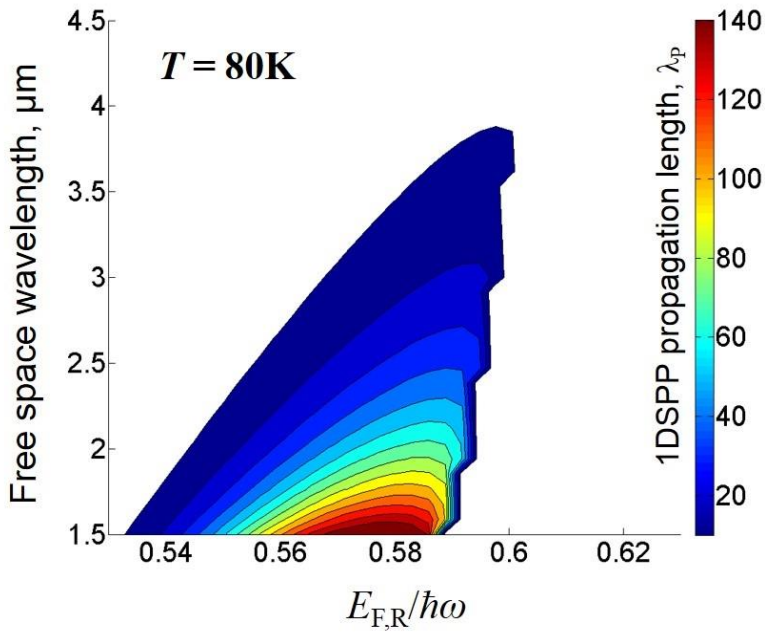


**Figure 3.10.** 1DSPP propagation length (in units of plasmonic wavelength; shown by colour contours) as a function of the photon energy and normalised Fermi energy of dielectric graphene in region R at 80 K.

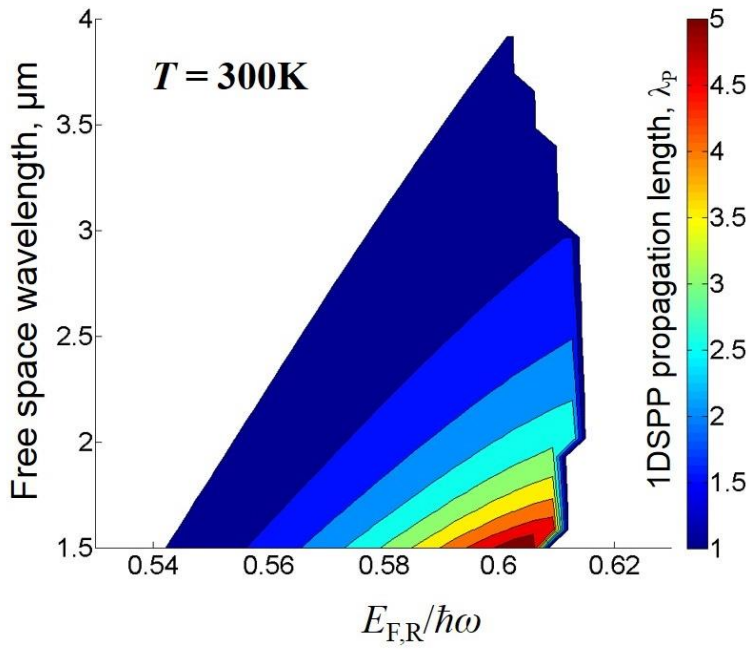


**Figure 3.11.** 1DSPP propagation length (in units of plasmonic wavelength; shown by colour contours) as a function of the photon energy and normalised Fermi energy of dielectric graphene in region R at 300 K.

### 3.2.3 1DSPP in graphene with non-abrupt metal-dielectric junctions

Graphene-based 1DMD interface created via spatially non-uniform doping of continuous graphene sheets will exhibit a smooth transition in conductivity between the constant values $\sigma^{(R)}$ and $\sigma^{(L)}$ on either side of the metal-dielectric (MD) junction. The origin of this effect is the steady decrease in charge-carrier concentration $\rho(x)$ that occurs across the junction from the metallic domain to the dielectric domain. Thus, it is also important to understand the effects of a finite-sized conductivity-transition region on the 1DSPP dispersion when a MD interface is realised on this type of system. An important question is whether the spatially abrupt change of the sign of imaginary part of conductivity at the junction is critical to support 1DSPPs.

As a reasonable approximation, we have assumed a linear relaxation profile of the carriers concentration [38] across the junction (between regions L and R – see inset of Fig. 3.11). The spatial dependence of the conductivity across the junction (Fig. 3.11) is obtained from the RPA in the local and zero-temperature limit (equation 2.3) by inserting the Fermi energy determined from the local value of the carrier concentration $\rho(x)$: $E_F(x) = \hbar \upsilon_F \sqrt{\pi \rho(x)}$. 1DSPP effective index then is obtained from the modal analysis using COMSOL for various widths of the junction region, $d$. Calculations were performed for Fermi energies of $E_F^{(L)} = 2\hbar\omega$ and $E_F^{(R)} = 0.56\hbar\omega$ at frequency of $f = 50$ THz. Note that, at $d = 0$, this MD junction corresponds to $K = -0.12$ and supports the 1DSPP with the third largest asymmetric mode cross section shown in Fig. 3.8.

In Fig. 3.12, we show the effective index of the 1DSPP as a function of the junction width along with several sample mode profiles of the electric field component $E_x$. The increasingly rapid divergence of the 1DSPP effective index and the symmetrisation of the mode profile indicate that the 1DSPP may exhibit a *d*-

dependent cutoff. It is expected that this cutoff is related to an effective local value of $K \approx -1$ (i.e. $\sigma^{(R)\prime\prime} \approx -\sigma^{(L)\prime\prime}$) near the position in the junction where $\sigma'' = 0$ (see Fig. 3.11); recall that the cutoff of the 1DSPP for the abrupt MD interface corresponds to $K \to -1$. A strong sensitivity of the 1DSPP dispersion to $d$ is observed when the junction width is of the same order as the mode cross section of the corresponding abrupt-junction 1DSPP (i.e. with $d = 0$). However, the 1DSPP exists in the same form (e.g., same sign parity of all field components) with negligible perturbation when the junction width is much less than the typical dimensions of the mode cross section. In conclusion, our numerical simulations suggest that an abrupt sign change of the imaginary part of the conductivity at the junction is not critical to support the 1DSPP within the described limits.

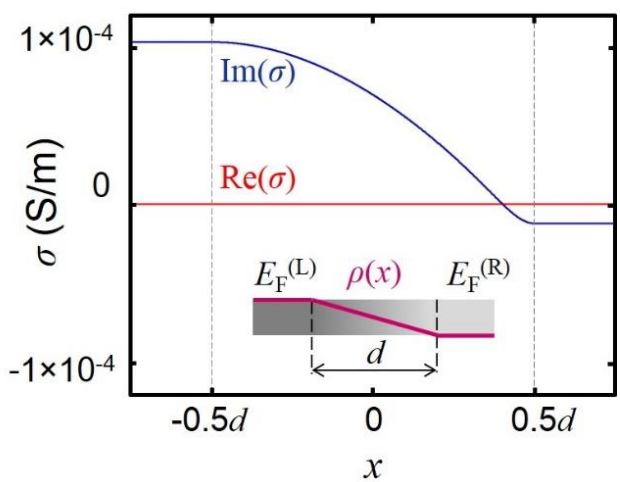


**Figure 3.12.** Spatial dependence of graphene's conductivity $\sigma$ across a non-abrupt MD junction of width $d$; the inset shows the corresponding dependence of the carrier density $\rho$ in the linear approximation.

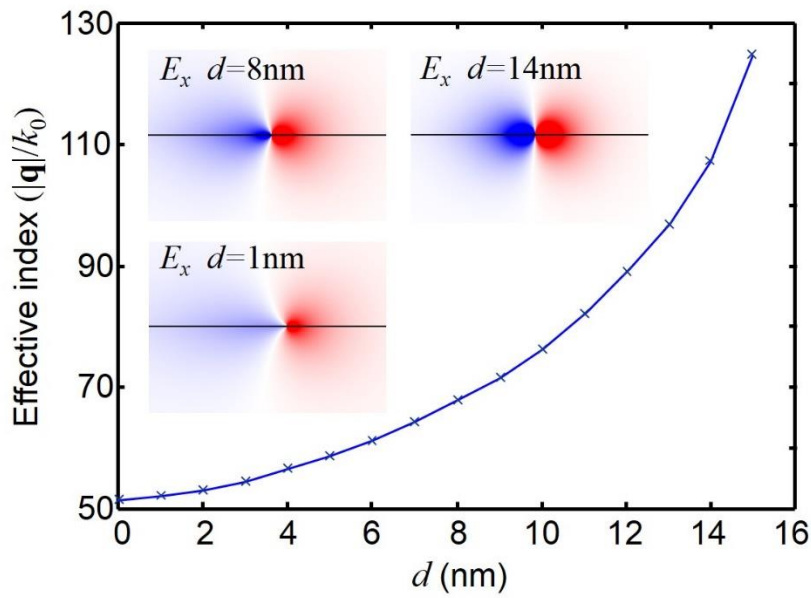


**Figure 3.13.** Numerical data for the 1DSPP effective index as a function of the junction width $d$; the insets show the mode profiles of the electric-field component $E_x$ at the indicated values of $d$. $E_F^{(L)} = 2\hbar\omega$ and $E_F^{(R)} = 0.56\hbar\omega$, and $f = 50$ THz.

## 3.3 Excitation of high effective index plasmonic modes

### 3.3.1 Tapered three-layer plasmonic waveguide

Excitation of surface plasmons in noble metals has been demonstrated long ago, using Otto-Kretschmann configuration via the high-index coupling prism [48]. However, this method is limited by the available materials selection for the coupling prism, and cannot provide phase matching adherence for surface plasmons in graphene with effective index $n_{2D} = 15 \sim 40$ even for MIR and NIR frequencies [49]. To access the higher-index GEP $n_{GEP} \approx \sqrt{3/2} n_{2D}$ or 1DSPP modes, Otto-Kretschmann configuration is inapplicable.

Successful graphene plasmons excitation, recently reported at IR frequencies [23], [24] (see Fig. 1.4), has been accomplished using the scanning nano-tip which scatters the excitation beam. Another excitation scheme targeting the graphene plasmons has been proposed by Nikitin [49], employing the tapered adiabatic polaritonic waveguide where the surface plasmon mode, excited via the coupling prism, experiences the nanofocusing at the narrow end of the waveguide so its high effective index allows phase matching with graphene mode [49]–[51]. This method provides theoretical coupling efficiency up to 30%, significantly exceeding that of the nan-tip-scattering coupling. The schematic illustration of proposed configuration is shown in Fig. 3.14. It has been demonstrated that, as waveguide thickness is reduced, the effective index of the "squeezed" plasmonic mode reaches that of the graphene plasmons (at the range of frequencies), and even significantly exceeds it (Fig. 3.15), satisfying the phase matching condition for the GEP and 1DSPP modes.

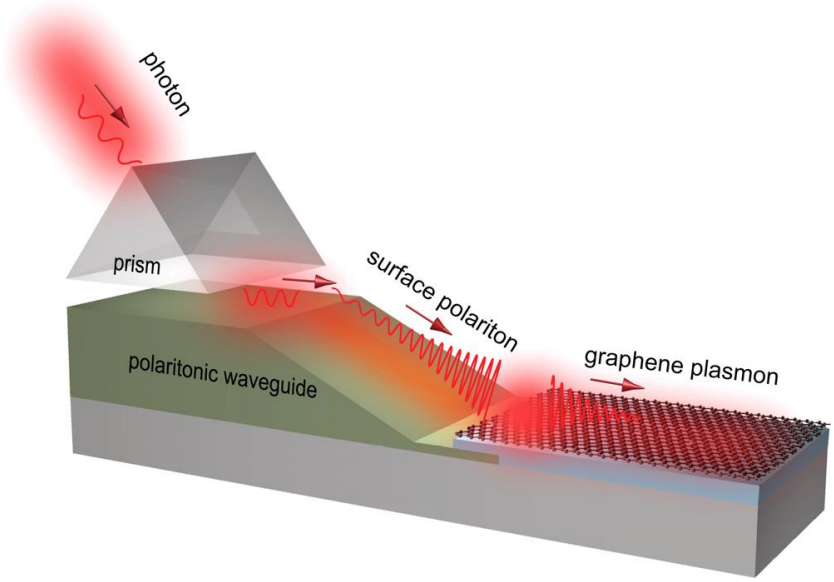


**Figure 3.14.** Schematic of the proposed in Ref. [49] coupling device.

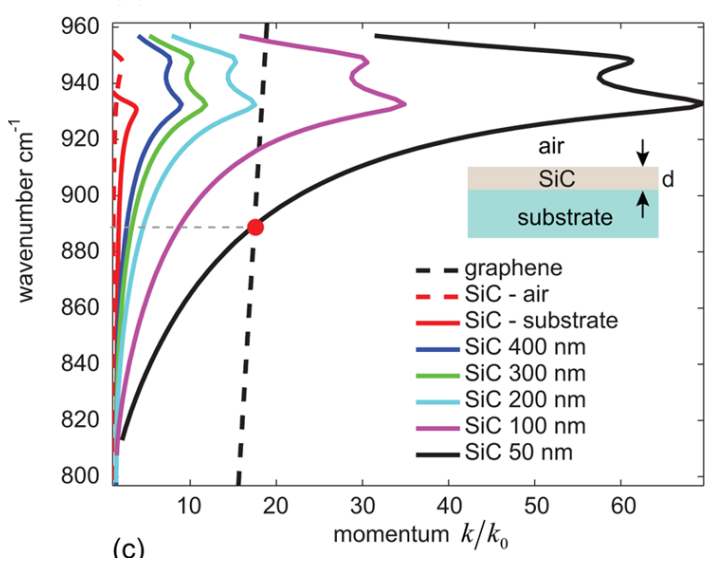


**Figure 3.15.** Reproduced from Ref. [49], dispersion of the surface polaritons in SiC slabs of different thickness and the dispersion of graphene plasmons ($E_F$ = 0.44 eV).

As implied in the study of Nikitin [49], the spectral vicinity of the plasmonic cutoff frequency for given MD interface (corresponding to the dispersion peak in Fig. 3.15) provides optimal conditions for the mode nanofocusing in tapered waveguide, allowing the highest values of the effective index. The cutoff frequency strongly depends on both plasmonic material properties and permittivity of the dielectric layer. Therefore, the spectral position of the cutoff can be selected from the wide range of frequencies by proper selection of materials for the waveguide as demonstrated in Fig. 3.16. Therefore, selection of the tapered waveguide materials gives an additional degree of freedom for its application to the excitation of high-index modes.

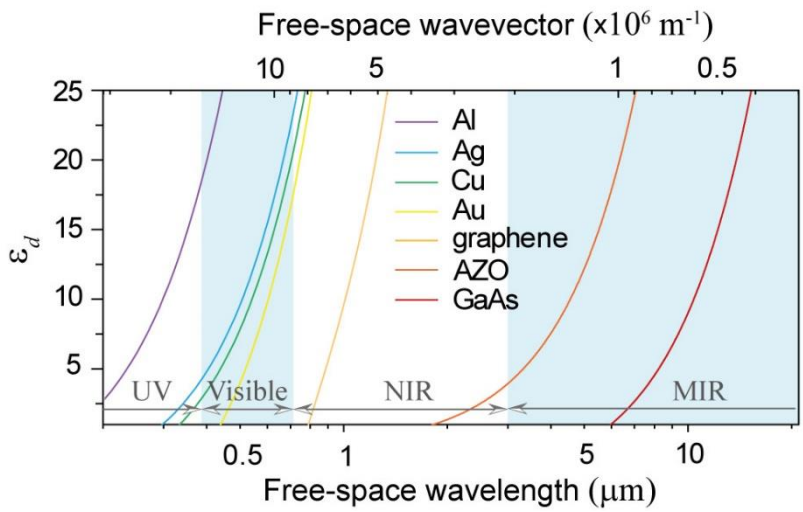


**Figure 3.16.** Spectral position of plasmonic cutoff at MD interface for given plasmonic materials as function of the dielectric layer permittivity. Metallic graphene is considered to have $E_F$ = 1 eV; AZO with charge carrier concentration of $2\times10^{20}$ $cm^{-3}$, and GaAs with $10^{19}$ $cm^{-3}$.

### 3.3.2 Asymmetric tapered waveguide for direct plasmon coupling

Particularly unusual behaviour of the three-layer waveguide's dispersion near the plasmonic cutoff suggests a potentially possible improvement to the tapered-slab-based excitation scheme. For example, it was demonstrated by the Author that plasmonic modes (at given frequency) propagating along the different MD interfaces of the asymmetrical tapered waveguide behave differently the tip. Their behaviour originates from different cutoff frequencies at different MD interface. As waveguide thickness $t$ decreases, the propagating surface mode starts to "feel" the opposite interface as $t$ becomes comparable with the mode size, so that surface mode of thick part couples to the mode of a three-later waveguide. As it further propagates towards the tip, this three-layer waveguide mode experiences an evolution, assumed in previous studies [49]–[51] but never explained in the detail.

To demonstrate the evolution of plasmonic response in a general asymmetric dielectric-metal-dielectric (DMD) waveguide (Fig. 3.17), the dispersion equation must be solved considering only low-lossy solutions when $|q| \leq 1$:

$$k_2 = \frac{1}{2t}\left[\operatorname{arctanh}\left(-\frac{k_2\varepsilon_1}{k_1\varepsilon_2}\right) + \operatorname{arctanh}\left(-\frac{k_2\varepsilon_3}{k_3\varepsilon_2}\right) + \pi q i\right], \tag{3.5}$$

where $k_j^2 = k_p^2 - k_0^2\varepsilon_j$, $j$ = 1, 2, or 3, and $q$ is integer. Other forms of 3L dispersion can be found elsewhere [49], [50], [52], [53]. The typical plasmonic response of the waveguide consists of the following three modes: the short range surface plasmon mode (SRSP; $q$ = 0), the long range surface plasmon (LRSP; $q$ = 1) mode first described by P. Berini [54], and the negative index mode when $q$ = –1. The Author has published the detailed study of these modes in the corresponding work.

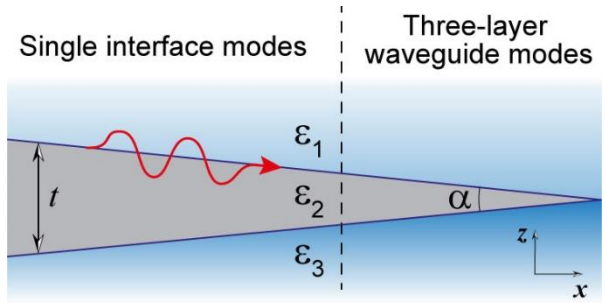


**Figure 3.17.** Schematic of general three-layer tapered asymmetric DMD waveguide.

In general, the dispersion of the SRSP and negative modes in the asymmetric waveguide is characterized by a double-peak behavior, with the peaks associated with the cutoff momenta at the corresponding interfaces: $k_0^{|\varepsilon 2|=|\varepsilon 1|}$ (when $|\varepsilon_2| = |\varepsilon_1|$) and $k_0^{|\varepsilon 2|=|\varepsilon 3|}$ (when $|\varepsilon_2| = |\varepsilon_3|$). At the same time, the LRSP mode is characterized by a cutoff momentum $k^{\mathrm{LRSP}}$ [54], below which the LRSP mode becomes leaky [54]–[56]. It should be noted that, although the LRSP and SRSP modes are both a positive index modes, they exhibit opposite field symmetry.

As an example of the asymmetric adiabatic tapered waveguide shown in fig. 3.17, let us consider the DMD waveguide with $\alpha = 15°$, $\varepsilon_1 = 2.25$, silver as the plasmonic material with $\varepsilon_2(k_0)$ according to the Drude model with parameters as in [57], and $\varepsilon_3 = 3.9$. In this case, the conditions for the existence of low-loss LRSP mode $k^{\mathrm{LRSP}} > k_0^{|\varepsilon 2|=|\varepsilon 1|}$ and $k^{\mathrm{LRSP}} > k_0^{|\varepsilon 2|=|\varepsilon 3|}$ are satisfied for thickness $t < 14$ nm. Due to different effective indices, the SRSP mode at the tip can be exclusively excited via the surface plasmon mode at the $\varepsilon_3$|Ag ($\varepsilon_3 > \varepsilon_1$) interface, whereas the excitation of the LRSP mode at the tip is possible only via the surface plasmon at the opposite interface $\varepsilon_1$|Ag ($\varepsilon_3 > \varepsilon_1$). Detailed analysis of the evolution for each mode is presented in the published Author's works.

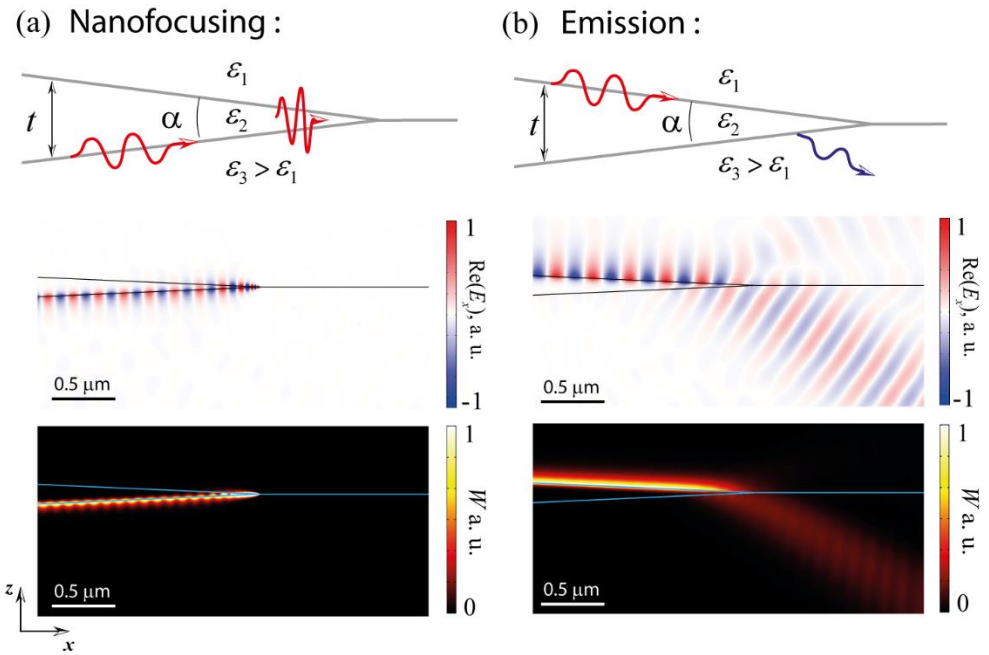


**Figure 3.18.** (a) The electric field component $E_x$ and the time averaged energy flow $W$ at $k_0 = 1.25\times10^7$ m$^{-1}$ for the plasmon, propagating along the $\varepsilon_3|\varepsilon_2$(Ag) interface of the tapered DMD waveguide and experiencing nanofocusing at the tip due to coupling to the SRSP mode. (b) Same as in (a) for the plasmon, propagating along the $\varepsilon_1|\varepsilon_2$(Ag) interface and coupling to the free-space mode via the leaky LRSP mode of the DMD waveguide. Waveguide materials in both cases are the same as noted in the text.

Figure 3.18(a) shows the COMSOL simulation results when the surface mode is excited at the $\varepsilon_3|$Ag ($\varepsilon_3 > \varepsilon_1$) interface. As expected in this case, nanofocusing is experienced at the tip, which is a direct consequence of the mode coupling to the high index SRSP mode – the same phenomenon illustrated in Fig. 3.14 and Fig. 3.15. At the same time, Fig. 3.18(b) demonstrates the way that the mode which is excited at the $\varepsilon_1|$Ag ($\varepsilon_3 > \varepsilon_1$) interface effectively couples into the free space radiative mode

via a coupling with the low index LRSP mode, whereby it becomes leaky at a small $t$ [54]–[56]. This effect is not usually observed at tapered waveguide since it requires special conditions for the LRSP mode excitation. The radiation can be reciprocally replaced by coupling of incident light into the plasmonic mode at the $\varepsilon_1$|Ag ($\varepsilon_3 > \varepsilon_1$) interface.

Demonstrated in Fig. 3.18 ways to couple plasmons to the free-space mode and at the same time obtain nanofocusing can be realized simultaneously in combined systems to provide direct coupling of light into the high-index graphene plasmons (including the GEP and 1DSPP modes). In this case coupling prism would not be necessary.

## 3.4 Conclusion

In summary, the existence of a fundamental 1D plasmonic mode of 1D metal-dielectric interfaces in 2D systems (so called 1DSPP) has been predicted. The effective index of 1DSPPs diverges asymptotically towards a cutoff as the magnitudes of the susceptibilities on the two sides of the interface become equal, in striking analogy to conventional SPPs at bulk metal-dielectric interfaces. On a sample 2D metal-dielectric graphene/graphene platform, highly sensitive tunability of the 1DSPP dispersion was demonstrated via the doping of either graphene domain, which further allowed for the achievement of spatial confinement of electric-field intensity to regions orders of magnitude smaller than that of the plasmonic excitations of a bare graphene edge. The unique and tuneable cutoff behaviour of 1DSPPs thus presents a means for dramatic enhancement of light confinement in 2D systems over other 1D or quasi-1D excitations, such as GEPs or plasmonic excitations of graphene *p-n* junctions. For example, at frequency of 50 THz, we predicted tremendous localisation of the electric-field intensity of the 1DSPP to a modal area more than one million times smaller than the diffraction limit. As a new member of the existing plasmon family of bulk plasmons, surface plasmons, localised plasmons, a new field of low-dimensional plasmonics is foreseen based on 1DSPPs, particularly branching out into various multi-material 2D systems.

The efficient excitation of high-index plasmonic modes in graphene is still to be experimentally demonstrated, however several approaches have been analytically and numerically tested, including the tapered tree-layer plasmonic waveguides. The asymmetric tapered waveguides provide means for direct coupling of light into the plasmons.

## Chapter 4

# Transverse electric mode in graphene under Otto excitation scheme

In this chapter, properties of an unusual TE mode in graphene are studied from the perspective of its experimental detection which has not been demonstrated yet. First, the Otto excitation scheme is investigated as a route towards the experimental detection of the TE mode in graphene. From the solution of the dispersion equation, it is demonstrated that the TE mode supported by graphene in Otto configuration can be successfully excited even at room temperature and moderate graphene quality when multilayer graphene stakes are used.

## 4.1 Otto excitation of TE mode in single-layer graphene

### 4.1.1 Reflection coefficient in three-layer Otto scheme

The considered Otto excitation scheme is shown in Fig. 4.1: an effectively semi-infinite high-index dielectric medium (e.g., a coupling prism) with the refractive index $n_1 = 2$ is juxtaposed at the plane $x = 0$ with a semi-infinite low-index dielectric medium of refractive index $n_2 = 1.5$ in which a graphene layer with the sheet conductivity (see Chapter 2) $\sigma = \sigma' + i\sigma''$ occupies the $x = d$ plane. A TE-polarized plane wave is incident onto the $n_1|n_2$ interface at an angle θ. The *ansatz* is made that the electric field in each medium $m$ = 1,2,3 takes the form $\mathbf{E}^{(m)} = \hat{\mathbf{y}} E_m(x)\exp(iqz - i\omega t)$, where,

$$\begin{aligned} E_1(x) &= A_1\exp(ik_1 x) + B_1\exp(-ik_1 x), x < 0; \\ E_2(x) &= A_2\exp(-\kappa[x-d]) + B_2\exp(\kappa[x-d]), 0 < x < d; \\ E_3(x) &= A_3\exp(-\kappa[x-d]) + B_3\exp(\kappa[x-d]), x > d. \end{aligned} \tag{4.1}$$

Substituting the *ansatz* into the Helmholtz equation $(\nabla^2\mathbf{E}^{(m)} + k_0^2\varepsilon\mathbf{E}^{(m)} = 0$, where $k_0 = \omega/c$) we obtain $k_1 = \sqrt{k_0^2 n_1^2 - q^2}$ and $\kappa = \sqrt{q^2 - k_0^2 n_2^2}$, noting that $q = n_1 k_0 \sin(\theta)$ is the projection of the incident wavevector onto the $z$-axis. Assuming the harmonic time dependence $\exp(-i\omega t)$ of the magnetic field **H,** substituting into the Maxwell curl equation $\nabla\times\mathbf{E} + \mu_0\partial\mathbf{H}/\partial t = 0,$ applying the electromagnetic boundary conditions $\hat{\mathbf{x}}\times\left(\mathbf{E}^{(m+1)} - \mathbf{E}^{(m)}\right) = 0$ and $\hat{\mathbf{x}}\times\left(\mathbf{H}^{(m+1)} - \mathbf{H}^{(m)}\right) = \mathbf{K}$ at the interfaces, noting that $\mathbf{K}(x = 0) = 0$ and $\mathbf{K}(x = d) = \sigma\mathbf{E}(x = d)$, and taking $B_3 = 0$ (i.e. absence of a reflected wave in medium 3), we obtain the reflection coefficient of the incident wave $R = |r|^2$ ($r = B_1/A_1$) with

$$r = -\frac{\kappa\left[\Lambda\cosh(\kappa d)+\kappa\sinh(\kappa d)\right]+ik_1\left[\kappa\cosh(\kappa d)+\Lambda\sinh(\kappa d)\right]}{\kappa\left[\Lambda\cosh(\kappa d)+\kappa\sinh(\kappa d)\right]-ik_1\left[\kappa\cosh(\kappa d)+\Lambda\sinh(\kappa d)\right]}, \tag{4.2}$$

where $\Lambda = \kappa - i\mu_0\omega\sigma$, and $\mu_0$ is the vacuum magnetic permeability. We note that equation (4.2) can also be derived using the transmittance matrix technique [29], [58].

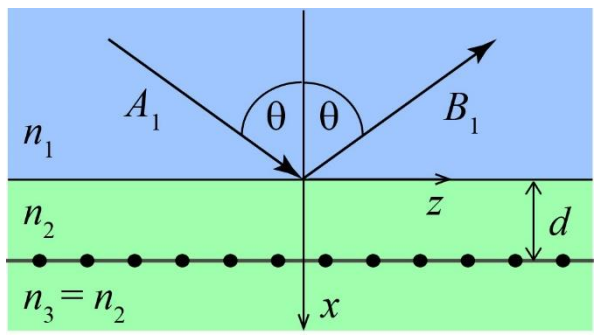


**Figure 4.1.** Three-layer Otto excitation scheme in ATR regime.

Figure 4.2 shows the angular reflectance distribution $R(\theta)$ staggered for $d$ from $d/\lambda = 0$ (bottom curve) to $d/\lambda = 30$ (top curve), and $\sigma \sim 0.5\sigma_u - i\sigma_u$. It can be seen that a sharp minimum in $R(\theta)$ emerges at the critical angle $\theta_c$ of the $n_1|n_2$ interface [$\theta_c = \text{asin}(n_2/n_1)$] when $d/\lambda > \approx 5$. The minimum becomes broadened as $d$ increases while at the same time shifting to the right, yet remaining very close to $\theta_c$ within $\Delta\theta = \theta - \theta_c \sim 0.001$deg. The expected angular range of TE mode excitation can be approximated from the symmetric semi-infinite case (i.e. $d \to \infty$), $\theta_{TE} \sim \text{asin}(n_{eff}/n_1)$, which gives $\Delta\theta \sim 0.001$deg, thus suggesting that the reflection minimum could be a consequence of the excitation of TE modes.

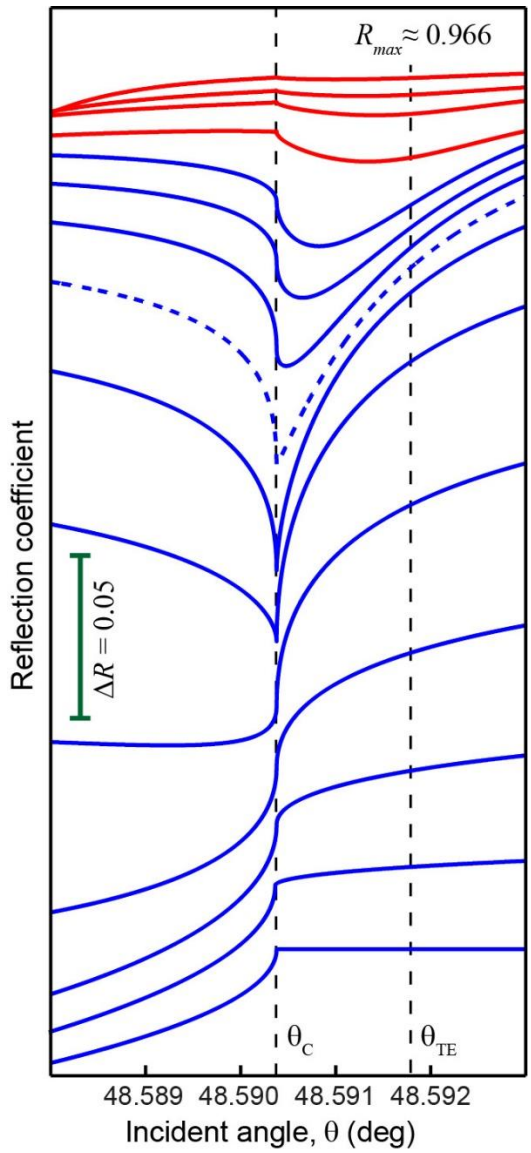


**Figure 4.2.** Angular reflectance distribution $R(\theta)$ for different values of thickness $d$.

To eliminate the possibility that the reflection minimum is a trivial consequence of loss in the graphene layer (i.e. $\sigma' > 0$), we also plot $R(\theta)$ (at $d/\lambda = 7$) in Fig. 4.3 for when the incident wave is TM polarized (for both $\sigma'' > 0$ and $\sigma'' < 0$ – dashed curve

Fig. 4.3; the derivation of the TM case is analogous to the above replacing **E** with **H** in equation (4.1)), and TE polarized with $\sigma'' > 0$. The evident absence of a distinct minimum in $R(\theta)$ in the vicinity of the critical angle except for when the incident wave is TE polarized and $\sigma'' < 0$ further suggests that the reflection minimum is solely due to the TE mode excitation.

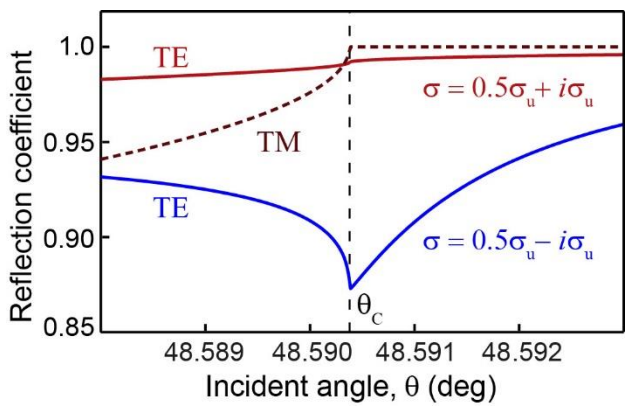


**Figure 4.3.** Reflectivity R($\theta$) for case of TE (solid curves) and TM (dashed curve) incident wave polarization and positive/negative sign of Im($\sigma$); $d/\lambda = 7$.

Noting that in Fig. 4.2, $R_{max} \approx 0.966$ (at large angles $\theta > \theta_c$ $R_{max} \neq 1$ due to absorption in graphene), we find that the reflectance contrast does not exceed $\Delta R/R_{max} \sim 10\%$ ($\Delta R = R_{max} - R_{min}$, $R_{min} = \min[R(\theta \geq \theta_c)]$), and $R_{min} > 0$ for all $d$. Therefore, critical coupling [59], [60] of the incident wave to the TE mode (which would correspond to $R_{min} = 0$) is not achieved. Furthermore, noting the extremely narrow angular width of the reflection minimum that is $\delta\theta < 0.001$deg, which exceeds the angular resolution limit of typical SPP detectors (see for example, Table 2 in [61], and [62]), the Otto excitation and detection of the TE mode in the considered single-layer graphene even at $T = 80$K would be a challenge.

### 4.1.2 Numerical analysis of TE mode dispersion

A theoretical understanding of the dispersive properties of TE mode supported by graphene in an Otto configuration will suggest routes toward loosening the experimental conditions required for their experimental detection. To this end we solve the dispersion relation of leaky TE mode in the asymmetric three-layer system of Fig. 4.1. The dispersion relation is obtained on setting $A_1, B_3 = 0$ in equation (4.1), substituting into the boundary conditions on **E** and **H**, and then setting the resulting 4×4 determinant of coefficients $B_1, A_2, B_2, A_3$ equal to zero, thus arriving at:

$$\exp(-2\kappa d) = \frac{k_1 + i\kappa}{k_1 - i\kappa} \frac{i2\kappa + \omega\mu_0\sigma}{\omega\mu_0\sigma}. \tag{4.3}$$

Equation (4.3) is solved numerically for complex $q = q' + iq''$ under the condition that $\mathrm{Re}(\kappa) \geq 0$ which ensures that the mode electric field is exponentially bound to the graphene layer and leaks only into propagating modes of medium 1. The expected angle of excitation of the leaky TE mode, $\theta_{TE}$, is obtained from the phase matching condition $q' = n_1 k_0 \sin(\theta_{TE})$ [48], [58].

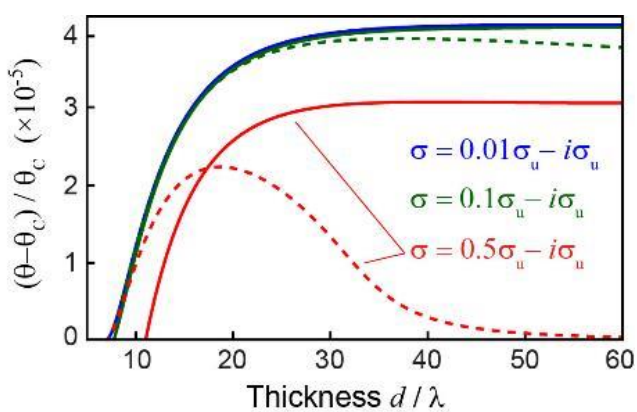


**Figure 4.4.** *d*-dependence of normalized angular deviation of $\theta_{TE}$ (solid curves) and $\theta_{Rmin}$ (dashed curves) from the critical angle $\theta_c$.

In Fig. 4.4, the normalized deviation from the critical angle of $\theta_{TE}(d)$ (solid curves) is plotted, and same for the angle $\theta_{Rmin}$ (dashed curves) corresponding to the minimum of $R(\theta \geq \theta_c)$ (i.e. $R(\theta_{Rmin}) = R_{min}$), for the conductivity $\sigma = 0.5\sigma_u - i\sigma_u$ (red curves). To observe contrasting behavior, we also show data for two experimentally challenging (e.g. very-low temperature) conductivities exhibiting smaller internal loss $\sigma'$: $\sigma = 0.1\sigma_u - i\sigma_u$ (green curves) and $\sigma = 0.01\sigma_u - i\sigma_u$ (blue curves).

Firstly, we note that each curve $\theta_{TE}(d)$ asymptotically approaches a fixed value at large $d$, which expectedly corresponds exactly to the wavenumber of the TE mode in the symmetric semi-infinite structure with refractive index $n_2$.

Secondly, we note that all curves $\theta_{TE}(d)$ collapse to the critical angle $\theta_c$ at a particular value $d = d_{cut}$ – see also the dashed curve in Fig. 4.2 corresponding to $d/\lambda = 7$. This value of $d$ constitutes a cutoff at which the electric field of the TE mode becomes completely delocalized (i.e. $\kappa(d = d_{cut}) = 0$) and leaks into the propagating mode of medium 3 (see also Fig. 4.7). The cutoff can be easily obtained from equation (4.3) taking $\kappa \rightarrow 0$ and Taylor expanding the LHS to first order. In the limit of zero loss ($\sigma' = 0$) and when $k_1 >> \omega\mu_0|\sigma''|$, we obtain $d_{cut}/\lambda \approx c\varepsilon_0/(2\pi|\sigma''|)$ which gives $d_{cut}/\lambda \approx 7$ when $\sigma'' = -\sigma_u$, and matches very well with the distance at which blue and green curves in Fig. 4.4 collapse to critical angle, i.e. those corresponding to small internal loss ($\sigma' << |\sigma''|$).

Thirdly, while we note excellent quantitative agreement between $\theta_{TE}(d)$ and $\theta_{Rmin}(d)$ to within < 0.01% at each of the considered conductivities, there is evident mismatch when $\sigma' = 0.5\sigma_u$ (red solid and dashed curves in Fig. 4.4). This is related to a strong under-coupling [60] of the incident wave to the TE mode at large internal loss. To illustrate this, in Fig. 4.5 we plot the $d$-dependent internal loss coefficient $q_{int}''$ (solid curves) and radiative loss coefficient $q_{rad}''$ (dashed curve) of the TE mode

at each of the three considered conductivities; the data for each conductivity is plotted over the domain $d \geq d_{cut}$. The quantity $q_{rad}''$ is obtained from the solution of equation (4.3) after setting $\sigma' = 0$ in which case $q_{rad}'' = q''$ i.e. the only loss mechanism is radiative loss. The quantity $q_{int}''$ is obtained on introducing $\sigma' \neq 0$, solving equation (4.3), and taking $q_{int}'' = q'' - q_{rad}''$.

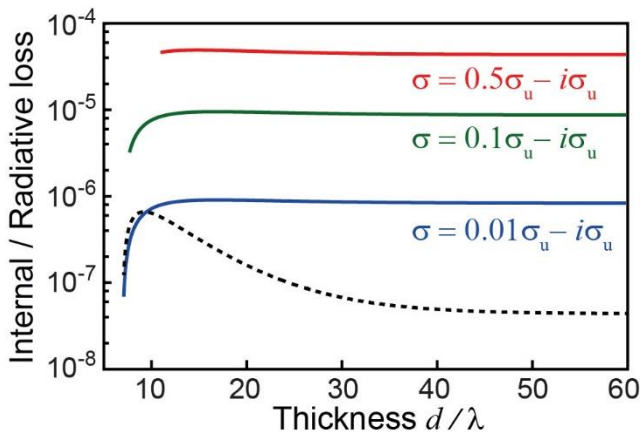


**Figure 4.5.** *d*-dependence of TE mode internal ($q_{int}''$; solid curves) and radiative ($q_{rad}''$; dashed curve) propagation loss.

Interestingly, when the conductivity takes the realistic value $\sigma = 0.5\sigma_u - i\sigma_u$, at all $d > d_{cut}$, the internal loss is several orders of magnitude greater than the radiative loss (Fig. 4.5), which is far from the critical coupling regime (critical coupling occurring when $q_{int}'' = q_{rad}''$ [59]). Considering that the radiative loss is reciprocal to the radiative coupling gain, we see that the TE mode is in fact strongly under-coupled. At the same time, it is interesting to note that cumulatively (i.e. internal plus radiative loss), the mode itself exhibits very low propagation loss, with a normalized (to the

mode wavelength $\lambda_p$) propagation length $l \approx 1/q'' = \sim 1000\lambda_p$. The low loss of the mode is responsible for the narrow angular width of the minimum in $R(\theta)$ [48], yet the existence of a large cutoff thickness $d_{cut}$ forbids the incident wave from effectively driving the mode.

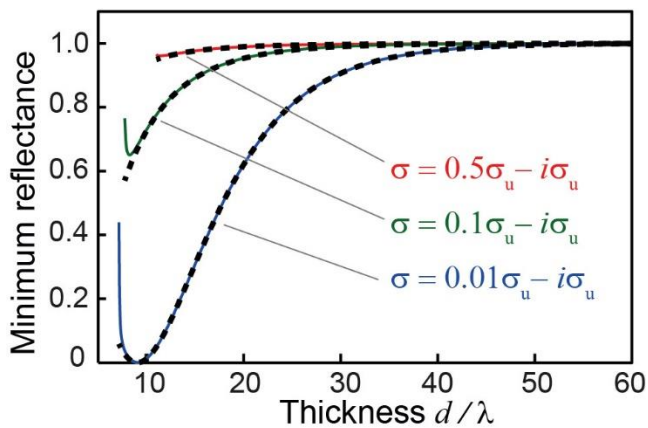


**Figure 4.6.** *d*-dependence of minimum reflectance $R(\theta_{min})$ (solid curves) and $R(\theta_{TE})$ (black dashed curves).

We expect that increased coupling of the incident wave to the TE mode could be achieved by reducing the internal loss ($\sigma'$) of the graphene (and thus, $q_{int}''$), such that the mode internal loss becomes comparable to the radiative loss – this is demonstrated by the green and blue curves in Figs. 4.5 and 4.6, corresponding respectively to $\sigma' = 0.1\sigma_u$ and $\sigma' = 0.01\sigma_u$. For small internal loss such as $\sigma' = 0.01\sigma_u$, the critical coupling condition [59], [60], for which the internal loss becomes equal to the radiative loss, can be satisfied (see blue curve intersecting with black dashed curve in Fig. 4.5), and $\theta_{TE}(d)$ and $\theta_{Rmin}(d)$ almost perfectly match (Fig. 4.4). Naturally, we expect a zero in $R(\theta)$ when $q_{int}'' = q_{rad}''$ is satisfied; this is illustrated by the blue

curve in Fig. 4.6. It is evident from Fig. 4.5 that when $\sigma'$ is further reduced, the radiative and internal mode loss will become comparable or equal at larger values of the film thickness $d$, and thus evidence of coupling of the incident wave to the TE mode is seen at larger film thickness (see Fig. 4.6). On the other hand, in the lossless case ($\sigma' = 0$), the evidence of TE mode coupling is absent from the angular reflectance distribution since there is no light absorption in the graphene layer. Thus, decreasing the internal loss of graphene significantly increases coupling between the mode and incident wave, resulting in strong reduction of the reflectance at the TE mode resonance. It is unusual that, although the mode itself exhibits extremely weak internal losses, a route to its more convenient experimental detection (i.e. increased contrast of the reflectance minimum) would be to further reduce the internal loss of the single-layer graphene. However, to do so would require the cooling of the graphene to very low temperatures.

### 4.1.3 Cutoff dynamics of TE mode

To obtain insight into the cutoff dynamics of Otto excited TE modes, in Fig. 4.7 we show the mode electric field intensity distribution $|E_{2,3}(x - d)|^2$ at several values of $d$, as determined from substituting $q(d) = q' + iq''$ (i.e. with $q$ obtained from equation 4.3) into the boundary conditions with $A_1, B_3 = 0$ and normalizing so that $A_3 = 1$. When $d >> d_{cut}$, we observe an almost symmetric field distribution (about $x = d$) which approaches that of the TE mode of the semi-infinite symmetric structure. As $d \rightarrow d_{cut}$ the field becomes increasingly asymmetric, rapidly delocalizing from the graphene layer in medium 3, while slowly becoming more localized in medium 2. The cutoff $d = d_{cut}$ corresponds to complete delocalization of the field and leakage of the mode into propagating waves in medium 3 (in the positive-$x$ direction).

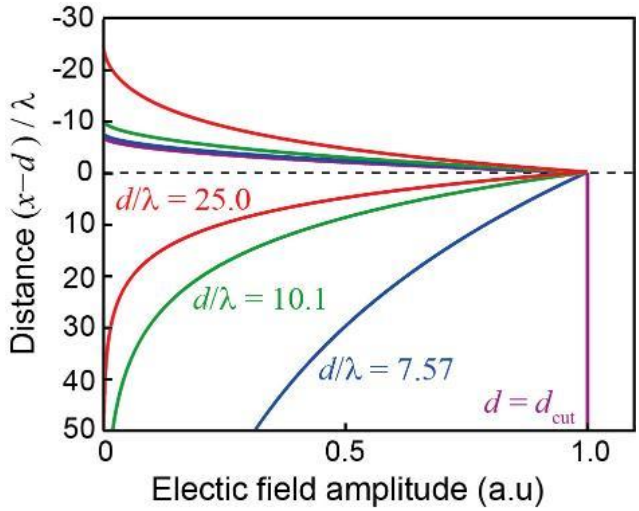


**Figure 4.7.** Electric field intensity profile of asymmetric TE mode illustrating cutoff behavior in Otto configuration at indicated $d$. The dashed line $x = 0$ marks the position of the graphene layer.

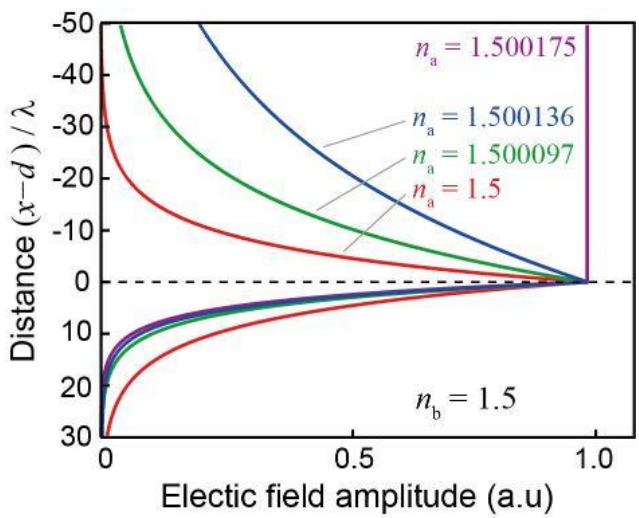


**Figure 4.8.** Electric field intensity profile of asymmetric TE mode illustrating cutoff behavior in asymmetric semi-infinite structure at indicated values of $n_a$ and $n_b$. The dashed line $x = 0$ marks the position of the graphene layer.

To contrast, we also show the electric field distribution of TE mode supported by a graphene sheet (at $x = d$) sandwiched between two semi-infinite dielectrics with the respective refractive indices $n_a$ ($x < d$) and $n_b$ ($x > d$), referred to as the asymmetric semi-infinite structure – Fig. 4.8. We note that the cutoff behavior in the asymmetric semi-infinite structure holds qualitative similarity to that of the Otto structure, except comparing each case shows that the mode becomes delocalized toward opposite sides of the graphene layer (i.e. toward or away the side containing the high index medium). The cutoff dynamics of TE modes in the Otto configuration are further revealed on calculating the $z$-component of power flow in medium 1, 2 and 3 given respectively by $P^{(1)} = \int_{-\infty}^{0} S_z^{(1)} dx$, $P^{(2)} = \int_{0}^{d} S_z^{(2)} dx$ and $P^{(3)} = \int_{d}^{\infty} S_z^{(3)} dx$, where $S^{(m)} = (1/2)\mathrm{Re}[\hat{\mathbf{z}}\cdot(\mathbf{E}^{(m)}\times\mathbf{H}^{(m)}*)]$ is the time-averaged $z$-component of Poynting vector in medium $m$, and the electric fields are given by equation (4.1) with $A_1, B_3 = 0$. In the limit of weak-leakage of the mode ($q'' << q'$), we have $P^{(1)} << P^{(2)} + P^{(3)}$ (since $P^{(1)}$ contains only the leakage wave prior to the cutoff), and $P^{(2)} + P^{(3)} \approx C$ where $C$ is a $d$-independent constant. We find in the limit $\kappa \to 0$ that $P^{(2)} \approx |A_3|^2 d$, and $P^{(3)} \approx |A_3|^2/2\kappa$.

Thus we see that as the cutoff (i.e. corresponding to $\kappa \to 0$) is approached, the mode amplitude ($A_3$) approaches zero (to ensure that $C$ is finite), and $P^{(2)}/P^{(3)} \approx 2\kappa d \to 0$, showing that the mode energy is mostly found in medium 3 ($x > d$). Furthermore, the power cutoff dynamics are independent of the optical contrast across the interface separating medium 1 from 2 (i.e. $\Delta n = n_1 - n_2$), and depend only on $n_2$ (recalling that $\kappa = \sqrt{q^2 - k_0^2 n_2^2}$), whereas the cutoff behavior in the semi-infinite anti-symmetric structure is very sensitive to the optical contrast [30]; the former is also consistent with the absence of the optical contrast from the expression for the cutoff thickness ($d_{cut}/\lambda \approx c\varepsilon_0/(2\pi|\sigma''|)$).

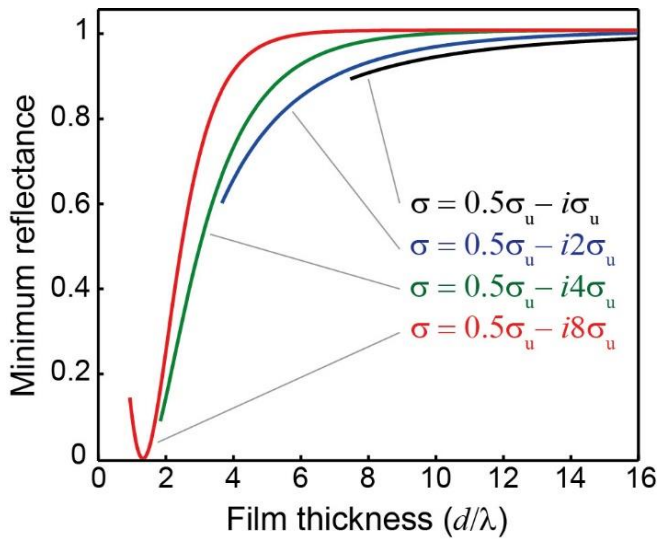


**Figure 4.9.** *d*-dependence of minimum reflectance R($\theta_{min}$).

On the other hand, we find that reducing the optical contrast can increase the coupling efficiency of the incident wave to the TE mode owing to increased penetration of the totally reflected incident beam (i.e. for $\theta > \theta_C$) into medium 2. We also point out that the cutoff itself, inversely proportional to $|\sigma''|$, suggests a second route (besides reducing the internal loss) to more convenient detection of TE modes in graphene. Indeed, increasing $|\sigma''|$ will reduce the cutoff thickness and allow increased coupling between the incident wave and the TE mode. This is demonstrated in Fig. 4.9, where we plot $R(\theta_{min})$ for increasing values of $|\sigma''|$ while keeping the internal loss fixed at $\sigma' = 0.5\sigma_u$ (similarly to Fig. 4.6, each curve is terminated at the respective values of $d = d_{cut}$). A significant reduction of the reflectance reveals enhanced coupling of the incident wave to the TE mode at increasing values of $|\sigma''|$, including critical coupling for when $\sigma'' = -8\sigma_u$; the cutoff prevents the critical coupling condition from being satisfied when $|\sigma''| < \approx 8\sigma_u$. The TE coupling enhancement is further demonstrated in Fig. 4.10, which shows the

angular reflectance distribution at those values of $d$ providing the minimum reflectance (as obtained from Fig. 4.9). Yet considering that $|\sigma''| > 1$ is difficult to achieve in practice except at very low temperature, in section 4.2 we suggest and demonstrate that multi-layer graphene stacks is a way to increase the effective conductivity of graphene toward providing less strict experimental conditions for the detection of TE modes.

Finally, we note that it was recently predicted that the TE mode supported in an optical cavity exhibits a cutoff with respect to the cavity width [63]. From this context, our results demonstrate that a TE mode cutoff is exhibited not only in an enclosed cavity but also when the TE mode is attempted to be confined on only one side by a high index medium.

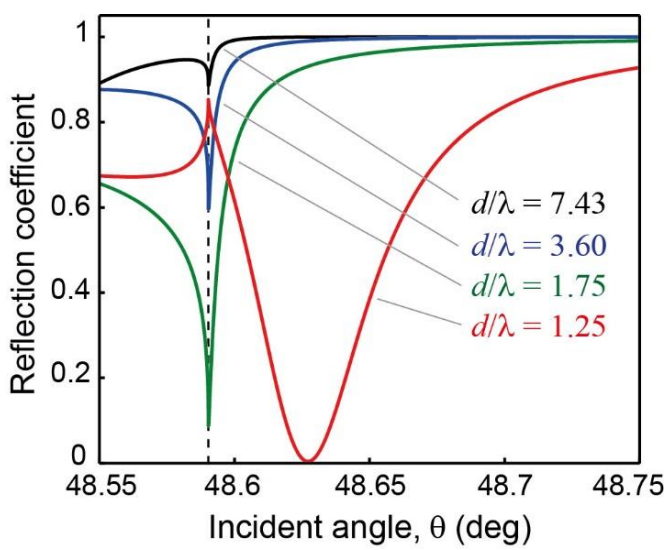


**Figure 4.10.** Angular reflectance distributions $R(\theta)$ corresponding to indicated values of $d$.

## 4.2 Enhanced coupling to TE mode in multilayer graphene stack

In section 4.1 we predicted that the Otto excitation of TE modes in a single-layer graphene can lead to a minimum in the angular reflectance distribution at the critical angle with a contrast $\Delta R/R_{\max}$ ~10%, although which would require a very high angular resolution exceeding ~0.001deg to experimentally detect. In this regard, we seek a means to increase the angular width and depth of the reflection minimum to facilitate the feasible experimental detection of TE modes in graphene. In this section we propose that stacking multiple single-layer graphene [26], [64] could provide both a widening and deepening of the reflectance minimum owing to an effective increase of the graphene conductivity. For example, in graphene insulator stacks [26], [65] or multi-layer graphene obtained from layer-by-layer transfer of single-layer graphenes [64], electronic decoupling between neighboring graphene layers provides an effective conductivity increase according to $\sigma_N = N\sigma$ [26], [64] as the distance between neighboring layers approaches zero; $N$ is the number of single-layer graphenes in the stack, $\sigma$ is the sheet conductivity of a single-layer graphene, and $\sigma_N$ is the effective sheet conductivity of the graphene multi-layer stack. We note that a random crystalline orientation between neighboring graphene layers [26], [64] provides the electronic decoupling [66] (and $N\sigma$ behavior), while for bi-layer or few layer graphene, the expression for conductivity becomes increasingly complicated (see for example [28]).

We start at an Otto configuration with two single-layer graphenes (a two-layer system) – the structure is the same as Fig. 4.1 except with an additional single-layer graphene inserted at the plane $x = d + \Delta$. Insight into the TE mode dynamics as the structural transition is made from the two-isolated-layer system (i.e. $\Delta > 0$) to the

two-layer-stack (i.e. as $\Delta \rightarrow 0$) is obtained by solving the dispersion equation of TE modes supported by the two-layer system. The dispersion equation is derived in determinant form following the same method in section 4.1 after inserting an additional layer ($d < x < d + \Delta$) and boundary condition (i.e. at the additional graphene layer) at $x = d + \Delta$. Expectedly, we find that the dispersion equation has two solutions corresponding to an even or odd coupled mode (i.e. with equal or opposing sign of electric field at either graphene layer) each comprising the even or odd coupling between the TE modes supported by each single layer system (i.e. one with a single-layer graphene only at $x = d$, and the other only at $x = d + \Delta$).

The $d$-dependence of the deviation of the TE coupled-mode mode effective index (with respect to, and normalized to the bulk effective index: $(n_{\text{eff}}\text{-}n_2)/n_2$, which equals to zero at $d = d_{\text{cut}}$) of both even (dashed) and odd (dot-dashed) mode solutions is shown in Fig. 4.11 at indicated values of normalized inter-layer separation ($\Delta/\lambda$), and when the single-layer graphene conductivity is fixed at $\sigma = 0.5\sigma_{\text{u}} - i\sigma_{\text{u}}$. As $\Delta$ increases, we see that the odd mode effective index converges exactly to that of the mode supported by the single layer system (marked $N = 1$, thick red solid line), in which case the mode field is bound only to the upper graphene layer (i.e. at $x = d$). For the odd mode, coupling induced perturbation of the effective index (evident for smaller values of $\Delta$) rapidly increase $d_{\text{cut}}$ (the $d/\lambda$-intercept in Fig. 4.11) which would significantly reduce coupling of an incident wave to the odd TE mode. Thus we conclude that the odd TE mode would likely be experimentally undetectable at the considered single-layer graphene conductivity.

In contrast, modal coupling rapidly increases the effective index of the even TE mode, starting at that of the TE mode of the isolated lower graphene layer (see the thick red dashed curve in Fig. 4.11, which corresponds to the symmetric semi-infinite

structure), and in the limit that $\Delta \to 0$, converging to that of a single layer system with an effective conductivity $\sigma_2 = 2\sigma$ and a halved (i.e. as compared to the single-layer case) cutoff thickness $d_{cut}/\lambda = 3.5$. As we predicted in section 4.1.3, a decreased cutoff thickness (at increased $|\sigma''|$) provides increased coupling of the TE mode to the incident wave.

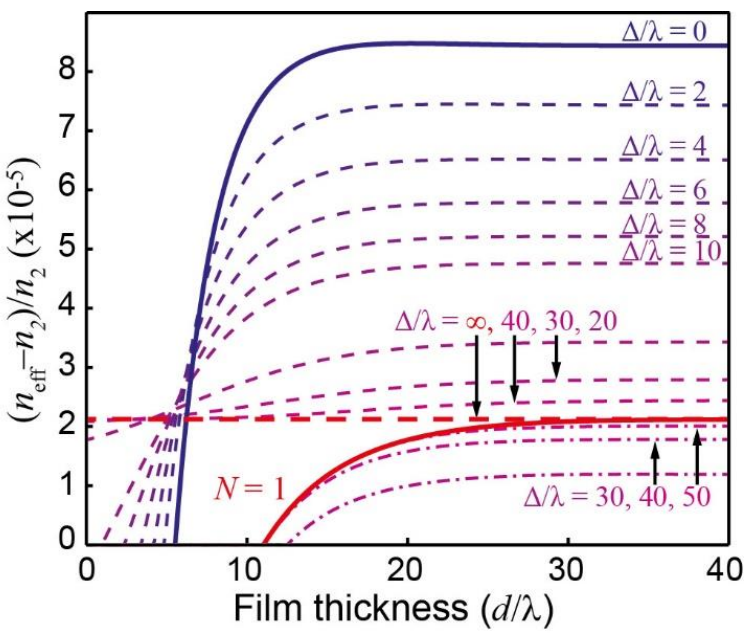


**Figure 4.11.** *d*-dependent normalized effective index deviation of even (dashed) and odd (dot-dashed) TE coupled-modes of an Otto system with two single-layer graphenes at indicated values of the inter-layer distance, Δ. The conductivity of each single-layer graphene is $\sigma \sim 0.5\sigma_u - i\sigma_u$. The solid blue and red curves correspond to a single layer Otto system with the graphene conductivity $\sigma \sim 2(0.5\sigma_u - i\sigma_u)$, and $\sigma \sim 0.5\sigma_u - i\sigma_u$, respectively. The thick red dashed curve corresponds to the semi-infinite symmetric structure.

To demonstrate increased coupling of an incident wave to TE modes in $N$-layer graphene stacks, in Fig. 4.12 we plot the angular reflectance distribution $R(\theta)$ about the critical angle (vertical dashed line) for when $d = d_{cut}$ at the respective values of $N$ (as indicated in the figure). These curves are obtained from the transmittance matrix method [29], [58] with the inter-layer spacing $\Delta/\lambda = 0.001$. It is immediately evident that the reflection minimum significantly widens and deepens as the numbers of layers in the graphene stack ($N$) increases, even to the extent that critical coupling is achieved (i.e. $R(\theta_c) \approx 0$) when $N = 20$. The angular width of the reflection minimum is increased by two orders of magnitude from $\Delta\theta \sim 0.001$deg in the single layer case to $\Delta\theta \sim 0.1$deg when $N \sim 10$, providing for much easier experimental detection (see also inset of Fig. 4.12). We also show an example case of a 20-layer graphene stack at room temperature ($T = 300$K) for which we have taken the single layer graphene conductivity as $\sigma = 0.5\sigma_u - 0.5i\sigma_u$ (see Fig. 2.2). Interestingly, an appreciable contrast of the reflection minimum ($\Delta R/R_{max} \approx 70\%$) is obtained while preserving the broad angular width. These results are therefore promising toward the experimental detection of TE modes in graphene including at room temperature.

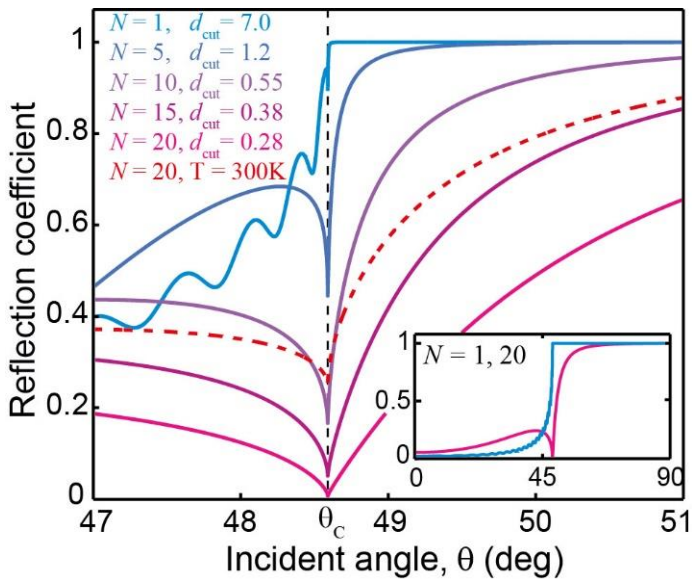


**Figure 4.12.** Angular reflectance distributions $R(\theta)$ for an Otto system with an $N$-layer graphene stack ($\Delta/\lambda = 0.001$) at respective $d = d_{cut}(N)$ and with $\sigma \sim 0.5\sigma_u - i\sigma_u$ (solid curves; $T \sim 80$K) and $\sigma \sim 0.5\sigma_u - i0.5\sigma_u$ (dashed red curve; $T \sim 300$K). Inset: wide-angle comparison of single-layer and 20-layer reflectance distributions over $0 < \theta < 90$ (deg) with $\sigma \sim 0.5\sigma_u - i\sigma_u$.

## 4.3 Conclusion

In this chapter, an Otto configuration as a mean for the experimental detection of the TE mode in graphene has been investigated. From solution of its dispersion equation, we demonstrated that the TE mode supported by graphene in an Otto configuration exhibits a cutoff at a particular thickness of the film between the graphene layer and the coupling prism. While the TE mode exhibits very weak internal and radiative losses, the existence of the cutoff is shown to prevent its efficient coupling to an incident wave. These two factors produce a minimum in the angular reflectance distribution which is both low contrast ($\Delta R/R_{\max} < 10\%$) and of exceptionally narrow angular width ($\Delta\theta \sim 0.001$deg), hindering the experimental detection of TE modes in single-layer graphene at finite temperatures. To address this issue, we proposed the Otto excitation of the TE mode in a multi-layer stack of single-layer graphenes. Owing to the effective increase of the graphene conductivity by a factor equal to the number of layers (i.e. $\sigma_N = N\sigma$), we demonstrated significantly increased coupling of TE mode to an incident wave, including orders-of-magnitude increase in the angular width and reflectance contrast of the TE mode resonance. Our results suggest that an Otto scheme with a graphene multi-layer stack provides the first recognized platform for the feasible detection of the TE mode in graphene at room temperature. Experimental detection of the TE mode in graphene is of significant fundamental importance, and the experimental implementation of the suggested Otto scheme is presented in the next Chapter 5. We foresee that the proposed scheme could provide a realistic platform for a new type of SPP detector based on the narrow angular width of the TE mode resonance.

## Chapter 5

# Experimental detection of transverse electric mode in graphene

In this chapter, based on theoretical and numerical observations of Chapter 4, the experimental means to detect the TE mode in graphene are proposed, and experimental results are discussed. Successful direct optical observation of the TE mode is demonstrated for the first time, ten years after its prediction, supported with theoretical and numerical analysis of the obtained data.

## 5.1 Otto excitation of TE mode in single-layer graphene

As it is shown in Chapter 2, in the spectral transition region, the imaginary part of graphene's conductivity (Im[$\sigma$] = $\sigma''$) changes sign from positive to negative, having its minimum at $\hbar\omega = 2E_F$ (see Fig. 2.2). The negative sign of $\sigma''$ has been associated with manifestation of the TE propagating electromagnetic mode in both single- and bi-layer graphene [7], [28], [30], contrary to conventional transverse magnetic plasmonic modes in metals and graphene existing exclusively when $\sigma'' > 0$. Yet, the main difficulty in detecting the TE mode is that its effective index is very close (with optical contrast as low as $\Delta n \sim 0.001$) to that of propagating wave in the bulk material surrounding the graphene, which imposes a necessity of extremely precise phase matching with an excitation wave.

Here, for the first time ten years after its prediction, direct optical probing of the TE mode supported by graphene is demonstrated, employing modified Otto configuration that allows very precise phase matching of the incident wave to the TE excitation, and electrostatically doped multi-layer graphene stacks at room temperature, performed at the telecommunication wavelength $\lambda_0 = 1.55$ μm.

The physical nature of TE excitations in graphene can be understood as magnetic dipole waves, i.e. self-sustained oscillations of current (Fig. 1.7) with no spatial charge density perturbation, while conventional TM plasmons are an electric dipole waves. As demonstrated in Chapter 4, the small effective index of the TE mode makes it easily accessible to Otto excitation via evanescent field in attenuated total reflection (ATR) regime [58], [67] even at room temperature [7], when doped graphene is sandwiched between the two dielectric layers of same refractive index.

However, necessity of doping (i.e. special techniques of thereof) makes it

difficult to provide symmetry between indices of materials above ($n_2$) and below ($n_3$) the graphene layer (Fig. 4.1). Therefore, the TE mode excitation scheme where graphene is situated between dielectrics with asymmetric indices, $n_2 > n_3$, and placed at distance $d$ from the coupling prism, $n_1$ (Fig. 5.1), is proposed. In such system, in contrary to previously proposed ATR, there available a regime when incident wave experiences total internal reflection (TIR) at the $n_2|n_3$ interface where graphene layer is situated. By employing materials with low optical contrast between $n_2$ and $n_3$, TIR regime with close to 90° angle of incidence for the excitation wave is possible to achieve, which is strongly favourable for adherence of phase matching and efficient TE mode excitation.

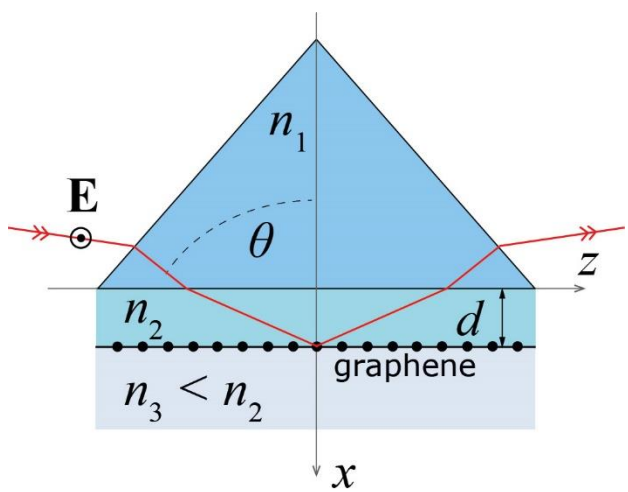


**Figure 5.1.** Modified Otto excitation scheme with asymmetrical indices $n_2 > n_3$.

## 5.2 Experimental approach

At first, we consider TE mode behaviour near the cutoff distance $d_{cut}$, as described in Chapter 4. The cutoff distance $d = d_{cut}$ denotes the condition of complete TE mode delocalisation in Otto configuration, i.e. when for $n_2 = n_3$ and $d < d_{cut}$, the existence of localised at graphene TE mode is prohibited. When $d > d_{cut}$, the solution of TE mode exists, but starts to be delocalised in the direction of $n_3$ as $d$ approaches to $d_{cut}$. However, increasing of $n_2 > n_3$ makes delocalisation to occur in the opposite direction (see section 4.1.3). Through the balancing of this index asymmetry by a proper selection of distance $d$, a condition of propagating TE mode existence can be preserved.

As predicted in section 4.2, in a stack of randomly oriented graphene layers (i.e. in a multilayer graphene with rotational faults [68]), an effective optical conductivity of the stack linearly increases proportional to the number of layers $N$ [64], [68]–[70]: $\sigma^{eff} = N\sigma$. Considering this, employed is the five-layer graphene stack to derive significantly more effective coupling to incident wave.

Graphene electrodes in the samples are deposited on a polyvinylidene fluoride resin which serves as a substrate (PVDF; $n_3^{(1.55\mu m)} \approx 1.4045$), with applied silver electrodes deposited by hand using the conductive silver paint (Fig. 5.2). Then, graphene can be electrostatically doped by an applied bias voltage via top-gated configuration [71] (essential for high doping values) with an ionic liquid of proper refractive index [72] ($n_2^{(1.55\mu m)} \approx 1.4070$), such that desired index asymmetry condition $n_2 > n_3$ is satisfied. Employing of an ionic liquid instead of an ion gel (see for example, [73]) allows scanning over the distance $d$ between graphene and the coupling prism (BK7; $n_1^{(1.55\mu m)} \approx 1.5006$), approaching desired values of $d \sim \lambda_0$, in order to obtain precise phase matching (discussed in sections 4.1.2 and 4.1.3).

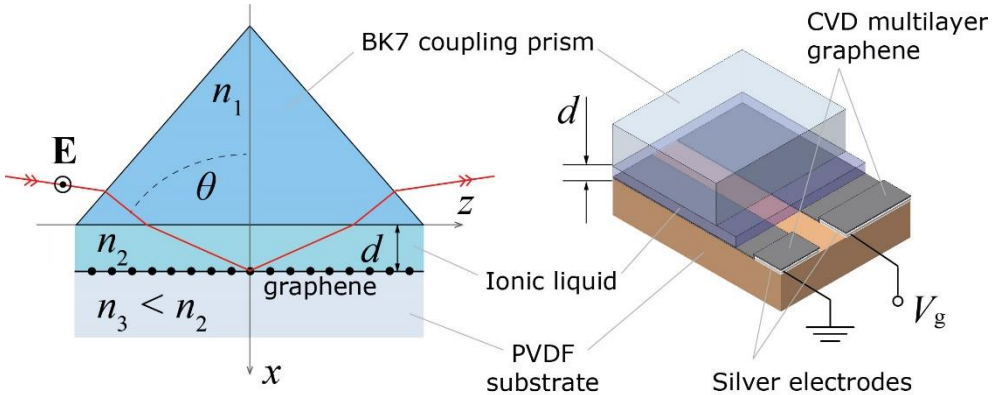


**Figure 5.2.** Modified Otto excitation scheme and multilayer graphene samples.

The PVDF film of thickness 0.254 mm was purchased from CS Hyde; silver electrodes were deposited manually using Pelco® colloidal silver liquid manufactured by Ted Pella, Inc. (product No. 16031), and cured at room temperature during 24 hours. 12.5×12.5 $mm^2$ area five layer graphene was manufactured by chemical vapour deposition [74] (CVD) and deposited layer by layer in acetone, and was purchased from Graphene Square, Inc. The ionic liquid 1-ethyl-3-methylimidazolium bis(trifluoromethylsulfonyl)imide was used as obtained from manufacturer, purchased from Sigma-Aldrich.

To measure angular reflectance, we employ a setup schematically shown in Fig. 5.3, where linear shift of a scanning flat mirror is translated into a high-resolution angular scan by concave spherical mirror of large radius. Gold-covered spherical mirror of 1250 mm radius was mounted at fixed stage while angular scan was conducted by a flat mirror on a moving linear stage (Fig. 5.3), providing, together with collimated laser beam with diameter of 1 mm, an effective angular resolution of 0.05 deg, while mechanically limited angular resolution allowed by the setup is $3\times10^{-5}$ deg.

Excitation wave's polarization is controlled by a fibre polarization controller (FPC), and collimated beam diameter is 1 mm, providing an effective angular resolution of the system 0.05 deg. Laser source used is the tunable diode laser at 1.55 μm wavelength and 1 mW power output. Infrared reflectance measurements are performed with power meter head with removed cover glass to avoid interference effects under varying angle. All measurements are performed under normal ambient conditions at 300 K temperature.

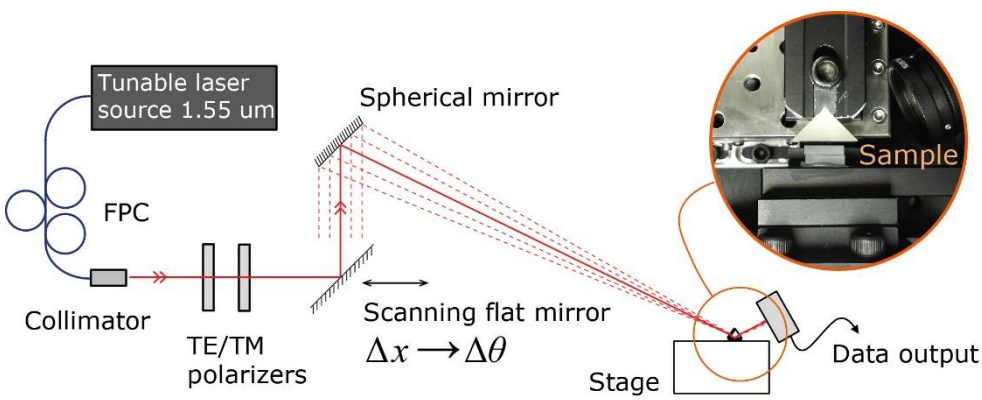


**Figure 5.3.** Optomechanical setup designed to measure angular reflectance with required precision.

## 5.3 Measurement results

Experimentally measured angular reflectance for two different samples is shown in Fig. 5.4 and is obtained for undoped (dashed lines) and doped (solid lines) 5-layer graphene stack under the bias voltage $V_g = 3.8$V and 4.5V respectively, for TM (black) and TE (blue) polarized incident wave ($\lambda_0 = 1.55$ μm; $T = 300$ K). While the TM curves show no response to doping, TE reflectance of doped graphene exhibits a distinct dip in the vicinity of the critical angle $\theta_c$ and can be observed for both samples, indicating an excitation of a guided TE mode in the structure. It is important to note that in the absence of the graphene, reflectance profile indicates lack of any specific TE mode in the structure under applied experimental conditions, which was confirmed by the control experiment (Fig. 5.5). Perfect agreement with analytical TE/TM curves is observed – see inset in Fig. 5.5.

To confirm the experimental data, and to get an insight into the mode excitation dynamics, a numerical model of employed excitation scheme is used, considering angular resolution $\Delta\theta \approx 0.05$ deg as provided by the experimental setup. Model parameters fitting is conducted based on both TE and TM reflectance responses, providing roughly estimated tolerances of $\pm 0.1\lambda_0$ for the distance $d$, and ±5meV for the Fermi level $E_F$ (Fig. 5.6). In the model, sheet conductivity of single graphene layer is calculated using random phase approximation (RPA) in the local limit (see chapter 2), with assumed charge carriers' mobility $\mu = 1 \times 10^4$ cm$^2$(Vs)$^{-1}$. In accordance with the RPA, fitted sheet conductivity is taken as $\sigma_1 = \sigma_u - i0.01\sigma_u$ for the undoped, and $\sigma_2 = 0.3\sigma_u - i0.4\sigma_u$ (model case 1) and $\sigma_2 = 0.7\sigma_u - i0.47\sigma_u$ (model case 2) for the doped graphene, corresponding to doping levels of $E_F \approx 0.42$ eV and 0.38 eV respectively; $\sigma_u = e^2/4\hbar$ is the universal conductivity of graphene [32]. For the 5-layer stack in the experiment, its effective conductivity is $\sigma^{eff}_{1,2} = 5 \times \sigma_{1,2}$.

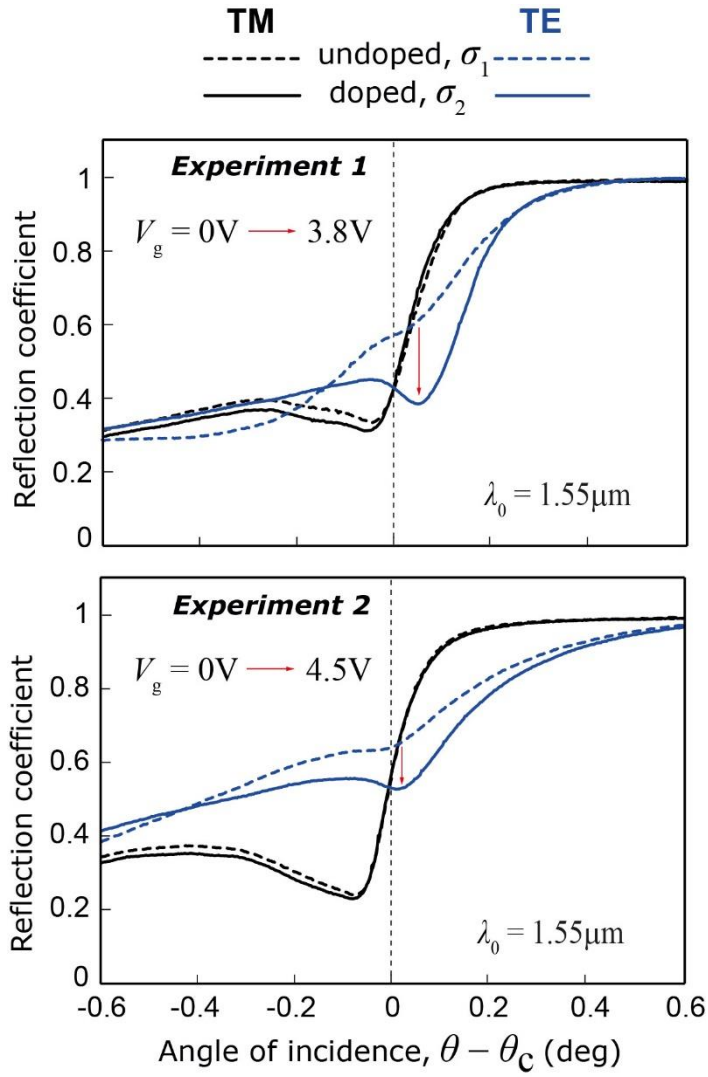


**Figure 5.4.** Experimentally measured angular reflectance of samples with 5-layer graphene for TE (blue) and TM (black) incident waves, for undoped (dashed) and doped (solid) graphene under the bias voltage $V_g$ = 3.8V (sample 1; top) and $V_g$ = 4.5V (sample 2; bottom).

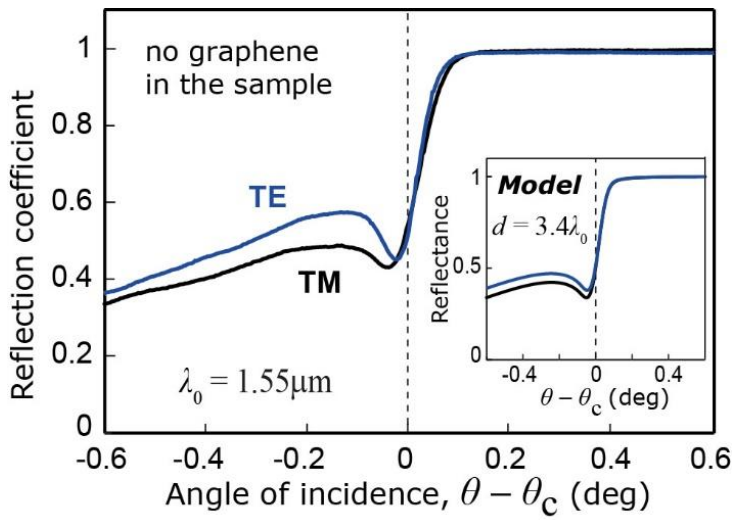


**Figure 5.5.** Angular reflectance measured in the absence of graphene layer under experimental conditions same as for sample 1 in Fig. 5.4. Inset – model numerical reflectance with no graphene for $d = 3.4\lambda_0$.

Numerical reflectance obtained for the values of $\sigma^{eff}_{1,2}$, and $d = 3.4\lambda_0$ (model case 1) and $d = 2.5\lambda_0$ (model case 2) for both samples is shown in Fig. 5.7, demonstrating the electrodynamic response in excellent agreement to that experimentally observed (Fig. 5.5). Considering a uniqueness of reflectance profile for given values of $d$ and $\sigma$, along with the estimated tolerances, it can be noted that fitted model parameters are very close to actual experimental conditions, thus confirming the doping of multilayer graphene coming up to negative values of $\sigma''$. Together with the reflectance minima located beyond the critical angle in both experimental and model studies, this indicates an excitation of TE mode in multilayer graphene.

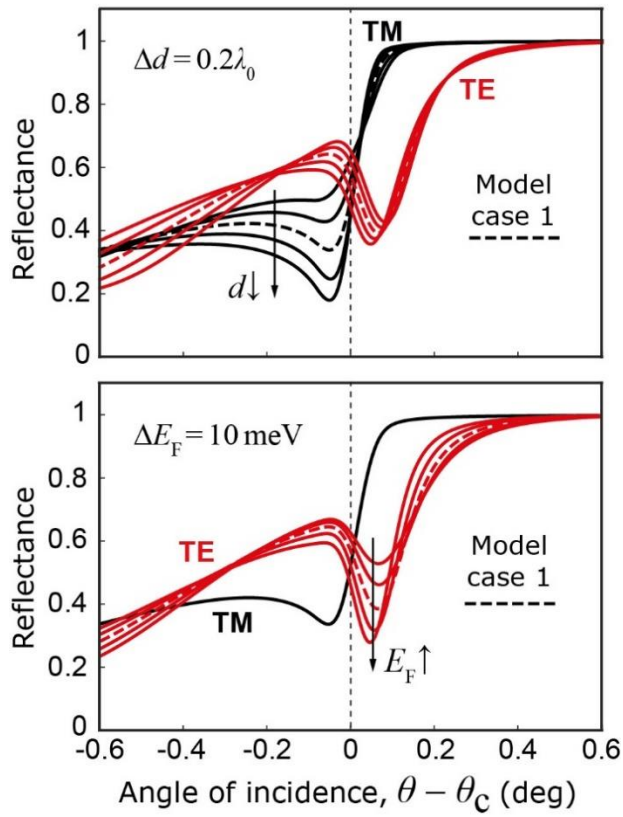


**Figure 5.6.** Numerically demonstrated dependence of the reflectance profile on distance *d* (top) and graphene doping level (Fermi energy; bottom) for the basis of model parameters of case 1(dashed); arrows indicate change in reflectance profile according to denoted step change in parameters.

It must be noted that an approximately 1 nm thick Debye layer of ions at the graphene/ionic liquid interface [71] does not provide detectable interference with the measurements. Considering that the angular reflectance behavior for both TM and TE polarized light perfectly follows theoretical prediction of a model where TE mode is excited in a doped graphene stack (Fig. 3a-d), it is clear that the observed change of the TE reflectance under applied gate voltage is dominantly determined by a change of the optical conductivity in graphene.

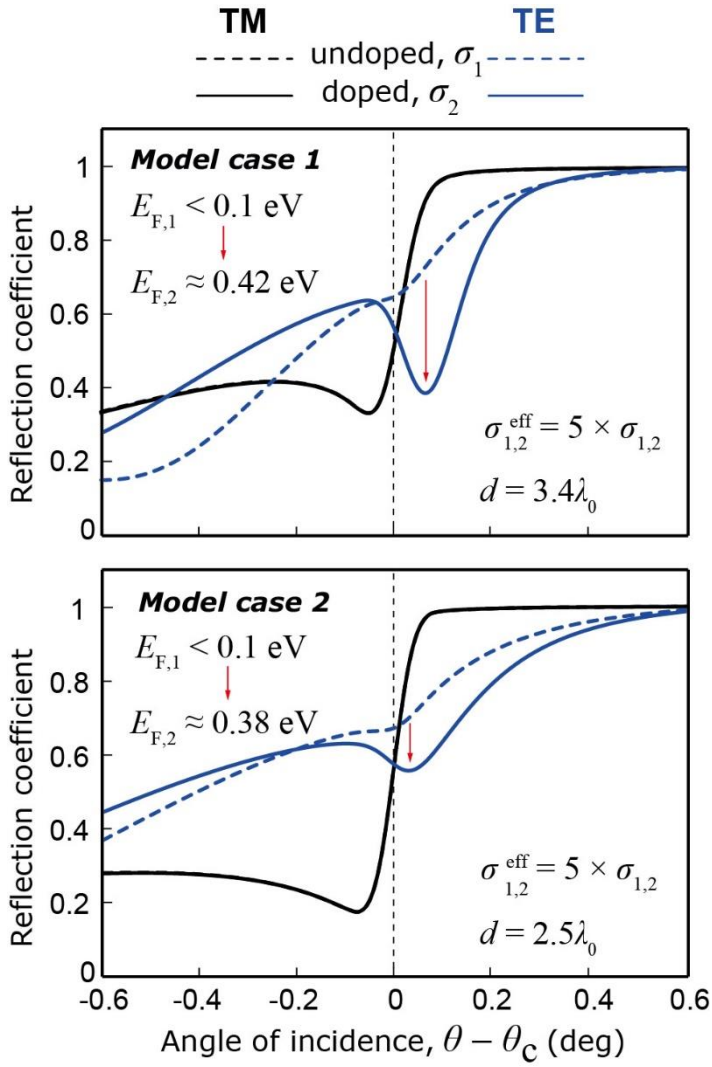


**Figure 5.7.** (Top) Numerical reflectance data replicating experimental conditions for sample 1 (as in Fig. 5.5 (top); model case 1), with fitting parameters $d = 3.4\lambda_0$, $n_2 = 1.407$, $n_2 - n_3 = 0.0025$, at indicated values of graphene conductivity. (Bottom) Numerical reflectance data replicating experimental conditions for sample 2 (as in Fig. 5.5 (bottom); model case 2), with similar fitting parameters for $n_{2,3}$ and $d = 2.5\lambda_0$, at indicated values of graphene conductivity.

## 5.4 Discussion on experimental results

Further numerical investigation with an eigenmode solver (by solving the determined system of equations (4.1) in the absence of the incident wave $A_1 = 0$) reveals a consistent presence of the TE eigenmode supported irrespectively of the structure variations, proving its existence solely due to the presence of multilayer graphene stack. Figure 5.8 demonstrate an electric field intensity $|E|^2$ profile of this mode (top and bottom sets corresponding to different doping levels according to cases "1" and "2" respectively). Leftmost profiles correspond to reconstructed experimental conditions of cases "1" and "2" (Fig. 5.7), and demonstrate the profile of the TE mode responsible for the experimentally observed reflectance dip at doped multilayer graphene (Fig. 5.5). This doped graphene mode, although perturbed by the leaky term, is confined to graphene plane in contrary to the waveguide mode supported with presence of undoped lossy graphene in an asymmetric index (the midst in Fig. 5.8). An unperturbed TE graphene mode is also supported by the structure with considered parameters, but only when $n_2 = n_3$, thus being tricky to be excited; its profile is the rightmost in Fig. 5.8.

Graphene sheets in a multilayer stack are separated by approximately 0.3 nm distance [64]. Considering huge (about three orders of magnitude) difference between the size of the TE mode (Fig. 5.8) and the actual thickness of the 5-layer graphene stack, experimentally detected TE mode is supported by a thin (i.e. with effectively zero thickness) layer of graphene with effective conductivity $\sigma^{\text{eff}}$ proportional to the number of layers (see section 4.1.3 and [64], [68]–[70]). At the same time, the physical nature of the mode is that of graphene TE mode.

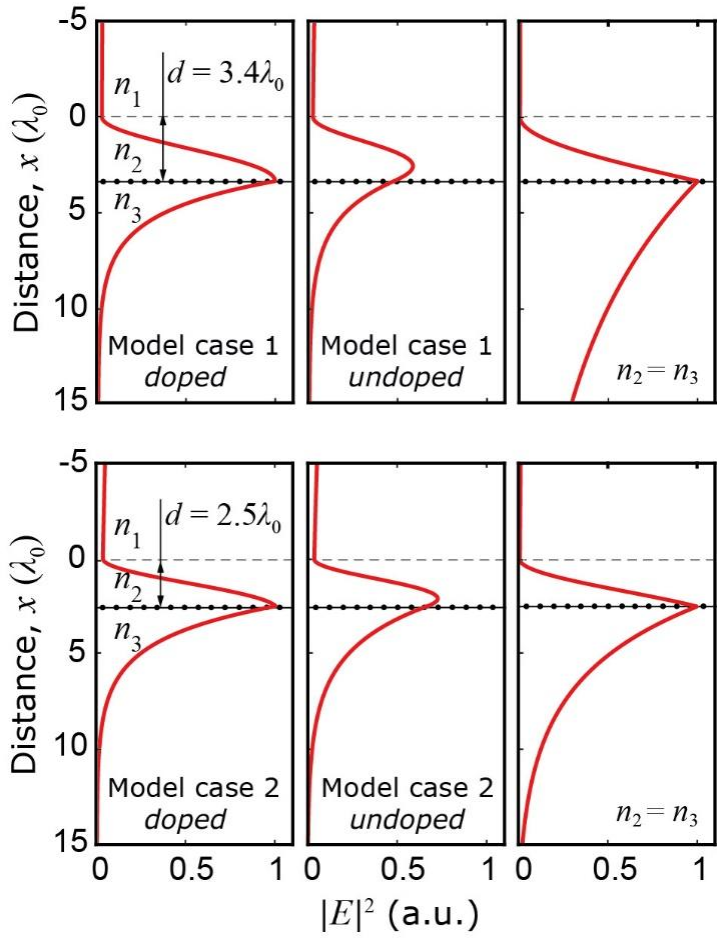


**Figure 5.8.** Obtained with a solver, electrical field intensity $|E|^2$ profiles of TE eigenmodes in considered structure with parameters of case 1 (top) and 2 (bottom). Left: TE eigenmode of doped graphene responsible for the experimentally observed TE reflectance dip. Middle: same as on the left, but for undoped graphene – a waveguide mode, with amplitude scaled according to theoretical coupling efficiency 59% (74%) for case 1 (2) of that for doped graphene mode. Right: an unperturbed TE mode supported by doped graphene in the considered structure under assumption of $n_2 = n_3$.

Figure 5.9 displays the effect of doping on losses associated with the TE mode as a function of distance *d*. Due to reduction of internal losses (blue) in doped graphene (solid lines) at shorter *d*, their magnitude becomes comparable with that of radiative losses (green), providing significantly enhanced coupling to incident light [29], [59], and producing experimentally observed distinct reflectance dip. As one can note, cumulative losses of the excited mode are still very low, though higher than in case of $n_2 = n_3$ (see inset in Fig. 5.11), giving its propagation length $L = \lambda_P/(2\pi q'')$ = ~1000 of plasmonic wavelengths, unimaginable for TM plasmons.

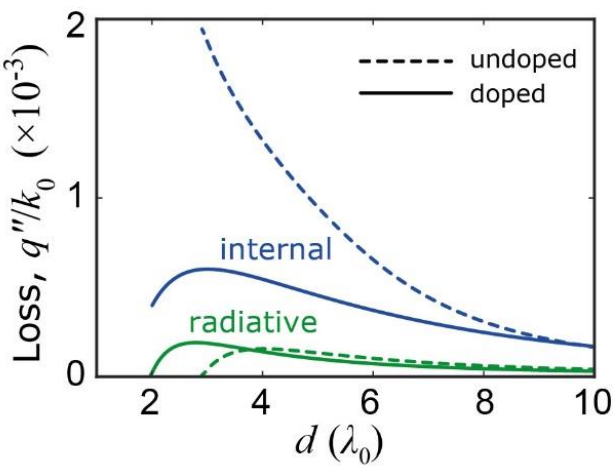


**Figure 5.9.** Internal (blue) and radiative (green) losses of the TE eigenmode for the undoped (dashed) and doped (solid) graphene, for the set of parameters of model case 1.

TE mode's electric field spatial distribution for the model case 2 is demonstrated at Fig. 5.10, showing significant asymmetry along the *x*-*z* axes, revealing mode expansion by several $\lambda_0$ into the bulk on both sides. Obtained with the solver dispersion of the TE mode for model case 1 (black), case 2 (pink), and

case 1 with $n_2 = n_3$ (dashed) is demonstrated in Fig. 5.11, with losses shown in the inset. Observed in Fig. 5.11 for model cases 1 and 2, the dispersion cutoff is associated with complete delocalization (leaking) of modes in the direction of $n_3$, following prediction for the symmetrical ($n_2 = n_3$) configuration (see section 4.1.3). Modes' delocalization is demonstrated in Fig. 5.12 where field's intensity and spatial distribution are shown for distances $d \approx d_{cut}$ for considered model cases. It is also clearly demonstrated (Fig. 5.11) that cutoff distance in case when $n_2 = n_3$ is significantly larger comparing to that in employed experimental configuration, preventing efficient coupling to the TE mode.

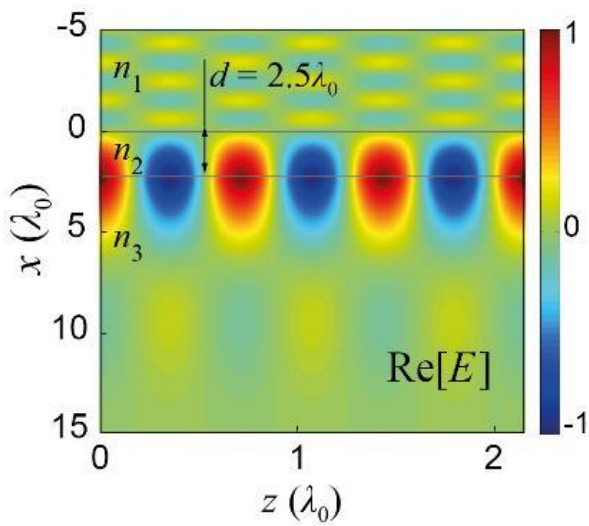


**Figure 5.10.** Electric field spatial distribution of the TE eigenmode for the set of parameters of model case 2.

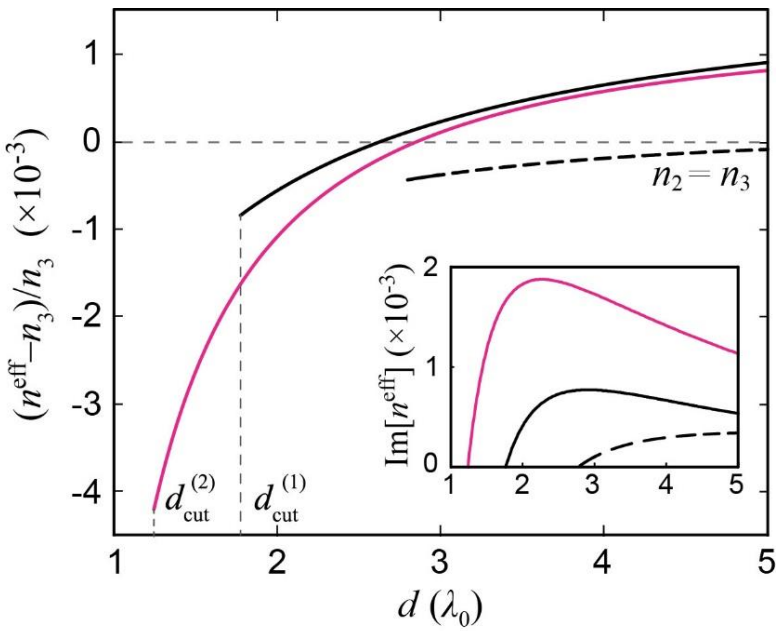


**Figure 5.11.** Dispersion of the TE eigenmode for the set of parameters of model case 1 (black), case 2 (pink), and case 1 with $n_2 = n_3$ (dashed) as a function of distance $d$. Inset: cumulative losses of the TE eigenmode for all cases.

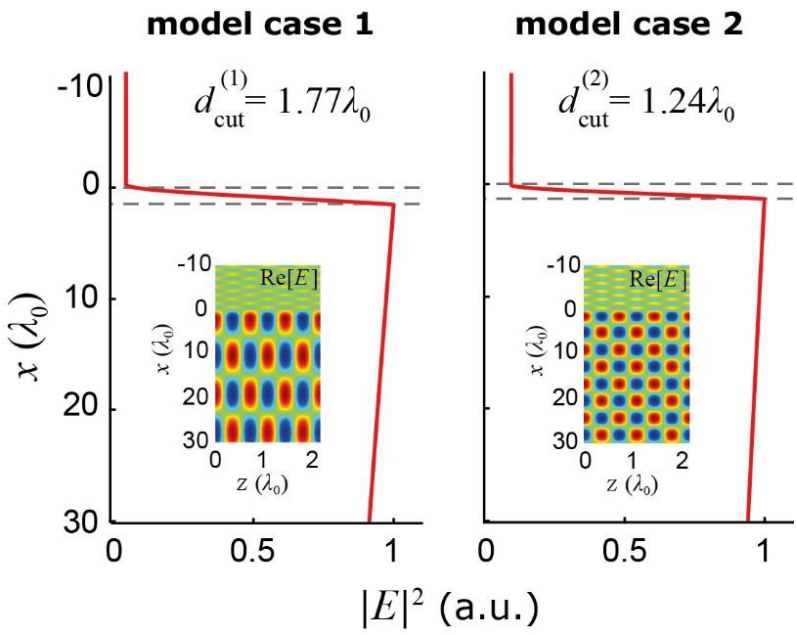


**Figure 5.12.** TE eigenmode's electrical field intensity profile $|E|^2$ shown at the indicated cutoff distances $d = d_{cut}$, for model cases 1 and 2. Insets: electrical field spatial distribution demonstrated for each cutoff case.

## 5.5 Remarks on multilayer graphene doping

The top-gated configuration for electrostatic graphene doping via the ionic liquid [71], [75], using two graphene stripes as electrodes, is used in the experimental setup. When bias voltage is applied, a Debye layer in the ionic liquid of thickness $d_{TG}$ ~1 nm is formed around the electrodes [75], acting as a parallel plate capacitor. Graphene electrode thus being one of the capacitor plates, so its charge carriers' concentration $n$ can be related to the applied bias voltage $V_g$ as follows [71]:

$$V_{TG} = \frac{\hbar |\upsilon_F| \sqrt{\pi n}}{e} + \frac{d_{TG} n e}{\varepsilon \varepsilon_0} \tag{5.1}$$

where $\varepsilon$ is the dielectric constant of the ionic liquid, $n$ is the carriers' concentration in graphene electrode. The Debye layer thickness in an electrolyte can be obtained as [76]:

$$d_{TG} = \sqrt{\frac{\varepsilon \varepsilon_0 RT}{2F^2 c_0}} \tag{5.2}$$

where $R$ is the molar constant, $F = eN_A$ is the Faraday constant, and $c_0 = 3.9$ mol/l is the molar concentration of the 1-ethyl-3-methylimidazolium bis(trifluoromethylsulfonyl)imide ionic liquid [77], [78]. Obtained value of the Debye layer $d_{TG} \approx 0.8$ nm is relatively small due to high electrolyte concentration of the ionic liquid, and comparable with thickness of several graphene layers, thus making difficult to predict actual charge distribution in real system of several layers where screening effects will occur. Therefore, as a first-order approximation, we assume that charge carriers' concentrations (Fermi energy) in all layers are equal, and the total effective carriers' concentration of the whole stack can be represented as $n = X \times n_{gr}$, where $n_{gr}$ is concentration of a single layer, and $X$ is some real number.

Considering the stack of graphene sheets as a single layer with Fermi energy as a function of effective carriers' concentration $E_F = \hbar|\upsilon_F|\sqrt{\pi n}$, following equations (5.1)-(5.2), and considering RPA conductivity at room temperature [equation (2.1)], one can obtain values of Fermi level and RPA sheet conductivity of a single graphene layer as a function of applied bias voltage, which is demonstrated in Fig. 5.13.

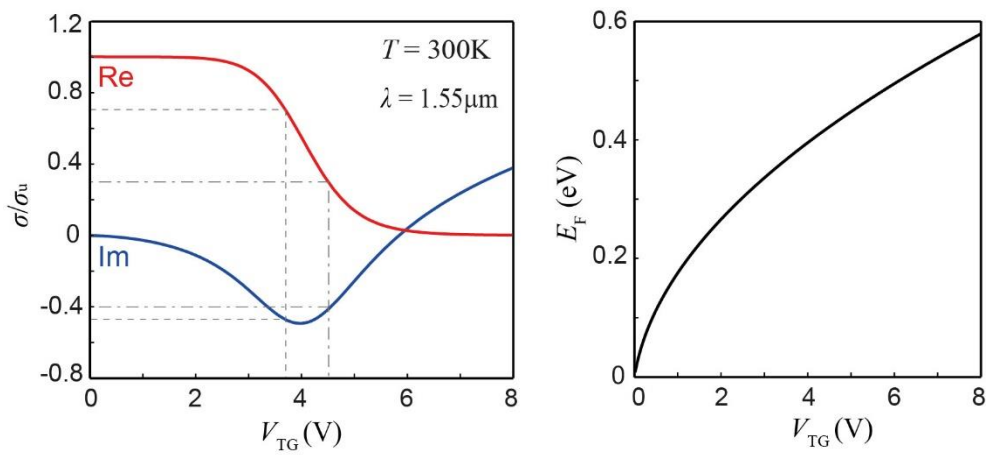


**Figure 5.13.** (Left) RPA sheet conductivity of single layer graphene as a function of bias voltage. Carriers' concentration of each single layer is assumed uniform through the five layer stack, and its value $n_{gr} = n/3$. Dot-dashed lines show real and imaginary parts of conductivity according to the experiment 1 reconstruction (model case 1; $V_{TG}$ = 3.8 V, $\sigma_2 = 0.3\sigma_u - i0.4\sigma_u$), and dashed lines show that for the experiment 2 reconstruction (model case 2; $V_{TG}$ = 4.5 V, $\sigma_2 = 0.7\sigma_u - i0.47\sigma_u$). (Right) Fermi energy of a single graphene layer as a function of bias voltage.

Interestingly, the assumption of $X$ = 3 gives the exact match between experimentally observed bias voltages and conductivity values used for experimental results reconstruction by an electrodynamic model of the structure. In other words, assumed conductivity of each graphene layer in a five layer graphene stack can be

taken as $n_{gr} = n/3$, where $n$ is an effective concentration in multilayer graphene treated as a single layer. Then, setting equal the effective concentration in the electrodynamic model (EM) and the top gated (TG) doping model, for a single layer in the stack of five we can speculate that $n_{gr}^{EM} = 3/5 \times n_{gr}^{TG}$. This may indicate that actual doping levels in conducted experiments are ~40% lower than that theoretically obtained from equations (5.1) and (5.2).

Demonstrated successful example of multilayer graphene doping requires more close study of the subject since multilayer graphene systems generally are able to provide significantly stronger electrodynamic response comparing with that built on a single graphene layer.

## 5.6 Conclusion

To summarize, the exotic TE mode in graphene can be successfully excited in multilayer graphene at room temperature. Its first experimental observation is achieved employing 5-layer doped graphene in modified Otto configuration with very precise phase matching capability. Besides, successful doping of multilayer graphene up to significant values of $E_F$ using an ionic liquid is also demonstrated, confirming predicted earlier increase of effective graphene conductivity. It is also suggested that optical sensing of the TE excitation in doped graphene can be used as a handy technique for characterisation of doping in multilayer graphene, and attract more attention to this unique phenomenon in the essential spectral transition domain.

## Chapter 6

# Conclusion

In this Dissertation, two major topics regarding the graphene's plasmonic response have been discussed. Owing to its unusual and tunable electrodynamic response, graphene provides a unique platform for low dimensional plasmonics at stripes, edges, and interfaces, at the same time supporting the transverse electric mode which by itself is an extraordinary phenomenon unavailable in other plasmonic materials. Interestingly, the transition spectral region of graphene's electrodynamic response (i.e. when response type changes from metallic- to dielectric-like) is associated to the both considered cases: 1D plasmonic excitation of the metal-dielectric interface and TE mode, each of which comprises an extreme case of plasmonic phenomena – that with exceptionally strong and weak field localization respectively.

First, is was demonstrated that induced in graphene by non-uniform doping, the 1D metal-dielectric interface supports propagating 1D plasmonic mode (1DSPP) exhibiting a tremendous spatial field localization – up to one million times compared to a wave in a free space. This regime become available due to the dielectric-like properties of graphene at one side of the interface, being tuned into the transition region by doping. This tuning of graphene's conductivity further allows controlling

over the 1DSPP effective index continuously from that of the bare edge up to cutoff regime with extremely high effective index values. Series of FEM numerical simulations completely confirmed validity of derived dispersion relation for the 1DSPP plasmonic mode, and demonstrated the predicted tunability of its effective index.

Second, a rigorous study of predicted earlier TE mode in graphene has revealed its accessibility to direct optical excitation and detection via the Otto configuration. The experimental detection of TE mode has not been reported yet due to its extremely weak localization on sensitivity to excitation environment. To overcome experimental issues, certain necessary modifications to the excitation scheme have been suggested to derive extremely precise phase matching and strong coupling to the excitation wave. Namely, artificially introduced index asymmetry, doped five-layer graphene stack, and tunable Otto configuration have allowed for the first ever excitation and detection of the TE mode in graphene.

Overall, in a single framework of this Dissertation, two fundamental aspects of graphene's electrodynamic response in its spectral transition region have been studied, for the first time demonstrating an existence of extreme cases of high-index 1DSPP plasmonic mode (theoretically and numerically), and low-index unique TE mode (experimentally) in graphene.

# Publications by the Author

## Journal articles

*equal contribution; **corresponding author

1) (submitted) Sergey Menabde, Hyunwoo Park, and Namkyoo Park, "Localized defect-assisted acoustic phonon scattering of hot carriers in graphene," (2017).
2) Viacheslav Shaidiuk, and Sergey Menabde,** "Modal evolution in asymmetric three- and four-layer plasmonic waveguides," Optics Express **24**, pp. 16595-16608 (2016).
3) Viacheslav Shaidiuk,* Sergey Menabde,* and Namkyoo Park, "Effect of structural asymmetry on three layer plasmonic waveguide properties," J. Opt. Soc. Am. B **33**, pp. 963-970 (2016).
4) Sergey Menabde, Daniel R. Mason, Evgeny Kornev, Changhee Lee, and Namkyoo Park, "Direct Optical Probing of Transverse Electric Mode in Graphene," Scientific Reports **6**, 21523 (2016).
5) Daniel R. Mason,* Sergey Menabde,* Sunkyu Yu, and Namkyoo Park, "Plasmonic Excitations of 1D Metal-Dielectric Interfaces in 2D Systems: 1D Surface Plasmon Polaritons," Scientific Reports **4**, 4536 (2014).
6) Daniel R. Mason,* Sergey Menabde,* and Namkyoo Park, "Unusual Otto excitation dynamics and enhanced coupling of light to TE plasmons in graphene," Optics Express **22**, pp. 847-858 (2014).
7) M. Sathish Kumar, Sergey Menabde, Sunkyu Yu, and Namkyoo Park, "Directional emission from photonic crystal waveguide terminations using particle swarm optimization," J. Opt. Soc. Am. B **27**, pp. 343-349 (2010).

# Patents

1) US patent application: US20130137930 A1 / EU patent application: EP2596740 A1 / China patent application: CN103135211 A1 / Title: “Objective lens for endoscopic device, actuator for focusing, and endoscopic system” / Publication date: May 30, 2013 / Inventors: Sergey Menabde, Jongchul Choi, Haein Chung / Assignee: Samsung Electronics.
2) Korean Patent Application: 1020100045464 / Title: “두 개의 카메라 입사 동공 간의 거리를 조절할 수 있는 3D 카메라 (3-Dimension Camera)” / Publication date: 2011.11.22 / Inventor: Sergey Menabde / Assignee: Samsung Electronics.

# International conferences

1) Sergey Menabde, Daniel R. Mason, Evgeny Kornev, Changhee Lee and Namkyoo Park, “Detection of exotic transverse electric mode in graphene,” Near Field Optics 14 (NFO’14), Hamamatsu, Japan, September 2016.
2) Sergey Menabde, Viacheslav Shaidiuk, and Namkyoo Park, “Asymmetric plasmonic waveguides as platform for coupling between surface plasmons and propagating waves,” Near Field Optics 14 (NFO’14), Hamamatsu, Japan, September 2016.
3) Sergey Menabde and Namkyoo Park, “Detection of Transverse Plasmons in Multilayer Graphene,” Metamaterial’2015 Congress, University of Oxford, UK, September 2015.
4) Sergey Menabde, Daniel Mason, and Namkyoo Park, “Enhanced coupling of light to TE plasmons in multilayer graphene,” Near Field Optics 13 (NFO’13), Salt Lake City, USA, September 2014.

5) Daniel Mason, Sergey Menabde, Sunkyu Yu, Seungkyun Park, and Namkyoo Park, "1D plasmons at metal-dielectric interfaces in 2D systems," Near Field Optics 13 (NFO'13), Salt Lake City, USA, September 2014.

6) Sergey Menabde, Sunkyu Yu, Xianji Piao, Daniel R. Mason, and Namkyoo Park, "Low Dimensional Nano-Photonic Systems," OSK Annual Summer Meeting 2014, Cheju, August 2014.

7) Daniel Mason, Sergey Menabde, Sunkyu Yu, and Namkyoo Park, "1-Dimensional Surface Plasmon Polaritons in 2-Dimensional Systems," 3rd Korea-Japan Metamaterials Forum 2013, K1, Seoul, June 2013.

8) Sergey Menabde, Daniel R. Mason, and Namkyoo Park, "Non-Abrupt-Edge Effects on Graphene Edge Plasmon Dispersion," Conference on Surface Plasmon-Polaritons (SPP6), Ottawa, Canada, 25-31 May 2013.

9) Sergey Menabde, "Small-size Zoom Lens Design," Optics-Photonics Design & Fabrication ODF'06, Nara, Japan, December 2006.

10) Sergey Menabde, "Automated zoom lens design," Frontiers in Optics 2006, Rochester, USA, October 2006.

11) Sergey Menabde, and Vitaly Klimov, "Automated zoom lens design and second-order derivative optimization methods," Optics & Photonics 2006, San-Diego, USA, August 2006.

# Bibliography


[1] A. Geim, “Random Walk To Graphene,” *Int. J. Mod. Phys. B*, vol. 25, no. 30, pp. 4055–4080, 2011.

[2] A. K. Geim, “Graphene: Status and Prospects,” *Science*, vol. 324, no. 5934, pp. 1530–1534, 2009.

[3] F. H. L. Koppens, D. E. Chang, and F. J. G. De Abajo, “Graphene plasmonics: A platform for strong light-matter interactions,” *Nano Lett.*, vol. 11, no. 8, pp. 3370–3377, 2011.

[4] Q. Bao and K. P. Loh, “Graphene photonics, plasmonics, and broadband optoelectronic devices,” *ACS Nano*, vol. 6, no. 5, pp. 3677–3694, 2012.

[5] A. N. Grigorenko, M. Polini, and K. S. Novoselov, “Graphene plasmonics,” *Nat. Photonics*, vol. 6, no. 11, pp. 749–758, 2012.

[6] F. J. G. de Abajo, “Graphene Plasmonics: Challenges and Opportunities,” *ACS Photonics*, vol. 24, no. 3, pp. 25–29, 2014.

[7] S. A. Mikhailov and K. Ziegler, “New Electromagnetic Mode in Graphene,” *Phys. Rev. Lett.*, vol. 99, no. 1, p. 16803, 2007.

[8] D. K. Gramotnev and S. I. Bozhevolnyi, “Plasmonics beyond the diffraction limit,” *Nat. Photonics*, vol. 4, no. 2, pp. 83–91, 2010.

[9] X. Gan, K. F. Mak, Y. Gao, Y. You, F. Hatami, J. Hone, T. F. Heinz, and D. Englund, “Strong enhancement of light-matter interaction in graphene coupled to a photonic crystal nanocavity,” *Nano Lett.*, vol. 12, no. 11, pp. 5626–5631, 2012.

[10] M. Jablan, H. Buljan, and M. Soljačić, “Plasmonics in graphene at infrared frequencies,” *Phys. Rev. B*, vol. 80, no. 24, p. 245435, 2009.

[11] E. H. Hwang and S. Das Sarma, “Dielectric function, screening, and plasmons in two-dimensional graphene,” *Phys. Rev. B*, vol. 75, no. 20, 2007.

[12] A. Vakil and N. Engheta, “Transformation Optics Using Graphene,” *Science*, vol. 332, no. 6035, pp. 1291–1294, 2011.

[13] A. Y. Nikitin, F. Guinea, F. J. García-Vidal, and L. Martín-Moreno, “Edge and waveguide terahertz surface plasmon modes in graphene microribbons,” *Phys. Rev. B*, vol. 84, no. 16, p. 161407, 2011.

[14] J. Christensen, A. Manjavacas, S. Thongrattanasiri, F. H. L. Koppens, and F. J. García De Abajo, “Graphene plasmon waveguiding and hybridization in individual and paired nanoribbons,” *ACS Nano*, vol. 6, no. 1, pp. 431–440, 2012.

[15] A. Y. Nikitin, F. Guinea, F. J. Garcia-Vidal, and L. Martin-Moreno, “Surface plasmon enhanced absorption and suppressed transmission in periodic arrays of graphene ribbons,” *Phys. Rev. B*, vol. 85, no. 8, pp. 1–4, 2012.

[16] R. Alaee, M. Farhat, C. Rockstuhl, and F. Lederer, “A perfect absorber made of a graphene micro-ribbon metamaterial,” *Opt. Express*, vol. 20, no. 27, p. 28017, 2012.

[17] Z. Fei, M. D. Goldflam, J. S. Wu, S. Dai, M. Wagner, A. S. McLeod, M. K. Liu, K. W. Post, S. Zhu, G. C. A. M. Janssen, M. M. Fogler, and D. N. Basov, “Edge and Surface Plasmons in Graphene Nanoribbons,” *Nano Lett.*, vol. 15, no. 12, pp. 8271–8276, 2015.

[18] E. G. Mishchenko, A. V. Shytov, and P. G. Silvestrov, “Guided Plasmons in Graphene p-n Junctions,” *Phys. Rev. Lett.*, vol. 104, no. 15, p. 156806, 2010.

[19] N. M. Hassan, V. V. Mkhitaryan, and E. G. Mishchenko, “One-dimensional plasmons confined in bilayer graphene p-n junctions,” *Phys. Rev. B - Condens. Matter Mater. Phys.*, vol. 85, no. 12, 2012.

[20] S. Thongrattanasiri, F. H. L. Koppens, and F. J. García de Abajo, “Complete Optical Absorption in Periodically Patterned Graphene,” *Phys. Rev. Lett.*, vol. 108, no. 4, p. 47401, 2012.

[21] Z. Fang, S. Thongrattanasiri, A. Schlather, Z. Liu, L. Ma, Y. Wang, P. M. Ajayan, P. Nordlander, N. J. Halas, and F. J. García De Abajo, “Gated tunability and hybridization of localized plasmons in nanostructured

graphene," *ACS Nano*, vol. 7, no. 3, pp. 2388–2395, 2013.

[22] S. Thongrattanasiri and F. J. Garcia De Abajo, "Optical field enhancement by strong plasmon interaction in graphene nanostructures," *Phys. Rev. Lett.*, vol. 110, no. 18, 2013.

[23] Z. Fei, A. S. Rodin, G. O. Andreev, W. Bao, A. S. McLeod, M. Wagner, L. M. Zhang, Z. Zhao, M. Thiemens, G. Dominguez, M. M. Fogler, A. H. C. Neto, C. N. Lau, F. Keilmann, and D. N. Basov, "Gate-tuning of graphene plasmons revealed by infrared nano-imaging," *Nature*, pp. 3–6, 2012.

[24] J. Chen, M. Badioli, P. Alonso-González, S. Thongrattanasiri, F. Huth, J. Osmond, M. Spasenović, A. Centeno, A. Pesquera, P. Godignon, A. Zurutuza Elorza, N. Camara, F. J. G. de Abajo, R. Hillenbrand, and F. H. L. Koppens, "Optical nano-imaging of gate-tunable graphene plasmons," *Nature*, pp. 1–5, 2012.

[25] V. Thareja, J.-H. Kang, H. Yuan, K. M. Milaninia, H. Y. Hwang, Y. Cui, P. G. Kik, and M. L. Brongersma, "Electrically Tunable Coherent Optical Absorption in Graphene with Ion Gel," *Nano Lett.*, vol. 15, no. 3, pp. 1570–1576, 2015.

[26] H. Yan, X. Li, B. Chandra, G. Tulevski, Y. Wu, M. Freitag, W. Zhu, P. Avouris, and F. Xia, "Tunable infrared plasmonic devices using graphene/insulator stacks," *Nat. Nanotechnol.*, vol. 7, no. 5, pp. 330–334, 2012.

[27] B. Shi, W. Cai, X. Zhang, Y. Xiang, Y. Zhan, J. Geng, M. Ren, and J. Xu, "Tunable Band-Stop Filters for Graphene Plasmons Based on Periodically Modulated Graphene," *Sci. Rep.*, vol. 6, no. May, p. 26796, 2016.

[28] M. Jablan, H. Buljan, and M. Soljačić, "Transverse electric plasmons in bilayer graphene.," *Opt. Express*, vol. 19, no. 12, pp. 11236–11241, 2011.

[29] P. Yeh, *Optical Waves in Layered Media*. New Jersey: John Wiley & Sons, Inc., 2005.

[30] O. V Kotov, M. a Kol'chenko, and Y. E. Lozovik, "Ultrahigh refractive index sensitivity of TE-polarized electromagnetic waves in graphene at the interface between two dielectric media.," *Opt. Express*, vol. 21, no. 11, pp.

13533–46, 2013.

[31] F. Wang, Y. Zhang, C. Tian, C. Girit, A. Zettl, M. Crommie, and Y. R. Shen, "Gate-Variable Optical Transitions in Graphene," *Science*, vol. 320, no. 5873, pp. 206–209, 2008.

[32] R. R. Nair, A. N. Grigorenko, P. Blake, K. S. Novoselov, T. J. Booth, N. M. R. Peres, T. Stauber, and A. K. Geim, "Fine structure constant defines visual transparency of graphene.," *Science*, vol. 320, no. 5881, p. 1308, 2008.

[33] J. Kim, H. Son, D. J. Cho, B. S. Geng, W. Regan, S. F. Shi, K. Kim, A. Zettl, Y. R. Shen, and F. Wang, "Electrical control of optical plasmon resonance with graphene," *Nano Lett.*, vol. 12, no. 11, pp. 5598–5602, 2012.

[34] V. W. Brar, M. S. Jang, M. Sherrott, J. J. Lopez, and H. a Atwater, "Highly confined tunable mid-infrared plasmonics in graphene nanoresonators.," *Nano Lett.*, vol. 13, no. 6, pp. 2541–7, 2013.

[35] L. Ju, B. Geng, J. Horng, C. Girit, M. Martin, Z. Hao, H. a. Bechtel, X. Liang, A. Zettl, Y. R. Shen, and F. Wang, "Graphene plasmonics for tunable terahertz metamaterials," *Nat. Nanotechnol.*, vol. 6, no. 10, pp. 630–634, 2011.

[36] B. Wunsch, T. Stauber, F. Sols, and F. Guinea, "Dynamical polarization of graphene at finite doping," *New J. Phys.*, vol. 8, 2006.

[37] L. a. Falkovsky, "Optical properties of graphene," *IOP Sci.*, vol. 12004, p. 5, 2008.

[38] W. Wang, P. Apell, and J. Kinaret, "Edge plasmons in graphene nanostructures," *Phys. Rev. B - Condens. Matter Mater. Phys.*, vol. 84, no. 8, p. 85423, 2011.

[39] X. Xia and J. Quinn, "Multipole edge plasmons of two-dimensional electron-gas systems," *Phys. Rev. B*, vol. 50, no. 11, pp. 8032–8034, 1994.

[40] V. A. Volkov and S. A. Mikhailov, "Edge magnetoplasmons: low frequency weakly damped excitations in inhomogeneus two-dimensional electron systems." 1988.

[41] S. A. Mikhailov and V. A. Volkov, "Inter-edge magnetoplasmons in inhomogeneous two-dimensional electron systems," *J. Phys. Condens.*

*Matter*, vol. 4, no. 31, pp. 6523–6538, 1992.

[42] J. M. Pitarke, V. M. Silkin, E. V Chulkov, and P. M. Echenique, "Theory of surface plasmons and surface-plasmon polaritons," *Rep. Prog. Phys.*, vol. 1, no. 1, p. 54, 2006.

[43] S. J. Goncher, L. Zhao, A. N. Pasupathy, and G. W. Flynn, "Substrate level control of the local doping in graphene," *Nano Lett.*, vol. 13, no. 4, pp. 1386–1392, 2013.

[44] L. Ci, L. Song, C. Jin, D. Jariwala, D. Wu, Y. Li, A. Srivastava, Z. F. Wang, K. Storr, L. Balicas, F. Liu, and P. M. Ajayan, "Atomic layers of hybridized boron nitride and graphene domains.," *Nat. Mater.*, vol. 9, no. 5, pp. 430–435, 2010.

[45] M. P. Levendorf, C.-J. Kim, L. Brown, P. Y. Huang, R. W. Havener, D. a. Muller, and J. Park, "Graphene and boron nitride lateral heterostructures for atomically thin circuitry," *Nature*, vol. 488, no. 7413, pp. 627–632, 2012.

[46] Z. Liu, L. Ma, G. Shi, W. Zhou, Y. Gong, S. Lei, X. Yang, J. Zhang, J. Yu, K. P. Hackenberg, A. Babakhani, J.-C. Idrobo, R. Vajtai, J. Lou, and P. M. Ajayan, "In-plane heterostructures of graphene and hexagonal boron nitride with controlled domain sizes," *Nat. Nanotechnol.*, vol. 8, no. 2, pp. 119–124, 2013.

[47] Y. Gao, Y. Zhang, P. Chen, Y. Li, M. Liu, T. Gao, D. Ma, Y. Chen, Z. Cheng, X. Qiu, W. Duan, and Z. Liu, "Toward single-layer uniform hexagonal boron nitride-graphene patchworks with zigzag linking edges," *Nano Lett.*, vol. 13, no. 7, pp. 3439–3443, 2013.

[48] A. Otto, "Excitation of nonradiative surface plasma waves in silver by the method of frustrated total reflection," *Zeitschrift fur Phys.*, vol. 216, no. 4, pp. 398–410, 1968.

[49] A. Y. Nikitin, P. Alonso-González, and R. Hillenbrand, "Efficient coupling of light to graphene plasmons by compressing surface polaritons with tapered bulk materials.," *Nano Lett.*, vol. 14, no. 5, pp. 2896–901, 2014.

[50] S. J. Tan and D. K. Gramotnev, "Analysis of efficiency and optimization of plasmon energy coupling into nanofocusing metal wedges," *J. Appl. Phys.*,

vol. 107, no. 9, p. 94301, 2010.

[51] D. K. Gramotnev and S. I. Bozhevolnyi, “Nanofocusing of electromagnetic radiation,” *Nat. Photonics*, vol. 8, no. 1, pp. 13–22, 2014.

[52] J. A. Dionne, E. Verhagen, A. Polman, and H. A. Atwater, “Are negative index materials achievable with surface plasmon waveguides? A case study of three plasmonic geometries,” *Opt. Express*, vol. 16, no. 23, pp. 19001–19017, 2008.

[53] T. J. Davis, “Surface plasmon modes in multi-layer thin-films,” *Opt. Commun.*, vol. 282, no. 1, pp. 135–140, 2009.

[54] P. Berini, “Long-range surface plasmon polaritons,” *Adv. Opt. Photonics*, vol. 1, no. 3, p. 484, 2009.

[55] R. Zia, M. D. Selker, and M. L. Brongersma, “Leaky and bound modes of surface plasmon waveguides,” *Phys. Rev. B - Condens. Matter Mater. Phys.*, vol. 71, no. 16, 2005.

[56] E. Verhagen, A. Polman, and L. K. Kuipers, “Nanofocusing in laterally tapered plasmonic waveguides.,” *Opt. Express*, vol. 16, no. 1, pp. 45–57, 2008.

[57] P. B. Johnson and R. W. Christy, “Optical constants of the noble metals,” *Phys. Rev. B*, vol. 6, no. 12, pp. 4370–4379, 1972.

[58] Y. V. Bludov, A. Ferreira, N. M. R. Peres, and M. I. Vasilevskiy, “A Primer on Surface Plasmon-Polaritons in Graphene,” *Int. J. Mod. Phys. B*, vol. 27, no. 10, p. 1341001, 2013.

[59] E. M. Yeatman, “Resolution and sensitivity in surface plasmon microscopy and sensing,” *Biosens. Bioelectron.*, vol. 11, no. 6–7, pp. 635–649, 1996.

[60] M. L. Gorodetsky and V. S. Ilchenko, “Optical microsphere resonators: optimal coupling to high-Q whispering gallery modes,” *J. Opt. Soc. Am. B*, vol. 16, no. 1, p. 147, 1999.

[61] R. Naraoka and K. Kajikawa, “Phase detection of surface plasmon resonance using rotating analyzer method,” *Sensors Actuators B*, vol. 107, no. 2, p. 952, 2005.

[62] J. Homola and M. Piliarik, *Surface plasmon resonance (SPR) sensors*. Berlin: Springer, 2006.

[63] a. Gutiérrez-Rubio, T. Stauber, and F. Guinea, "Transverse current response of graphene at finite temperature: plasmons and absorption," *J. Opt.*, vol. 15, no. 11, p. 114005, 2013.

[64] I. H. Baek, K. J. Ahn, B. J. Kang, S. Bae, B. H. Hong, D.-I. Yeom, K. Lee, Y. U. Jeong, and F. Rotermund, "Terahertz transmission and sheet conductivity of randomly stacked multi-layer graphene," *Appl. Phys. Lett.*, vol. 102, no. 19, p. 191109, 2013.

[65] M. A. K. Othman, C. Guclu, and F. Capolino, "Graphene–dielectric composite metamaterials: evolution from elliptic to hyperbolic wavevector dispersion and the transverse epsilon-near-zero condition," *J. Nanophotonics*, vol. 7, no. 1, p. 73089, 2013.

[66] J. Hass, F. Varchon, J. E. Millán-Otoya, M. Sprinkle, N. Sharma, W. A. De Heer, C. Berger, P. N. First, L. Magaud, E. H. Conrad, J. E. Millan-Otoya, M. Sprinkle, N. Sharma, W. A. De Heer, C. Berger, P. N. First, L. Magaud, and E. H. Conrad, "Why multilayer graphene on 4H-SiC(0001) behaves like a single sheet of graphene," *Phys. Rev. Lett.*, vol. 100, no. 12, p. 125504, 2008.

[67] F. Ramos-Mendieta, "Mid-infrared Otto excitation of transverse electric modes in doped graphene," *J. Appl. Phys.*, vol. 117, no. 13, p. 133101, 2015.

[68] J. Hass, F. Varchon, J. E. Millán-Otoya, M. Sprinkle, N. Sharma, W. A. de Heer, C. Berger, P. N. First, L. Magaud, and E. H. Conrad, "Why multilayer graphene on 4H-SiC(0001) behaves like a single sheet of graphene," *Phys. Rev. Lett.*, vol. 100, no. 12, p. 125504, 2008.

[69] J. M. Dawlaty, S. Shivaraman, J. Strait, P. George, M. Chandrashekhar, F. Rana, M. G. Spencer, D. Veksler, and Y. Chen, "Measurement of the optical absorption spectra of epitaxial graphene from terahertz to visible," *Appl. Phys. Lett.*, vol. 93, no. 13, p. 131905, 2008.

[70] H. Yan, F. Xia, W. Zhu, M. Freitag, C. Dimitrakopoulos, A. a. Bol, G. Tulevski, and P. Avouris, "Infrared spectroscopy of wafer-scale graphene,"

*ACS Nano*, vol. 5, no. 12, pp. 9854–9860, 2011.

[71] A. Das, S. Pisana, B. Chakraborty, S. Piscanec, S. K. Saha, U. V Waghmare, K. S. Novoselov, H. R. Krishnamurthy, A. K. Geim, A. C. Ferrari, and A. K. Sood, "Monitoring dopants by Raman scattering in an electrochemically top-gated graphene transistor.," *Nat. Nanotechnol.*, vol. 3, no. 4, pp. 210–215, 2008.

[72] S. Seki, S. Tsuzuki, K. Hayamizu, Y. Umebayashi, N. Serizawa, K. Takei, and H. Miyashiro, "Comprehensive refractive index property for room-temperature ionic liquids," *J. Chem. Eng. Data*, vol. 57, no. 8, pp. 2211–2216, 2012.

[73] C.-F. Chen, C.-H. Park, B. W. Boudouris, J. Horng, B. Geng, C. Girit, A. Zettl, M. F. Crommie, R. A. Segalman, S. G. Louie, and F. Wang, "Controlling inelastic light scattering quantum pathways in graphene," *Nature*, vol. 471, no. 7340, pp. 617–620, 2011.

[74] X. Li, W. Cai, J. An, S. Kim, J. Nah, D. Yang, R. Piner, A. Velamakanni, I. Jung, E. Tutuc, S. K. Banerjee, L. Colombo, and R. S. Ruoff, "Large-area synthesis of high-quality and uniform graphene films on copper foils.," *Science*, vol. 324, no. 5932, pp. 1312–1314, 2009.

[75] C. Lu, Q. Fu, S. Huang, and J. Liu, "Polymer electrolyte-gated carbon nanotube field-effect transistor," *Nano Lett.*, vol. 4, no. 4, pp. 623–627, 2004.

[76] D. A. Saville, W. R. Schowalter, N. York, P. Chester, and M. Sydney, *Colloidal Dispersions*. Cambridge University Press, 1989.

[77] A. B. McEwen, H. L. Ngo, K. LeCompte, and J. L. Goldman, "Electrochemical properties of imidazolium salt electrolytes for electrochemical capacitor applications," *J. Electrochem. Soc.*, vol. 146, no. 5, pp. 1687–1695, 1999.

[78] H. Ohno, *Colloidal Dispersions Electrochemical Aspects of Ionic Liquids*. New Jersey: John Wiley & Sons, Inc., 2011.

# Abstract in Korean

2000년대 중반 그래핀이 발견되면서 빛-물질 상호작용의 범위가 대폭 확대되었다. 무질량 디랙 페르미온으로 작용하는 그래핀의 특이한 무간격 선형 전자 띠 구조로 인해 단일층 탄소원자의 중대한 초광대역 전기역학 반응이 일어난다. 그래핀에서의 독특한 캐리어 분산은 또한 광범위한 에너지에서 페르미 준위 조정을 가능하게 하여 특정한 주파수에서 전기 역학 반응을 통제하고 그래핀의 플라즈몬 특성을 조절한다. 가령, 광자에너지가 페르미 준위의 2배에 도달할 때 띠간 전자전이의 시작은 금속(드루드 타입)에서 유전체 유형의 반응으로의 전환을 통제하며 이때 그래핀 전도성의 허수부분은 양수에서 음수로 표시된다. 그래핀의 전기역학 반응의 이러한 분광 전이는 본 연구의 핵심인 두 가지 독특한 플라즈몬 현상과 관련 있다.

첫째, 그래핀은 1D 금속-유전체 인터페이스를 가진 2D 금속-유전체 시스템이 구현될 수 있는 현실적 플랫폼을 제공한다는 사실이 집중 조명되었다. 비균일 도핑임을 가정하여 그래핀의 측면으로 연결된 서로 다른 특성을 보이는 두 개의 반무한 영역을 검토하였다. 하나는 금속인 반면 다른 하나는 동등한 도핑 레벨의 저손실 유전체로 그래핀의 전도성의 허수부분에서 음수를 나타낸다. 이러한 배열에서 1D 금속-유전체 인터페이스(그래핀 플랫폼에서 구현)가 차단 행동을 보이는 기본 1D 플라즈몬 모드를 지원하여 2D 시스템에서 빛의 포획을 상당히 증가시킨다는 점이 이론상으로나 수적으로 최초로 증명되었다. 이러한 1D 플라즈몬 모드는 플라즈몬 패밀리에 존재하지 않던 1D 멤버로 플라즈몬의 새로운 기본 카테고리를 다음과 같이 구성한다: 3D 벌크

플라즈몬, 2D 표면 플라즈몬, 1D 플라즈몬 및 0D 국부 플라즈몬.

둘째, 그래핀의 전기 역학 반응의 또 다른 독특한 특성인, 전도성의 허수 부분이 음수일 때 극명하게 드러날 것으로 예상되는 횡단 전기(TE) 전파 모드에 대한 연구가 활발히 이루어지고 있다. 아직은 요원하지만 유한 온도에서 TE모드를 실험으로 직접 탐지하기 위한 실행 가능한 플랫폼이 구현되어야 한다. 본 연구에서 오토-크레슈만 접근법이 그래핀에서 TE 모드 여기(excitation)를 위한 실행 가능한 플랫폼으로 보여진다. 오토 배열의 그래핀으로 지원되는 TE모드는 전형적인 유한 온도의 단일층 그래핀과 입사파의 효율적 커플링을 방지하는 커플링 프리즘과 그래핀층 사이의 차단 두께를 보여준다는 사실이 이론적으로 입증되었다. 이에 반해, N-층 그래핀 더미는 효율적 그래핀 전도성이 N배 증가하여 커플링이 상당히 증가할 것으로 예상된다.

그래핀은 여기(excitation) 환경 및 위상 정합 조건 부착에 극도로 민감하기 때문에 그래핀에서 TE모드의 여기(excitation) 및 그 이상의 탐지는 해결해야 할 도전과제였다. 본 연구는 최초로 TE 모드의 직접적 광학 탐지를 구현했으며 극도로 정확한 위상 정합을 가진 수정된 오토 배열을 활용하였다. 본 연구에서 예측한대로 상온에서 전기적으로 도핑된 다층 그래핀 시트에서 입사파와의 상당한 커플링이 입증되었다. 본 연구에서 제안한 세밀한 위상 정합 기술 및 그래핀의 TE 여기(excitation)에 대한 접근은 이러한 독특한 현상에 대한 심층 연구를 촉진하고 다양한 포토닉스 분야에서의 적용을 가능하게 할 것이다.

**주요어:** 그래핀, 그래핀 플라즈모닉, 횡단 전기 모드, 1D 플라즈몬, 2D 결정체.

**학번:** 2012-31289